

U.S. DEPARTMENT OF COMMERCE
National Technical Information Service

AD-A027 705

A DETERMINISTIC METHODOLOGY FOR DISCRIMINATING
BETWEEN EARTHQUAKES AND UNDERGROUND NUCLEAR
EXPLOSIONS

SYSTEMS, SCIENCES AND SOFTWARE

PREPARED FOR
AIR FORCE OFFICE OF SCIENTIFIC RESEARCH

JULY 1976

218108

AFOSR - TR - 76 - 0924

ADA 027705



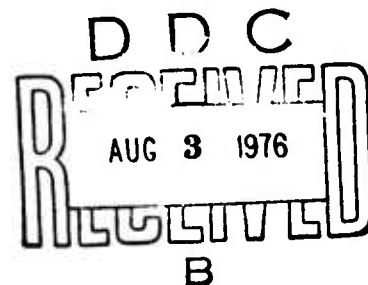
SYSTEMS, SCIENCE AND SOFTWARE

SSS-R-76-2925

**A DETERMINISTIC METHODOLOGY FOR DISCRIMINATING BETWEEN
EARTHQUAKES AND UNDERGROUND NUCLEAR EXPLOSIONS**

T. C. Bache
J. T. Cherry
D. G. Lambert
J. F. Masso
J. M. Savino

FINAL TECHNICAL REPORT



Sponsored by:

Advanced Research Projects Agency
ARPA Order No. 1827
Program Code 4F10

Contract No. F44620-74-C-0063
Effective Date of Contract: 4/1/74
Contract Expiration Date: 6/30/76
Amount of Contract: \$600,430

REPRODUCED BY
NATIONAL TECHNICAL
INFORMATION SERVICE
U. S. DEPARTMENT OF COMMERCE
SPRINGFIELD, VA. 22161

July 1976

OFFICE OF SCIENTIFIC RESEARCH (AFSC)
TRANSMITTAL TO DDC
Technical report has been reviewed and is
for public release in accordance with AFR 100-12 (7)
which is unlimited.

Information Officer

DISCLAIMER NOTICE

THIS DOCUMENT IS THE BEST
QUALITY AVAILABLE.

COPY FURNISHED CONTAINED
A SIGNIFICANT NUMBER OF
PAGES WHICH DO NOT
REPRODUCE LEGIBLY.

Much of this report is devoted to a study of the earthquake source. A three-dimensional finite difference model for earthquake faulting was developed and an earthquake simulation was carried out. Results from this complex, nonlinear earthquake simulation were compared to equivalent events computed with elastodynamic models of the relaxation and dislocation type. The interesting conclusion is that as a radiator of elastic waves, the finite difference source is similar to the relaxation/volume source model proposed by Archambeau.

The comparison between the finite difference computed source and other source models was facilitated by the representation of the numerical source in terms of an equivalent elastic source. In this way high resolution methods for simulating complex seismic sources can be linked with high resolution elastic wave propagation techniques. This capability was used to compute teleseismic body wave seismograms for a complex earthquake source computed using the Archambeau/Minster model. We found that fault propagation at finite rupture velocity has a significant effect on the teleseismic short period ground motion recordings. A scaling law relating teleseismic body wave amplitudes to the source parameters and elastic properties of the material in the fault region was also developed.

A computer code (MARS) was developed for signal detection, enhancement and analysis. This code can treat multi-component seismic data and has proven extremely useful for the problem of focal depth determination for shallow seismic events.

The Variable Frequency Magnitude (VFM) technique, which is embodied in the MARS code, was tested on large populations of Eurasian and North American events for its usefulness as a discriminant between earthquakes and explosions. Complete separation of earthquake and explosion populations, based on short-period recordings only, was achieved for events with body wave magnitudes (m_b) as low as 4.0 to 4.5.

SYSTEMS, SCIENCE AND SOFTWARE

SSS-R-76-2925

A DETERMINISTIC METHODOLOGY FOR DISCRIMINATING BETWEEN EARTHQUAKES AND UNDERGROUND NUCLEAR EXPLOSIONS

T. C. Bache
J. T. Cherry
D. G. Lambert
J. F. Masso
J. M. Savino

FINAL TECHNICAL REPORT

ACCESSION for	
NTIS	Write Sample <input checked="" type="checkbox"/>
DOC	Best of Best <input type="checkbox"/>
UNANNOUNCED	<input type="checkbox"/>
JUSTIFICATION	
BY	
DISTRIBUTION AVAILABILITY CODES	
Dist.	CRITICAL
A	

Sponsored by:

Advanced Research Projects Agency
ARPA Order No. 1827
Program Code 4F10

Contract No. F44620-74-C-0063
Effective Date of Contract: 4/1/74
Contract Expiration Date: 6/30/76
Amount of Contract: \$600,430

July 1976

P. O. BOX 1620, LA JOLLA, CALIFORNIA 92038, TELEPHONE (714) 453-0060

FOREWORD

This final technical report entitled, "A Deterministic Methodology for Discriminating Between Earthquakes and Underground Nuclear Explosions," is submitted by Systems, Science and Software (S³) to the Advanced Research Projects Agency and to the Air Force Office of Scientific Research (AFOSR). This report presents the results of a research effort directed toward the development of an optimum multi-discriminant/detection procedure for earthquakes and explosions. The work was performed under Contract Number F44620-74-C-0063. Mr. William J. Best was the AFOSR technical contracting officer.

Dr. J. Theodore Cherry was the S³ project manager. Drs. Thomas C. Bache and Joseph F. Masso and Mr. Bruce Mason were responsible for the development and application of the seismic ground motion prediction technique. Dr. John M. Savino and Messrs. Kenneth G. Hamilton and David G. Lambert were responsible for the analysis of the seismic data against which all theoretical developments must eventually be tested. Acting as consultants on the project were Professors Charles B. Archambeau of the University of Colorado, David G. Harkrider of the California Institute of Technology and Donald V. Helmberger of the California Institute of Technology.

The authors wish to extend their sincere appreciation to Ms. Bernadine Ludwig and Ms. Darlene Roddy for the many hours spent in the preparation of this report.

TABLE OF CONTENTS

	Page
FOREWORD	1
LIST OF ILLUSTRATIONS	5
LIST OF TABLES	12
I. INTRODUCTION	13
II. THE TRES CODE	18
2.1 INTRODUCTION	18
2.2 CONSERVATION OF LINEAR MOMENTUM	19
2.3 BOUNDARY CONDITIONS	22
2.4 THE CALCULATION OF VELOCITY, DISPLACEMENT AND THE TIME INCREMENT	24
2.5 STRAIN RATE	25
2.6 NONLINEAR MATERIAL BEHAVIOR	28
2.7 THE LINEAR MODULE	30
III. FINITE DIFFERENCE EARTHQUAKE MODEL	32
3.1 INTRODUCTION	32
3.2 MODELING PROCEDURE	33
3.3 EQUIVALENT ELASTIC SOURCE REPRESENTATION	43
3.4 THE SEISMIC WAVE RADIATION CHARACTER OF THE SOURCE	47
3.5 COMPARISON TO THE ARCHAMBEAU/MINSTER RELAXATION SOURCE MODEL	57
3.6 COMPARISON WITH DISLOCATION MODELS	64
3.7 CONCLUSIONS	72
IV. SHORT PERIOD THEORETICAL SEISMOGRAMS FOR A PROPAGATING SOURCE MODEL FOR EARTHQUAKES.	76
4.1 INTRODUCTION	76

	Page
4.2 COMPUTATION OF THEORETICAL SEISMO-GRAMS	77
4.3 THE ARCHAMBEAU/MINSTER EARTHQUAKE SOURCE MODEL	82
4.4 THEORETICAL SEISMOGRAMS	90
4.5 ANALYSIS OF THEORETICAL SEISMOGRAMS	96
4.6 CONCLUDING REMARKS	104
V. THE MULTIPLE ARRIVAL RECOGNITION SYSTEM	106
5.1 INTRODUCTION	106
5.2 DESCRIPTION OF MARS	106
5.3 MARS ANALYSIS OF THE NTS EXPLOSION CHARTREUSE	111
5.4 DISCUSSION OF DEPTH ESTIMATION	120
5.4.1 Location Programs	120
5.4.2 Spectra for Narrow-Band Filtering	121
5.5 SUMMARY AND RECOMMENDATIONS	125
VI. VARIABLE FREQUENCY MAGNITUDE DISCRIMINANT.	126
6.1 INTRODUCTION	126
6.2 PHYSICAL BASIS FOR THE VFM DISCRIMINANT	127
6.3 NARROW-BAND FILTERING	131
6.4 APPLICATION OF THE VFM TECHNIQUE TO OBSERVED EVENTS	135
6.4.1 Shallow Events Recorded at LASA and Norway	135
6.4.2 VFM for Deep Events ($h \geq 70$ km)	140
6.4.3 North American Events Recorded in Canada	144
6.5 MULTIPLE EXPLOSION SCENARIO	145

	Page
6.6 APPLICATION OF VFM TO THEORETICAL SEISMOGRAMS	150
6.6.1 Calculation of Synthetic Seismograms	150
6.6.2 VFM Values for Synthetic Explosion Seismograms	155
6.6.3 VFM Values for Synthetic Earthquake Seismograms	158
6.7 COMPARISON OF SYNTHETIC TO OBSERVED VFM DATA.	164
6.7.1 Comparison of Explosion VFM Data	164
6.7.2 Comparison of Earthquake VFM Data	166
6.7.3 Comparison of Explosion- Earthquake VFM Data	166
6.8 SUMMARY AND CONCLUSIONS	169
VII. REFERENCES	172

LIST OF ILLUSTRATIONS

No.		Page
2.1	The centroids of the eight elements surrounding an interior nodal point are A, B,C,D,E,F,G,H.	21
2.2	Exterior points of zone A are labeled 1, 2,3,4,5,6,7,8.	26
3.1	Geometry for the finite difference earthquake simulation. The fault plane on which the rupture radiates symmetrically is shown on the left. The first octant of the grid is depicted on the right including the dimensions of the "nonlinear zone" and the "elastic radius". . . .	35
3.2	The time history of tangential stress at five locations on the fault surface (see insert). The σ_{xy} is sampled at the nine indicated time points. The connecting lines are then approximate. Closed circles indicate that the fault is tied.	39
3.3	The X displacement (half the fault offset) corresponding to the tangential stress in Figure 3.2.	40
3.4	The out-of-plane (Y) displacement of the fault surface. On the left are shown the displacements on half the fault at the last time step. The displacements are symmetric about the X axis and antisymmetric about Z. On the right the time history is depicted via nine snapshots of the displacements on the fault centerline, the X axis	42
3.5	The radial velocity and displacement time histories at two stations on the elastic radius. The position of the stations is indicated on the figures: The left plot is for the station in the center of the first octant; the right plot is for a station in the XZ plane, 45° from each axis. The indicated times, $P_{arr} = 1.5/\alpha$ and $S_{arr} = 1.5/\beta$, are the earliest times at which undispersed elastic waves can arrive from the point of rupture initiation. . .	44

No.		Page
3.6	The amplitude of the monopole and largest quadrupole and octupole terms for the equivalent elastic source representation of our earthquake referred to the coordinate system of Figure 3.1.	48
3.7	Orientation of the fault with respect to the geographic coordinate system	50
3.8	Far-field displacement spectra at two locations (specified by ϕ and τ) on the elastic radius ($R = 1.5$ km).	51
3.9	Far-field radiation patterns at three frequencies for the finite difference earthquake source. The patterns are for $\theta = 90^\circ$; that is, we plot the amplitude of the SH and P waves radiated in the X_G - Y_G plane. The coordinate system and first motion direction for the SH waves are indicated in the top middle plot. The two rows are for two levels of truncation (N) of the multipolar expansion. The amplitude of the outer ring for each frequency is indicated on the bottom row with $a = 9/R$ cm/km.	56
3.10	Far-field displacement spectra at $R = 1.5$ km, $\phi = 15^\circ$, $\tau = 30^\circ$, for the finite difference model compared to the Archambeau/Minster model with two source geometries. The diameter of the growing spherical volume is indicated at five equally spaced time steps from 0 to 1.0/2.7 sec. Modification of the unilateral rupture (right) to represent a bilateral rupture is described in the text.	60
3.11	Far-field radiation patterns for the bilateral fault (TES) constructed from the tangentially expanding sphere model. These patterns are for $\theta = 90^\circ$ and are directly comparable to those in Figure 3.9 for the finite difference source. Again, $a = 9/R$ cm/km.	63

No.		Page
3.12	Comparison of the far-field SH spectrum at $\tau = 30^\circ$, $\phi = 30^\circ$, for the finite difference earthquake source to spectra from a dislocation model with two rupture time histories (3.18, 3.19). The spectra are normalized by the moment and the double-couple radiation pattern effect. For the dislocation time histories T has been selected to bring the corner frequencies into agreement, using the half amplitude rule.	69
3.13	The static dislocation on the fault surface (left) and one zone (0.1 km) from the fault surface. The average dislocation (d_a) over the plane is indicated by a dotted line on each plot. The data points are the values at the nodes in the grid. The nodes are indicated by their distance from the $X = 0$ or $Z = 0$ line	71
4.1	The geometry and coordinate system for a source at depth h in a multilayered half-space.	79
4.2	The geometry and coordinate system for a right-lateral strike-slip fault. The outgoing displacement field along the ray A is specified by the azimuth ϕ and takeoff angle τ	85
4.3	Far-field displacement radiation patterns at three frequencies (plotted vertically) and three levels of truncation of the multipolar coefficients. The patterns are for fixed azimuth $\phi = 45^\circ$ and are oriented with respect to the system of Figure 4.2 as indicated in the double-couple patterns of the first row. The SH component is suppressed on the $N = 4$ and first set of $N = 6$ plots. (The meaning of the plot symbols is indicated on the last two plots in the center row.) The displacement amplitude at the outer circle is indicated in units of a , $a = 1.98$ cm-sec	87
4.4	Free-field displacement spectra at $R = 100$ km, $\tau = 30^\circ$ for two azimuths	88

No.		Page
4.5	Theoretical seismograms at an epicentral distance of ≈ 4050 km and two azimuths with respect to the strike-slip earthquake sources of Table 4.3. All records have been scaled to stress drop $\sigma(0) = 100$ bars. The focal depth, fault length and m_b are indicated on each record. At left is the maximum peak-to-peak amplitude in millimicrons at 1 Hz. The bar indicates the phase at which the m_b measurement is made and T is the apparent period of this phase.	94
4.6	Theoretical seismograms at 15 azimuths ($0 < \phi < 180$) for the $L = 8.4$ km source at a 25 km focal depth. The m_b phase from which it was computed, apparent period of this phase and maximum peak-to-peak amplitude (1 Hz) are shown as in Figure 4.5	95
4.7	Theoretical seismograms at several levels of truncation (N) of the multipolar expansion. Otherwise the calculation is identical to that of Figure 4.5a. The fourth record differs from the third in that a constant spreading factor (GS) was used to represent the upper mantle.	97
4.8	The maximum peak-to-peak amplitude versus azimuth for the strike-slip source at 25 km focal depth. The amplitudes are from the records of Figure 4.6 and are normalized to that for $\phi = 45^\circ$. The closed circles represent an upward (compressional) first motion and the open circles are for downward first motion. The broken line indicates the normalized amplitudes expected for a simple double-couple source. The circles are for amplitude ratios of 0.5 and 1.0	99
4.9	Seismograms like those of Figure 4.5a except that the first three layers of the source region crustal structure have been made identical to the fourth. The source at all depths is that specified by (4.6)	100
5.1	MARS flowchart.	108
5.2	Flowchart indicating principal mathematical operations embodied in the MARS code.	109

No.		Page
5.3	Polarization filtering of Chartreuse-KNUT record ($\Delta = 312$ km) where indicated arrivals (arrows) are predicted times.	114
5.4	Polarization filtering of Chartreuse-MNNV record ($\Delta = 201$ km) where indicated arrivals (arrows) are predicted times.	117
5.5	P and S arrival times at KNUT and MNNV from Chartreuse.	122
5.6	P_n , P^* , and P_g^2 amplitude spectra for Chartreuse-KNUT.	124
6.1	Event spectra at base of crust in the source region	129
6.2	Narrow-band filter used in MARS.	132
6.3	Examples of increasing signal-to-noise ratio for a presumed explosion (top left frame) recorded at Norway with successive application of high frequency narrow-band filters. Arrow at top denotes approximate arrival times of the P-wave on the unfiltered trace.	134
6.4	Spectral magnitudes, \bar{m}_b , computed at 0.45 Hz and 2.25 Hz. The presumed explosions numbered 35 and 138 occurred at Novaya Zemlya	136
6.5	Spectral magnitude estimates at $f_c = 0.6$ Hz and $f_c = 5.0$ Hz for an event population recorded at the Oyer array in Norway. The arrows attached to several of the closed circles indicate that the low frequency (0.60 Hz) m_b estimates are at the prevailing noise level as determined from recording segments immediately preceding each signal onset.	138
6.6	Maximum filter amplitudes with noise correction for the same event population plotted in Figure 6.5.	139
6.7	Spectral magnitude estimates of deep earthquakes recorded at LASA. The shallow earthquake and explosion populations plotted in Figure 6.4 are contoured in this figure.	141

No.		Page
6.8	Maximum filter amplitudes corrected for noise for deep earthquakes recorded at Norway and compared with the shallow event populations. . . .	142
6.9	Narrow-band filter outputs at three different center frequencies ($f_c = 0.3, 1.0$ and 6.0 Hz) for an explosion (left-hand side) and a deep earthquake (right-hand side)	143
6.10	Variable frequency magnitude estimates, $m_b(f)$, computed at 0.425 Hz and 2.5 Hz for a population of Gulf of California earthquakes (O's) and NTS explosions (X's)	146
6.11	Primary explosion signature (bottom-center) used to make composite seismograms at five different azimuths from the array of eight explosions. The firing order and spacing of the explosions are indicated in the center	147
6.12	Spectral magnitudes for same event population and filter parameters as in Figure 6.4 with estimates for multiple explosions (X's) showing complete discrimination.	149
6.13	Theoretical seismograms for NTS events at two epicentral distances. The event yield (KT) and DOB (km) is indicated on the left. Given with each seismogram is the approximate peak-to-peak amplitude in microns at 1 Hz. The instrument response is specified by the LRSM nominal response curves.	154
6.14	Theoretical seismograms for a right-lateral strike-slip event at an epicentral distance of ≈ 2500 km and an azimuth 30° counterclockwise from the strike. The fault length is indicated and the stress drop is 100 bars. At the left is the maximum peak-to-peak amplitude in microns at 1.0 Hz.	156
6.15	Theoretical seismograms identical to those of Figure 6.14 except that the upper mantle response is now appropriate to a distance of 4000 km.	157
6.16	Theoretical NTS explosion VFM estimates for two distance ($21^\circ, 36^\circ$).	159

No.		Page
6.17	Plot of VFM for five events at three different fault orientations. The distance and azimuth are 4000 km and 30° for all seismograms.	161
6.18	Theoretical VFM estimates for three strike-slip earthquakes	162
6.19	Theoretical VFM estimates for the seismograms of Figures 6.14 and 6.15	163
6.20	Comparison of theoretical to observed explosion (NTS-YKA) VFM estimates.	165
6.21	Comparison of theoretical strike-slip earthquakes to observed earthquake (Gulf of California-YKA) VFM estimates	167
6.22	Comparison of theoretical and observed explosion and earthquake VFM estimates.	168

LIST OF TABLES

No.		Page
3.1	Corner frequencies at various positions on the radiation pattern.	53
3.2	Comparison of multipole coefficients for the finite difference earthquake (FD) to those from the analytical bilateral fault constructed from the Archambeau/Minster tangentially expanded sphere (TES).	62
4.1	Basin and range crustal structure.	91
4.2	Average continental crust.	91
4.3	Source parameters for events at five focal depths	93
4.4	Scaling of b amplitudes for the records of Figure 4.6	103
5.1	Predicted versus observed travel-times	119
6.1	Characteristics of explosion events for synthetic seismograms	151
6.2	Yucca Flat crust for theoretical seismograms . .	152
6.3	Pahute Mesa crust for theoretical seismograms. .	152

I. INTRODUCTION

The fundamental problem toward which our research efforts were directed under this project is seismic discrimination. Briefly stated, the objective of this program was the development of an optimum multi-discriminant/detection procedure for earthquakes and underground nuclear explosions.

Our approach to the solution of the seismic discrimination problem was the development of a deterministic methodology for predicting teleseismic ground motion from both earthquakes and explosions. This predictive capability provides a theoretical basis against which existing discriminants may be tested and new discriminants designed.

The principal areas of research pursued during the course of this project are the following:

1. Explosion and earthquake source modeling, including finite difference and analytic formulations.
2. Stress wave propagation through complicated, realistic earth structures.
3. Development of state of the art signal enhancement and identification techniques.
4. Multi-discriminant design and evaluation.

Each of the sections of this report is devoted to a self-contained description of current results relating to one of the four research areas listed above. Previous semi-annual technical reports written under this contract (Bache, et al., 1974, 1975; Savino, et al., 1975) have also contained sections that are viewed as self-contained reports on these and related subjects. We would like to point out that this report is not a summary of all work carried out

under this contract, but is primarily devoted to work done since the last semi-annual report.

Much of the work done under this contract is of interest to the scientific community at large and we plan to disseminate the important results by publication in the appropriate scientific journals. Two papers have been accepted for publication in the October (Bache, 1976) and December (Bache and Harkrider, 1976) issues of the Bulletin of the Seismological Society of America. The material of Chapters III, IV and VI of this report may be viewed as drafts of papers to be submitted for publication.

The first two sections of the report deal with the three-dimensional finite difference simulation of earthquake faulting. In Section II, a recently developed computer code, TRES, is described. The TRES code represents a finite difference simulation of stress wave propagation in three space dimensions. Special features of this code include the capability to model nonhomogeneous geologic environments and provisions for linking regions where material behavior is linear elastic with regions where the behavior is nonlinear.

Section III is devoted to a description of the application of TRES to simulate strike-slip earthquake faulting. With this three-dimensional finite difference code a numerical simulation of bilateral faulting on a 1.0×0.6 km fault plane was carried out. The basic mechanism for releasing the stored strain energy was relaxation of the tangential stress at the slipping interface from its welded value to its kinetic friction value.

An important step in our analysis of the results of the finite difference earthquake simulation is a representation of the earthquake generated elastic wave field in terms of an equivalent elastic point source. This equivalent

elastic source representation is important because it allows a linkage between the numerical codes and the analytical wave propagation techniques of theoretical seismology.

Our primary interest in earthquakes is in their character as radiators of elastic waves to the far field. An advantage of the equivalent elastic source representation is that it allows a convenient comparison between our finite difference source and the far-field radiation characteristics of elastodynamic earthquake source theories. A number of intriguing results are found from a comparison of far-field displacement spectra from the finite difference source to those from equivalent earthquakes modeled by the relaxation/volume source model of Archambeau/Minster (Archambeau, 1968; Minster, 1973) and simple dislocation models (Haskell, 1964; Savage, 1972). We find that in almost all respects (moment, radiation pattern, corner frequency behavior) the radiation from our finite difference source more closely resembles that from the Archambeau/Minster model. This is in spite of the fact that in terms of a kinematic description of the fault displacements, the finite difference earthquake is quite similar to a dislocation model. In fact, when we construct an equivalent dislocation model from the outgoing radiation field generated by the finite difference earthquake, we find rather poor agreement between the actual fault parameters (rise time and slip) and those of the equivalent dislocation model. We attribute this disagreement to the fact that in the finite difference calculation the stress concentrations that occur around the fault edges are relieved by plastic flow. While we do not want to place too much significance on a single finite difference calculation, this example does point out a potential difficulty with attaching physical significance to equivalent dislocation model parameters.

In Section IV is presented the results of a study in which we apply our newly developed techniques for linking

complex source models (such as the finite difference source of Section III) with methods for elastic wave propagation in realistic earth structures. The objective of the study is to compute synthetic seismograms for a sufficiently complex source model to illustrate the potential utility of the techniques for general seismological research. In doing this we develop a scaling law relating teleseismic body wave amplitudes to the source parameters and the elastic properties of the material in the fault region.

Section V is devoted to a description of the mode of operation of the Multiple Arrival Recognition System (MARS) computer code and its application to explosion seismograms. The MARS code is proving to be particularly effective for detecting, isolating and timing the various seismic phases (P_g , P^* , P_n , S_g , S^* , S_n , etc.) that are recorded on event seismograms in the near-regional and regional distance ranges. The signal analysis capabilities for narrow-band and polarization filtering are finding immediate application to the problem of depth determinations for shallow focus events. More accurate event depths can be obtained by incorporating P and S wave arrival times in standard hypocentral location routines and by the combined usage of spectra of isolated body waves for identification of spectral nulls caused by the interference of direct and free-surface reflected phases.

The variable frequency magnitude (VFM) technique, embodied in the MARS code, has been tested on both observed and synthetic short-period P wave seismograms from seismic events to determine its effectiveness as a discriminant between earthquakes and explosions. In Section VI we present the results of an application of the VFM technique to a large population of Eurasian events recorded at LASA and NORSAR and to North American events recorded at the Yellowknife array in Canada. Obviating the requirement for

recording surface waves from small explosions results in an extended magnitude range over which this discriminant can be applied. Based on the event populations examined so far, in particular those occurring in Eurasia, complete separation of earthquakes and explosions is achieved with the VFM technique down to event magnitudes, m_b , in the range 4.0 to 4.5.

Section VI concludes with a comparison of VFM estimates for theoretical and observed explosion and earthquake seismograms for the case where the travel path effects are comparable. The VFM estimates for the observed and synthetic event populations compare well in terms of both absolute values and population trends.

II. THE TRES CODE

2.1 INTRODUCTION

The TRES code represents a finite difference simulation of stress wave propagation in three space dimensions. In the code the conservation of linear momentum, containing the spatial derivatives of the individual stress components, is written in finite difference form. Nonlinear material behavior is simulated by differencing the components of strain rate and incrementing stress according to an appropriate constitutive model. Explicit time stepping is used to advance the solution in time. The output of the code is usually time histories of displacement, velocity, stress and/or their derivatives at selected distances from the source.

The limitations of the code are as follows:

1. The code is written in three dimensional Cartesian geometry and the basic element is a rectangular parallelepiped.
2. All Lagrangian rates of change are replaced by local rates of change. This small deformation assumption linearizes the differential equation governing the conservation of momentum and removes the distinction between Eulerian and Lagrangian coordinates.
3. Stability of the transient solution requires that the time step (Δt) be less than the time required to propagate a compressional wave through an element in the grid.

The code contains the following special features:

1. Contact discontinuity boundary conditions are used to obtain the normal and tangential components of stress over a specified interior

surface of the computational grid. If the tangential stress is then relaxed at a point on the surface, a discontinuity in tangential velocity results. This technique has been used to simulate the earthquake presented in Chapter III.

2. Both exterior and contact discontinuity boundary conditions follow naturally from the interior difference equations used for conservation of momentum. This feature of the difference equations also permits nonuniform zoning to be used in the grid.
3. A constitutive equation is able to be specified for each element in the grid. Therefore a non-homogeneous geologic environment is easily modeled. Furthermore, the code contains a provision for linking regions where material behavior is linear elastic with regions where the behavior is nonlinear. The divergence and curl of the displacement field may be monitored over a spherical surface in the elastic region. The equivalent elastic source discussed in Chapter III is obtained from these derivatives of the displacement field.

2.2 CONSERVATION OF LINEAR MOMENTUM

If u , v , and w are the x , y , and z components of velocity, then the conservation of linear momentum may be written:

$$\frac{du}{dt} = \frac{\partial (P + \sigma_x)}{\rho \partial x} + \frac{\partial \sigma_{xy}}{\rho \partial y} + \frac{\partial \sigma_{xz}}{\rho \partial z} , \quad (2.1)$$

$$\frac{dv}{dt} = \frac{\partial \sigma_{xy}}{\rho \partial x} + \frac{\partial (P + \sigma_y)}{\rho \partial y} + \frac{\partial \sigma_{yz}}{\rho \partial z} , \quad (2.2)$$

$$\frac{dw}{dt} = \frac{\partial \sigma_{xz}}{\rho \partial x} + \frac{\partial \sigma_{yz}}{\rho \partial y} + \frac{\partial (P - \sigma_x - \sigma_y)}{\rho \partial z} , \quad (2.3)$$

There will be eight elements surrounding an interior nodal point. The centroids of these elements are labeled A through H as shown in Figure 2.1. The following increments in x, y, and z give the distances from the interior nodal point, at which the acceleration is to be computed, to the corresponding centroid.

$$\begin{aligned} \Delta x^+ &\rightarrow A, D, E, H & \Delta y^+ &\rightarrow A, B, E, F & \Delta z^+ &\rightarrow A, B, C, D \\ \Delta x^- &\rightarrow B, C, F, G & \Delta y^- &\rightarrow C, D, G, H & \Delta z^- &\rightarrow E, F, G, H \end{aligned}$$

If Σ is a typical stress component in the above equations, then the differenced form of the spatial derivatives used in the code are as follows:

$$\begin{aligned} \frac{\partial \Sigma}{\rho \partial x} &= \frac{\Sigma_{AB} (1 - \xi^Y) (1 - \xi^Z)}{\rho_A \Delta x^+ + \rho_B \Delta x^-} + \frac{\Sigma_{DC} \xi^Y (1 - \xi^Z)}{\rho_D \Delta x^+ + \rho_C \Delta x^-} \\ &+ \frac{\Sigma_{EF} (1 - \xi^Y) \xi^Z}{\rho_E \Delta x^+ + \rho_F \Delta x^-} + \frac{\Sigma_{HG} \xi^Y \xi^Z}{\rho_H \Delta x^+ + \rho_G \Delta x^-} , \end{aligned} \quad (2.4)$$

$$\begin{aligned} \frac{\partial \Sigma}{\rho \partial y} &= \frac{\Sigma_{AD} (1 - \xi^X) (1 - \xi^Z)}{\rho_A \Delta y^+ + \rho_D \Delta y^-} + \frac{\Sigma_{BC} \xi^X (1 - \xi^Z)}{\rho_B \Delta y^+ + \rho_C \Delta y^-} \\ &+ \frac{\Sigma_{EH} (1 - \xi^X) \xi^Z}{\rho_E \Delta y^+ + \rho_H \Delta y^-} + \frac{\Sigma_{FG} \xi^X \xi^Z}{\rho_F \Delta y^+ + \rho_G \Delta y^-} , \end{aligned} \quad (2.5)$$

$$\begin{aligned}
\frac{\partial \Sigma}{\rho \partial z} = & \frac{\Sigma_{AE} (1 - \xi^x) (1 - \xi^y)}{\rho_A \Delta z^+ + \rho_E \Delta z^-} + \frac{\Sigma_{DH} \xi^y (1 - \xi^x)}{\rho_D \Delta z^+ + \rho_H \Delta z^-} \\
& + \frac{\Sigma_{BF} \xi^x (1 - \xi^y)}{\rho_B \Delta z^+ + \rho_F \Delta z^-} + \frac{\Sigma_{CG} \xi^x \xi^y}{\rho_C \Delta z^+ + \rho_G \Delta z^-} .
\end{aligned} \tag{2.6}$$

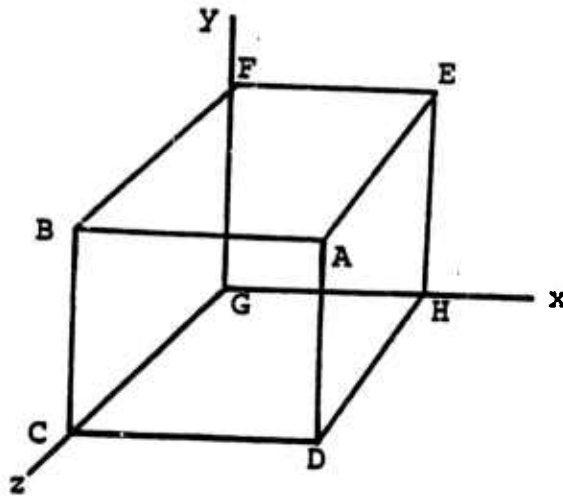


Figure 2.1. The centroids of the eight elements surrounding an interior nodal point are A,B,C,D,E,F,G,H.

The weighting factors in the above equations are:

$$\xi^x = \frac{\Delta x^+}{\Delta x^+ + \Delta x^-}, \quad \xi^y = \frac{\Delta y^+}{\Delta y^+ + \Delta y^-}, \quad \xi^z = \frac{\Delta z^+}{\Delta z^+ + \Delta z^-}, \quad (2.7)$$

where ρ_A is the density of the A element and

$$\Sigma_{AB} \equiv \Sigma_A - \Sigma_B. \quad (2.8)$$

Each stress difference is weighted based on its location relative to the interior nodal point at which the acceleration is to be computed. For example, the coordinates of Σ_{AB} relative to the interior nodal point are $(0, \Delta y^+, \Delta z^+)$. The factor $(1 - \xi^y)(1 - \xi^z)$ extrapolates the Σ_{AB} acceleration term to the interior nodal point.

2.3 BOUNDARY CONDITIONS

If a nodal point is located at a boundary then only certain elements surrounding the point will contain stress. It is these real elements along with the stress at the boundary which contribute to the acceleration of the nodal point. The weighting factors given in Eq. (2.7) provide a convenient technique for isolating the real elements.

For example, suppose that the x, y plane is a grid boundary and the real elements are in the positive z direction, i.e., A, B, C, D in Figure 2.1. If $\xi^z = 0$ in Eqs. (2.4) and (2.5), then only real elements contribute to these acceleration terms. If Σ^* is used to denote the stress at the boundary, then the first term in Eq. (2.6) may be written

$$\frac{\Sigma_{AE}(1 - \xi^x)(1 - \xi^y)}{\rho_A \Delta z^+ + \rho_E \Delta z^-} = \frac{(\Sigma_A - \Sigma_E^*)(1 - \xi^x)(1 - \xi^y)}{\rho_A \Delta z^+}. \quad (2.9)$$

Similar expressions involving Σ_F^* , Σ_G^* , Σ_H^* , ρ_B , ρ_C , ρ_O result for the remaining terms in Eq. (2.6).

If $\xi^z = 1$ in Eqs. (2.4) and (2.5), then the real elements are in the negative z direction, i.e., E, F, G, and H in Figure 2.1. The first term in Eq. (2.6) is written

$$\frac{\Sigma_{AE}(1 - \xi^x)(1 - \xi^y)}{\rho_A \Delta z^+ + \rho_E \Delta z^-} = \frac{(\Sigma_A^* - \Sigma_E)(1 - \xi^x)(1 - \xi^y)}{\rho_E \Delta z^-} \quad (2.10)$$

with similar modifications for the remaining terms.

At an exterior boundary the Σ^* stresses are specified in order to provide symmetry conditions to simulate a free surface or to initiate the stress wave. At an interior boundary the Σ^* stresses are first obtained by assuming continuity of acceleration at a nodal point on the boundary, i.e.,

$$\frac{du^+}{dt} = \frac{du^-}{dt} , \quad (2.11a)$$

$$\frac{dv^+}{dt} = \frac{dv^-}{dt} , \quad (2.11b)$$

$$\frac{dw^+}{dt} = \frac{dw^-}{dt} . \quad (2.11c)$$

If the boundary is the x, y plane, then all $+$ derivatives are evaluated with $\xi^z = 0$ and all $-$ derivatives are evaluated with $\xi^z = 1$. If we assume that

$$\Sigma_A^* = \Sigma_B^* = \Sigma_C^* = \Sigma_D^* , \quad (2.12)$$

then continuity of stress at the boundary along with Eqs. (2.11) permit a unique solution for σ_{xz}^* , σ_{yz}^* , and σ_{zz}^* at

the nodal point. If these stress components are used to move the nodal point, then the acceleration will be continuous at the boundary. Relaxation of either σ_{xz}^* or σ_{yz}^* will violate Eqs. (2.11a) or (2.11b) and shear failure (slipping) is simulated. Relaxation of σ_{zz}^* simulates tension failure.

2.4 THE CALCULATION OF VELOCITY, DISPLACEMENT AND THE TIME INCREMENT

In the code, all Lagrangian rates of change are replaced by local rates of change. This assumes that $u \frac{d}{dx} + v \frac{d}{dy} + w \frac{d}{dz}$ is small compared to $\frac{\partial}{\partial t}$. The fundamental consequence of this assumption is that a given element remains a rectangular parallelepiped during all states of deformation. At a nodal point, velocities are incremented as follows:

$$u^{n+\frac{1}{2}} = u^{n-\frac{1}{2}} + \frac{\partial u}{\partial t} \Delta t^n, \quad (2.13a)$$

$$v^{n+\frac{1}{2}} = v^{n-\frac{1}{2}} + \frac{\partial v}{\partial t} \Delta t^n, \quad (2.13b)$$

$$w^{n+\frac{1}{2}} = w^{n-\frac{1}{2}} + \frac{\partial w}{\partial t} \Delta t^n, \quad (2.13c)$$

where superscripts indicate cycle number,

Δt^n is the time increment at cycle n ,

and all acceleration components are evaluated from the finite difference approximation to Eqs. (2.1), (2.2) and (2.3).

The corresponding components of displacement, U , V , W are

$$U^{n+1} = U^n + u^{n+\frac{1}{2}} \Delta t^{n+\frac{1}{2}}, \quad (2.14a)$$

$$v^{n+1} = v^n + v^{n+\frac{1}{2}} \Delta t^{n+\frac{1}{2}}, \quad (2.14b)$$

$$w^{n+1} = w^n + w^{n+\frac{1}{2}} \Delta t^{n+\frac{1}{2}}. \quad (2.14c)$$

If ΔL^n is the minimum dimension of all the elements in the grid, then

$$\Delta t^{n+\frac{1}{2}} = a \frac{\Delta L^n}{\alpha}, \quad (2.15)$$

where

$$\alpha = \sqrt{\frac{k + \frac{4}{3} \mu}{\rho}} = \text{the compressional wave velocity,}$$

a is an input constant ≈ 0.5 .

Then

$$\Delta t^n = \frac{\Delta t^{n+\frac{1}{2}} + \Delta t^{n-\frac{1}{2}}}{2}. \quad (2.16)$$

2.5 STRAIN RATE

After the calculation of acceleration, velocity and displacement, the code proceeds to calculate the strain rate produced in the element. The centroids of the eight elements surrounding an interior nodal point are as shown in Figure 2.1. The exterior points of element A are labeled 1 through 8 as shown in Figure 2.2. The following notation has been adopted.

$$u_{12} = u_1 - u_2, \quad x_{12} = x_1 - x_2, \quad \text{etc.},$$

$$\Delta x^+ = \frac{x_{67}}{2}, \quad \Delta y^+ = \frac{y_{67}}{2}, \quad \Delta z^+ = \frac{z_{37}}{2}.$$

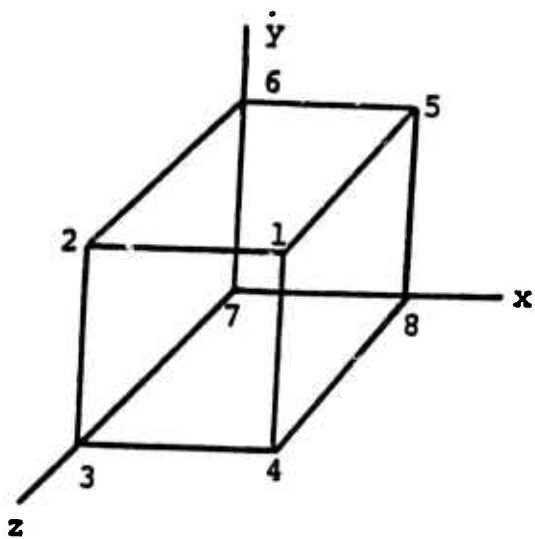


Figure 2.2. Exterior points of zone A are labeled 1,2,3,4, 5,6,7,8.

The differenced form of the strain rate components are as follows:

$$\dot{e}_{xx} = \frac{\partial u}{\partial x} = \frac{u_{12} + u_{43} + u_{56} + u_{87}}{8 \Delta x},$$

$$\dot{e}_{yy} = \frac{\partial v}{\partial y} = \frac{v_{14} + v_{23} + v_{67} + v_{58}}{8 \Delta y},$$

$$\dot{e}_{zz} = \frac{\partial w}{\partial z} = \frac{w_{15} + w_{26} + w_{37} + w_{48}}{8 \Delta z},$$

$$\frac{\dot{V}}{V} = \dot{e}_{xx} + \dot{e}_{yy} + \dot{e}_{zz}, \quad (2.17)$$

$$\dot{e}_x = \left[\dot{e}_{xx} - \frac{1}{3} \frac{\dot{V}}{V} \right], \quad (2.18)$$

$$\dot{e}_y = \left[\dot{e}_{yy} - \frac{1}{3} \frac{\dot{V}}{V} \right], \quad (2.19)$$

$$\dot{e}_{xy} = \frac{1}{2} \left[\frac{u_{14} + u_{23} + u_{67} + u_{58}}{8 \Delta y} + \frac{v_{12} + v_{43} + v_{56} + v_{87}}{8 \Delta x} \right], \quad (2.20)$$

$$\dot{e}_{xz} = \frac{1}{2} \left[\frac{u_{15} + u_{26} + u_{37} + u_{48}}{8 \Delta z} + \frac{w_{12} + w_{43} + w_{56} + w_{87}}{8 \Delta x} \right], \quad (2.21)$$

$$\dot{e}_{yz} = \frac{1}{2} \left[\frac{v_{15} + v_{26} + v_{37} + v_{48}}{8 \Delta z} + \frac{w_{14} + w_{23} + w_{67} + w_{58}}{8 \Delta y} \right]. \quad (2.22)$$

The corresponding stress increments required by Eqs. (2.1), (2.2) and (2.3) are

$$p^{n+1} = p^n + k \frac{\dot{V}}{V} \Delta t^{n+\frac{1}{2}}, \quad (2.23)$$

$$\sigma_x^{n+1} = \sigma_x^n + 2\mu \dot{e}_x \Delta t^{n+\frac{1}{2}}, \quad (2.24)$$

$$\sigma_y^{n+1} = \sigma_y^n + 2\mu \dot{e}_y \Delta t^{n+\frac{1}{2}}, \quad (2.25)$$

$$\sigma_{xy}^{n+1} = \sigma_{xy}^n + 2\mu \dot{e}_{xy} \Delta t^{n+\frac{1}{2}}, \quad (2.26)$$

$$\sigma_{xz}^{n+1} = \sigma_{xz}^n + 2\mu \dot{e}_{xz} \Delta t^{n+\frac{1}{2}}, \quad (2.27)$$

$$\sigma_{yz}^{n+1} = \sigma_{yz}^n + 2\mu \dot{e}_{yz} \Delta t^{n+\frac{1}{2}}. \quad (2.28)$$

Equation (2.17) gives the total volumetric strain rate. Equations (2.18) through (2.22) are the total deviatoric strain rates. The isotropic component of the stress tensor is given in Eq. (2.23). Note that this component is negative in compression, i.e., it is opposite in sign from the hydrodynamic pressure.

2.6 NONLINEAR MATERIAL BEHAVIOR

The basic assumption of nonlinear continuum mechanics is that the total strain rate \dot{e}_{ij} is composed of elastic $\dot{\eta}_{ij}$ and inelastic $\dot{\pi}_{ij}$ components, i.e.,

$$\dot{e}_{ij} = \dot{\eta}_{ij} + \dot{\pi}_{ij}. \quad (2.29)$$

Only the elastic components are used to increment stress. If $\dot{\pi}_{ij} \neq 0$, then all total strain rates in Eqs. (2.23) through (2.28) must be replaced by elastic strain rates. The constitutive equation determines $\dot{\pi}_{ij}$ at a given stress state.

Various models for nonlinear material behavior have been developed and used at S^3 in one and two dimensional stress wave codes. These include models of tension failure,

plastic flow, effective stress, irreversible pore collapse and dilatancy. At the present time, TRES contains only the plastic flow model, which has been used to simulate non-linear material behavior in the fault zone.

For plastic flow we assume that the maximum allowable stress difference, Y , is known. The stress deviators \hat{S}_{ij} are calculated using total strain rates as given by Eqs. (2.24) through (2.28), where

$$\begin{aligned}\hat{S}_{11} &= \sigma_x, & \hat{S}_{12} &= \sigma_{xy}, \\ \hat{S}_{22} &= \sigma_y, & \hat{S}_{13} &= \sigma_{xz}, \\ & & \hat{S}_{23} &= \sigma_{yz}.\end{aligned}$$

The second deviatoric invariant is

$$J'_2 = \frac{1}{2} \hat{S}_{ij} \hat{S}_{ji} = \sigma_x^2 + \sigma_y^2 + \sigma_x \sigma_y + \sigma_{xy}^2 + \sigma_{xz}^2 + \sigma_{yz}^2$$

Plastic flow results if

$$J'_2 > \frac{Y^2}{3}. \quad (2.30)$$

Then

$$S_{ij} = \hat{S}_{ij} \frac{Y}{\sqrt{3J'_2}}, \quad (2.31)$$

and the S_{ij} stresses are used to calculate accelerations. The increment in plastic strain corresponding to the stress adjustment given by Eq. (2.31) is

$$\Delta \pi_{ij} = \frac{\hat{S}_{ij} - S_{ij}}{2\mu}. \quad (2.32)$$

The corresponding increment in plastic work is

$$\Delta E = S_{ij} \Delta \pi_{ij} = \frac{Y^2}{3\mu} \left[\frac{\sqrt{3J^2}}{Y} - 1 \right]. \quad (2.33)$$

A plastic work rupture criterion has proven to be an effective technique for controlling the rupture velocity during earthquake simulation (Cherry, et al., 1976).

The flexibility of the code to accept various modes of nonlinear material behavior is contained in the stress rate-strain rate formulation given by Eqs. (2.23) through (2.28). Modification of these stresses at time t^{n+1} is obtained through the constitutive equation which determines the inelastic strain rate in Eq. (2.29). The code now contains the plastic flow model. Additional constitutive models are a straightforward extension of those existing in one and two dimensional codes. These will be included as the need arises.

2.7 THE LINEAR MODULE

The nonlinear region in TRES is linked to a linear module. The physical dimensions of the surface over which the nonlinear and linear modules are linked must be specified by the user.

The link has two objectives, decreasing computation time and coupling the results of the finite difference calculation to analytic wave propagation techniques.

The former is achieved since stress is related to strain through Hooke's law. Stress is not a saved variable in the linear module since it is calculated from nodal point displacements.

The latter is achieved by constructing an equivalent point source which provides an analytic continuation of the

outgoing stress field in the elastic region. The divergence and curl of the displacement field are monitored over a spherical surface in TRES and are used to obtain the multipole coefficients in a spherical wave expansion of the radiating elastic field.

In the following section we describe the application of TRES for simulating strike-slip earthquake faulting. The determination of an equivalent elastic point source representation of the earthquake from the TRES output in the linear regime is an important step in describing the character of the source as a radiator of far-field seismic waves.

III. FINITE DIFFERENCE EARTHQUAKE MODEL

3.1 INTRODUCTION

It is only within the last 10-15 years that serious attempts have been made to develop a mathematical model for the earthquake source. Source theory, as it is often called, remains a subject of considerable interest and controversy and much scientific energy is being expended to develop new source theories, expand old ones or to demonstrate the ability of a particular theory to explain some portion of earthquake data. The subject of this section of the report is an earthquake source model that employs finite difference numerical techniques. We use this model to carry out a three-dimensional simulation of a small earthquake.

Most of the source models discussed in the literature are elastodynamic models. That is, the earthquake source is characterized as a radiator of elastic waves and the non-linear processes near the fault are not explicitly treated. The formulation of these models is essentially analytical, though machine calculations may be required to evaluate some of the expressions. On the other hand, numerical techniques (finite difference or finite element) have the potential capability to model fine details of the rupture process. There are at least three important applications for which such detailed models can be used:

1. As a research tool, to develop an understanding of the details of the rupture process.
2. As a research tool, to verify and extend the assumptions and approximations made in developing analytical elastodynamic models.
3. To numerically simulate earthquake ground motion in the near-field, strong motion regime where

analytical approximations are unavailable or unapplicable. The applications are either for research or directly to earthquake engineering problems of immediate interest.

There have been a few attempts to simulate earthquake faulting with numerical techniques. The work of Dieterich (1973), Andrews (1975), and Geller and Frazier (1976) is known to us. Cherry, et al., (1976) incorporated a two-dimensional (plane strain) stick-slip rupture model into a finite difference code. The model used here is essentially a three-dimensional extension of this earlier model.

The results presented in this report may be viewed in three parts. First, we describe the numerical earthquake simulation, showing that plausible and intuitively appealing behavior occurs in the fault vicinity. Second, the earthquake generated elastic wave field is decomposed into a unique and exact (in a homogeneous space) equivalent elastic point source. The ability to obtain such an equivalent source from the results of a finite difference calculation is an important step because it allows a linkage between the numerical codes and the analytical elastic wave propagation techniques of theoretical seismology. Finally, we compare our earthquake source to equivalent events from volume- and dislocation-type elastodynamic models. The interesting result is that as a radiator of elastic waves our source is much more like the volume source model.

3.2 MODELING PROCEDURE

In order to develop a numerical model for simulating the earthquake faulting process it is necessary to specify:

1. The region in which faulting is to occur.
2. The constitutive behavior of the material in the vicinity of the fault.

3. The condition for rupture initiation.
4. The criterion controlling adjustment of the stress field during rupture.
5. A criterion allowing the rupture to heal.

All earthquake models must, implicitly or explicitly, deal with these five items.

Finite difference techniques allow almost unlimited freedom for modeling earthquake faulting as outlined above. The restrictions are generally economic rather than technical. In this section we wish to describe a specific model we chose to study, but also to point out the generality of the method and the alternative choices that can be made.

A three-dimensional finite difference earthquake model was developed based on experience with two-dimensional modeling studies. The basic difference equations are similar to those reported by Cherry, et al. (1970). The stick-slip rupture model is an extension of that used by Cherry, et al. (1976), in a study of the ground motion from two-dimensional (plane strain) earthquake faulting. The numerical scheme for solving the differenced form of the governing differential equations incorporates explicit time stepping for updating the stress. Details have been presented in Section II.

The geometry for the calculation is indicated in Figure 3.1. A rectangular fault, $1.0 \times 0.6 \text{ km}^2$, was specified as the surface on which slip was to be allowed. That is, a discontinuity in X-displacement was allowed across this surface. It is clear that some nonlinear mechanism must be postulated for the region adjacent to the slip surface. In fact, on the edges of this surface the strain is unbounded. The questions that must be addressed are: What is the nonlinear material behavior in the fault zone? What is the

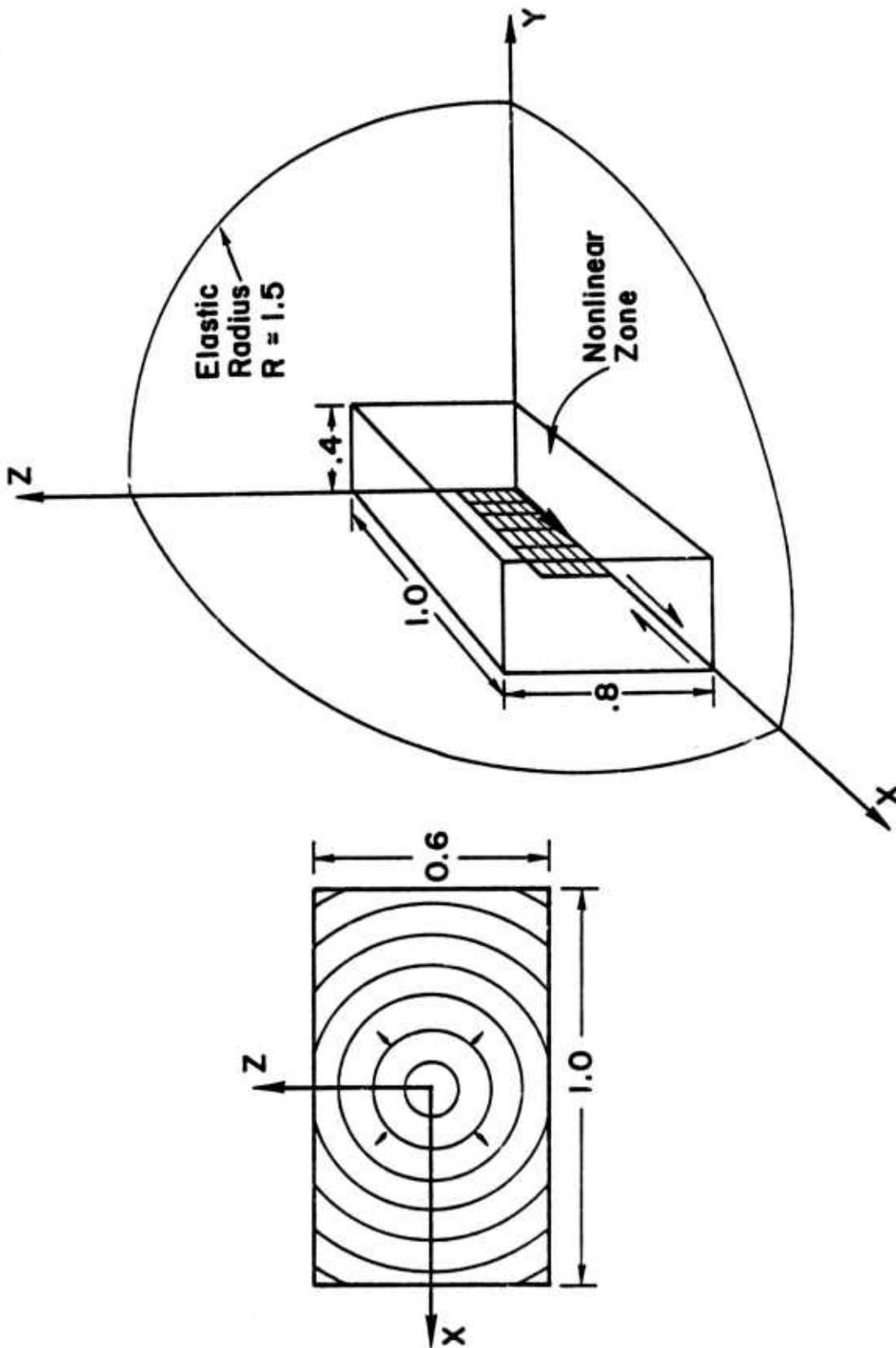


Figure 3.1. Geometry for the finite difference earthquake simulation. The fault plane on which the rupture radiates symmetrically is shown on the left. The first octant of the grid is depicted on the right including the dimensions of the "nonlinear zone" and the "elastic radius".

extent of the fault zone; that is, how large is the region in which material nonlinearities are important?

The fault zone was specified to be a rectangular parallelepiped $2.0 \times 1.6 \times 0.8 \text{ km}^3$ as indicated in Figure 3.1. Outside this zone the material behavior was linear elastic. The elastic P and S wave velocities are $\alpha = 5.7 \text{ km/sec}$ and $\beta = 3.4 \text{ km/sec}$. The density is $\rho = 2.8 \text{ gm/cm}^3$ and the shear modulus is $\mu = 324 \text{ kbar}$. In the fault zone, elastic-plastic material response consistent with a von Mises yield criterion was allowed. That is, if the second deviatoric invariant (J'_2) is greater than a specified value, then

$$S_{ij} = \hat{S}_{ij} \frac{Y}{\sqrt{3J'_2}}, \quad J'_2 > \frac{Y^2}{3}, \quad (3.1)$$

where \hat{S}_{ij} is the stress deviator tensor, S_{ij} is the adjusted stress deviator and

$$J'_2 = \frac{1}{2} \hat{S}_{ij} \hat{S}_{ji}. \quad (3.2)$$

For a triaxial test Y corresponds to the maximum stress difference at failure.

Another important feature of the calculation are the grid dimensions for the finite difference mesh. All zones were cubes, 100 meters on a side. Then the fault surface itself is 6×10 grid dimensions while the fault zone includes $20 \times 16 \times 8$ grid dimensions. With a grid this coarse stress waves with frequencies greater than 3-5 Hz are not propagated accurately and this must be considered when evaluating the results. In order to obtain an equivalent elastic source (described in a subsequent section), it was necessary to propagate the full time history of the earthquake generated ground motion to some elastic radius. This

was selected to be at 1.5 km as indicated in Figure 3.1. The time step (which is controlled by the grid dimensions) was 0.005 seconds and 225 time steps were required to complete the problem. Taking advantage of the symmetry of the problem, the calculation was actually run for only a quadrant of the whole space, that where X and Z are positive. A detailed description of the symmetry conditions imposed on the boundary of the finite difference grid appears in Savino, et al. (1975), Appendix A.

The elastic-plastic stress-strain behavior is one of the simplest nonlinear mechanisms that can be introduced to dissipate the stress concentrations at the edges of the dislocation. Certainly, the size of the fault zone and the constitutive behavior of the material within this zone are important parameters of the calculation. While the finite difference formulation allows great freedom in how they are specified, we made this relatively simple choice as being most appropriate for our first three-dimensional calculation.

How is rupture to be initiated? In the two-dimensional earthquake simulations by Cherry, et al. (1976), rupture initiation was controlled by a criterion based on the amount of plastic work accumulated at a location on the fault surface. However, the rupture velocity was found to be nearly constant. Then a simpler though nearly equivalent criterion is to specify the rupture velocity and this was the procedure followed in the calculation described here. The rupture was assumed to grow symmetrically with velocity $V_R = 2.7$ km/sec (80 percent of the shear wave velocity) until reaching the boundary of the specified fault surface. The fault growth pattern is indicated in Figure 3.1. The prestress was assumed to be pure shear: $\sigma_{xy}^{(0)} = 1.0$ kbar. Therefore, in the coordinate system of Figure 3.1, the faulting is bilateral and the event is right-lateral strike-slip.

The next question to be answered is: How does the stress field adjust during rupture? Initially, all the material in the fault zone was specified to be on the fault surface. In view of (3.1) this means $\gamma = \sqrt{3J_2}$ or $\gamma = \sqrt{3}$ kbar since at the beginning of the calculation $J_2' = \sigma_{xy}(0)^2 = 1.0 \text{ kbar}^2$. Then all the material in the fault zone flows plastically when J_2' increases beyond its initial value. However, this increase in J_2' , leading to plastic flow, will be restricted to the region around the tip of the fault since elsewhere the effect of the rupture is to relax the shear stress from its initial value. At the time of rupture initiation, grid points on opposite sides of the fault surface are uncoupled and allowed to slip as the tangential stress is relaxed (over three time steps) to its kinetic friction value which was taken to be 0.85 kbar. The nominal dynamic stress drop is then $\Delta\sigma = 1.0 - 0.85 \text{ kbar} = 150 \text{ bars}$. A given location on the fault sticks when there is a reversal in relative velocity between points on opposite sides of the fault.

The tangential stress at several locations on the fault surface is plotted in Figure 3.2 at nine time points at which the grid was monitored. We see that the stress can build up slightly before rupture initiation at which time it is relaxed to 0.85 kbar. After the fault is tied the stress continues to change before reaching its static value. The static values vary over the fault surface from 0.77 - 0.91 kbar with the average value being 0.854 kbar. Therefore, the average static stress drop is 146 bars, quite close to the nominal $\Delta\sigma$ of 150 bars.

In Figure 3.3 is plotted the X-displacement corresponding to the tangential stress of Figure 3.2. Once again, the sampling is only at nine evenly spaced time points. However, we do know the time of rupture initiation at each point. Taking this into account, we see that the displacement time history on the fault is consistent with a simple ramp with a rise

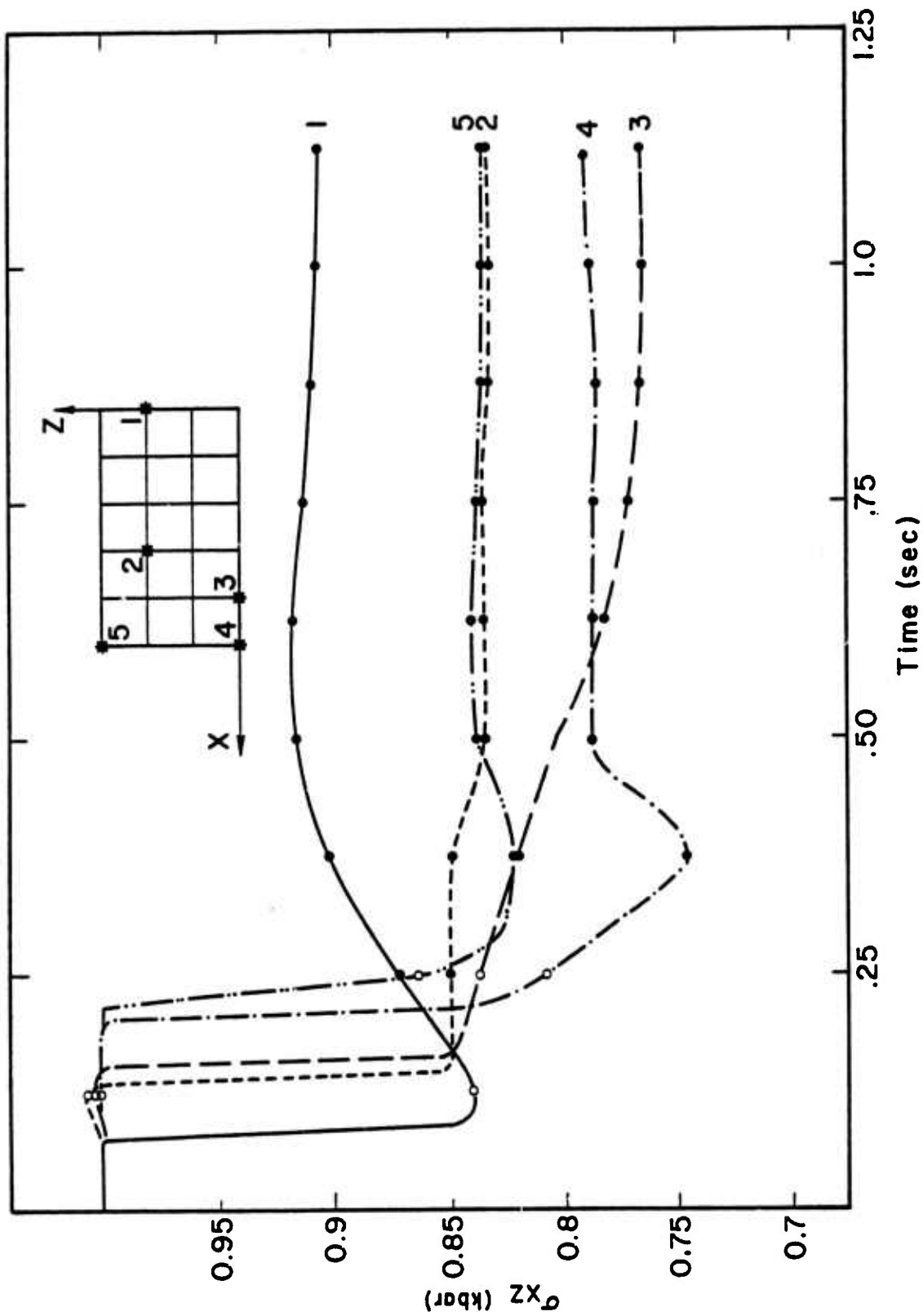


Figure 3.2. The time history of tangential stress at five locations on the fault surface (see inset). The σ_{xy} is sampled at the nine indicated time points. The connecting lines are then approximate. Closed circles indicate that the fault is tied.

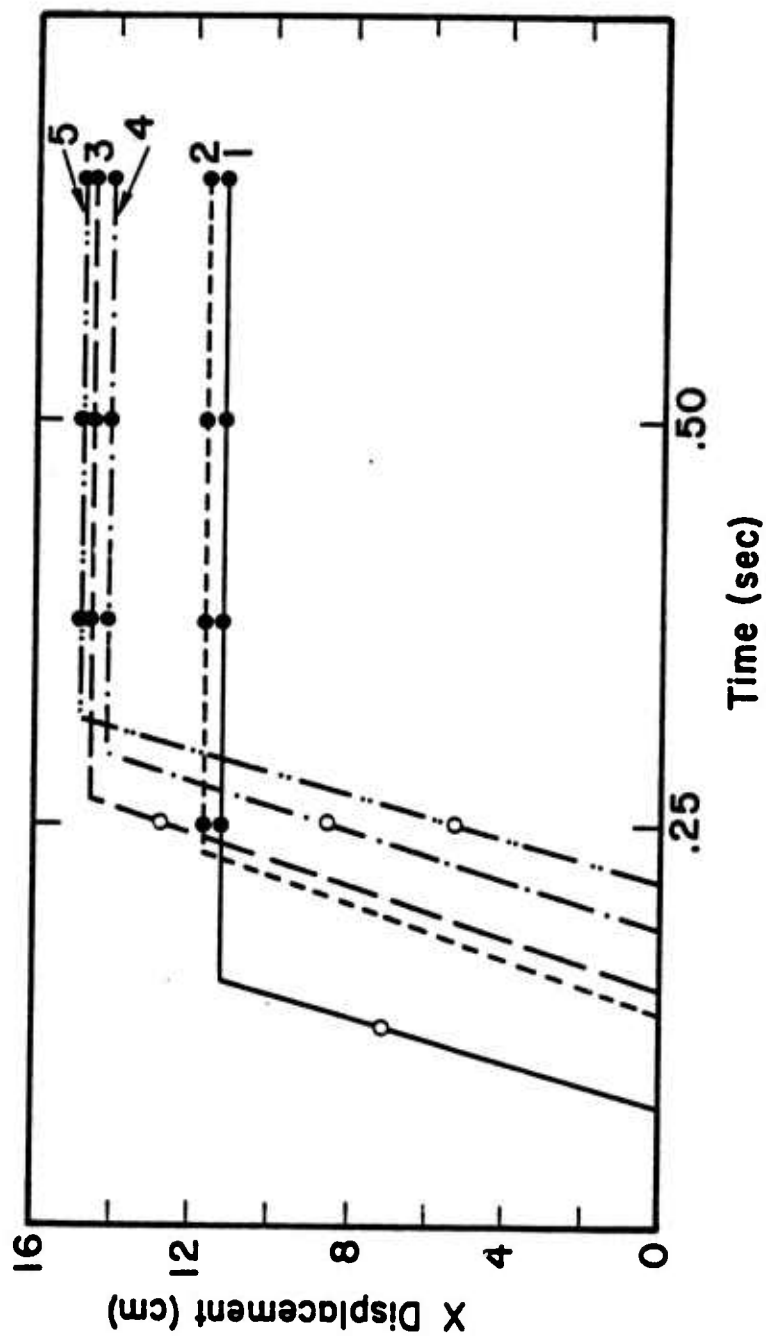


Figure 3.3. The X displacement (half the fault offset) corresponding to the tangential stress in Figure 3.2.

time of 0.08 - 0.10 seconds, depending on position. This interpretation has been used to draw the curves in the figure. We caution that we do not mean to infer that these curves show the actual time history of displacement, only that the known values are consistent with this simple model.

At the beginning of this section we listed five items that must be specified for a deterministic earthquake faulting model. In specifying these items we have chosen to keep the problem as simple as possible, consistent with the physics as we understand it. The result is a rupture process characterized by a rather complex adjustment of the tangential stress across the fault (Figure 3.2), but a relatively simple time history of displacement on the fault surface. In the way "dislocation" models of earthquake faulting are usually formulated (e.g., Haskell, 1964), displacement time histories very much like those in Figure 3.3 are specified on the fault surface. In using such models, little attention is generally given to the time history of shear stress on the fault. In our model the adjustment of the shear stress (Figure 3.2) is clearly influenced by the nonlinear material behavior in the fault zone.

As pointed out above, the rupture process in our finite difference model is rather similar to that assumed in constructing the dislocation-type models of earthquake faulting of which there are many examples in the literature (e.g., Haskell, 1964; Savage, 1966; Brune, 1970; Dahlen, 1974; Richards, 1976). One difference is the plastic flow allowed in the fault zone to relieve the stress concentrations that occur at the crack edges. Another difference is that the fault surface does not remain plane, but is warped as is seen in Figure 3.4. There the out-of-plane (Y) displacement of the fault is shown versus position at the last time step and at nine snapshots in time for the displacements on the X-axis. The maximum out-of-plane displacements are at the end of the fault where they are as much as

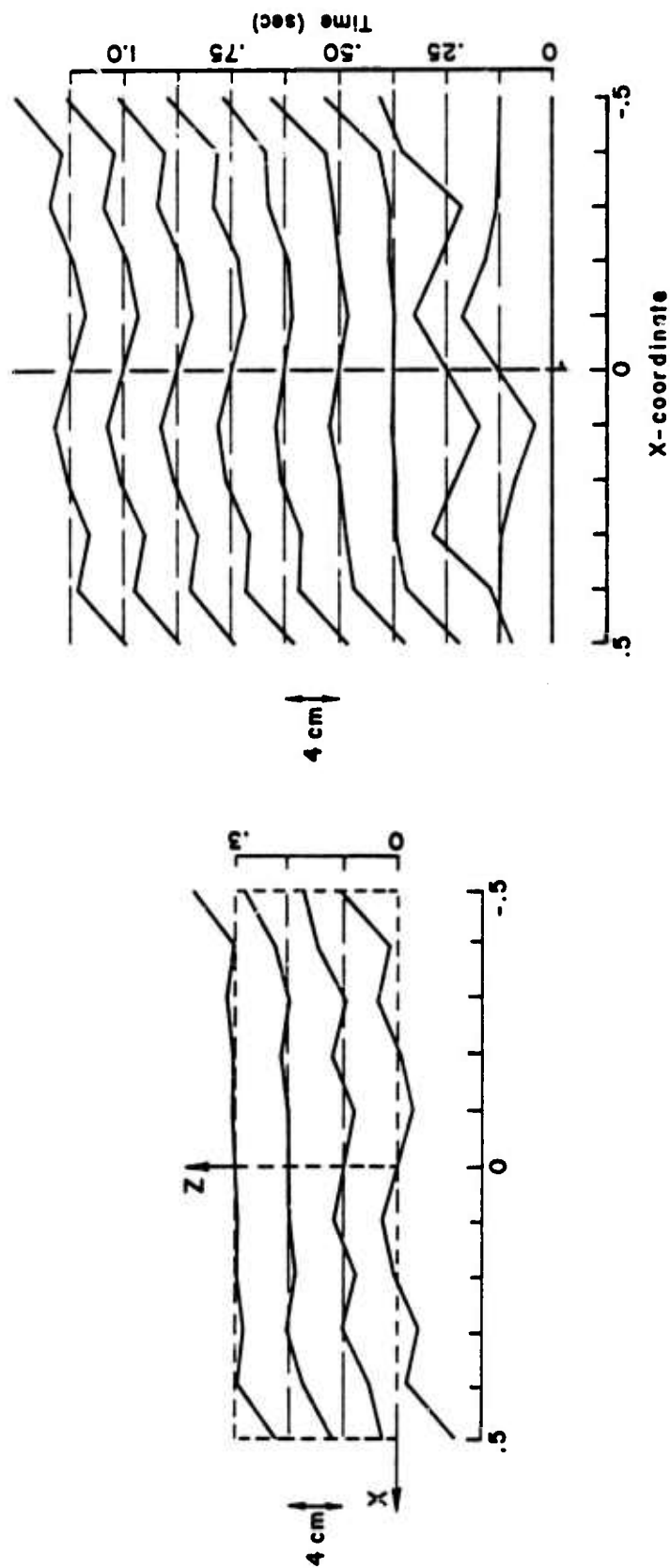


Figure 3.4. The out-of-plane (Y) displacement of the fault surface. On the left are shown the displacements on half the fault at the last time step. The displacements are symmetric about the X axis and antisymmetric about Z. On the right the time history is depicted via nine snapshots of the displacements on the fault centerline, the X axis.

5 cm or approximately 20 percent of the average fault offset.

Our primary interest in this paper is in the source as a radiator of seismic waves. As a first indication of the character of the radiated field, some typical velocity and displacement time histories are shown in Figure 3.5 at two stations 1.5 km from the center of the fault. In these time histories much of the complexity can be attributed to the fact that near- and far-field P and S wave effects are all represented. In the next section the outgoing wave field is represented in equivalent elastic source form from which it can be decomposed into its various components.

3.3 EQUIVALENT ELASTIC SOURCE REPRESENTATION

Finite difference methods are useful for modeling details of the rupture physics but are not practical for propagating the resulting seismic waves very far from the fault. In the seismic wave (linear elastic wave propagation) regime the analytical techniques of theoretical seismology are generally much more efficient and economical. In order to bridge the gap between complex source calculations such as that described in the previous section and elastic wave propagation theories, it is necessary to construct an equivalent elastic source. As was pointed out by Bache and Harkrider (1976), a convenient equivalent source can be obtained by expanding the outgoing elastic wave field in spherical harmonics. The procedure is briefly outlined below.

The Fourier transformed equations of motion in a homogeneous, isotropic, linear elastic medium may be written

$$\bar{\mathbf{u}} = - \left(\frac{1}{k_\alpha^2} \right) \nabla \bar{\chi}^{(4)} + \left(\frac{2}{k_\beta^2} \right) \nabla \times \bar{\chi} \quad (3.3)$$

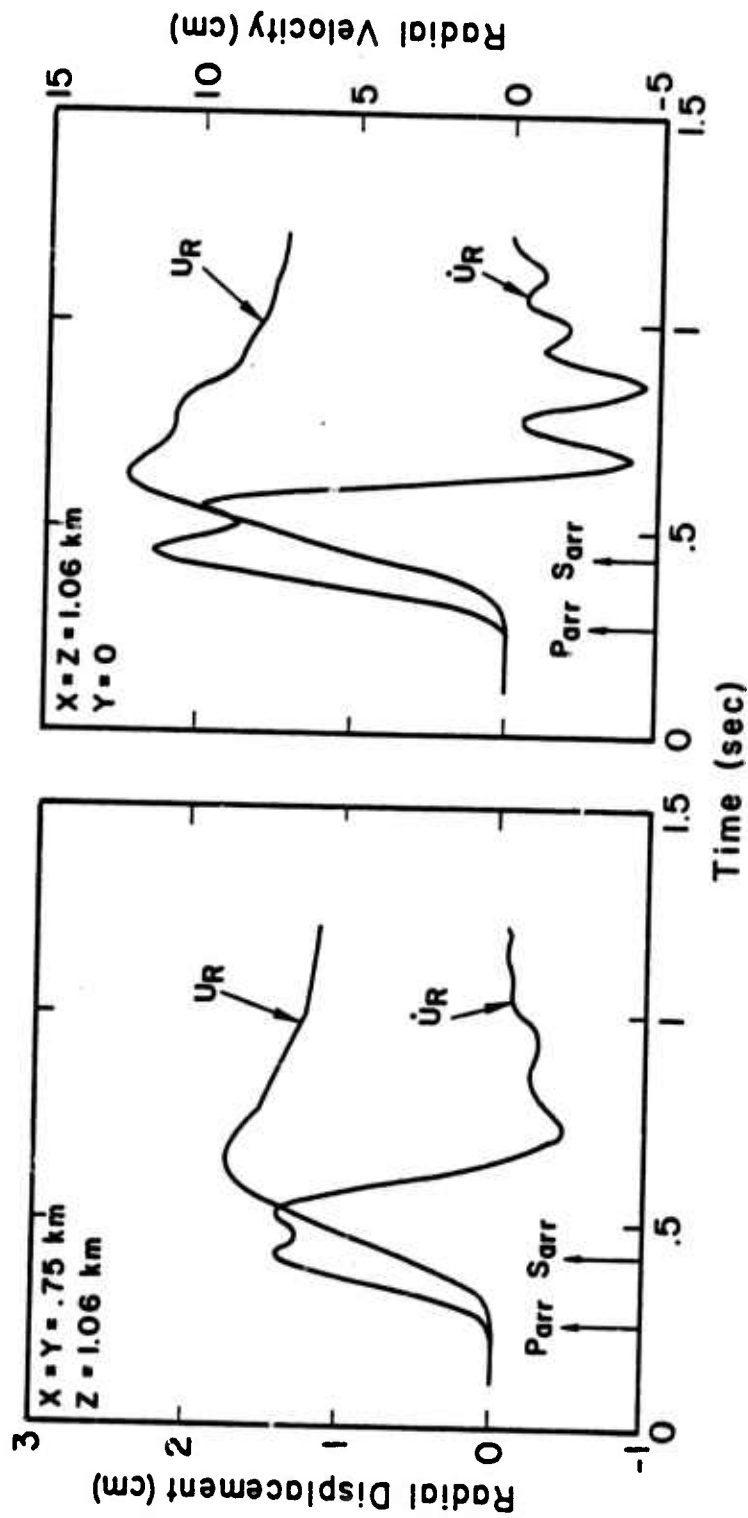


Figure 3.5. The radial velocity and displacement time histories at two stations on the elastic radius. The position of the stations is indicated on the figures: The left plot is for the station in the center of the first octant; the right plot is for a station in the XZ plane, 45° from each axis. The indicated times, $Parr = 1.5/\alpha$ and $Sarr = 1.5/\beta$, are the earliest times at which undispersed elastic waves can arrive from the point of rupture initiation.

where \bar{u} is displacement and k_α and k_β are the compressional and shear wave numbers. The Cartesian potentials $\bar{\chi}^{(4)}$ and $\bar{\chi}$ are defined by

$$\begin{aligned}\bar{\chi}^{(4)} &= \nabla \cdot \bar{u} , \\ \bar{\chi} &= \frac{1}{2} \nabla \times \bar{u} .\end{aligned}\tag{3.4}$$

The potentials can be shown to satisfy wave equations and therefore can be expanded in spherical eigenfunctions as follows:

$$\begin{aligned}\bar{\chi}^{(j)}(R, \omega) &= \sum_{\ell=0}^{\infty} h_{\ell}^{(2)}(k_j R) \sum_{m=0}^{\ell} \left[A_{\ell m}^{(j)}(\omega) \cos m\phi \right. \\ &\quad \left. + B_{\ell m}^{(j)}(\omega) \sin m\phi \right] P_{\ell}^m(\cos \theta), \quad j = 1, 2, 3, 4\end{aligned}\tag{3.5}$$

where $k_4 \equiv k_\alpha = \omega/\alpha$ and $k_i \equiv k_\beta = \omega/\beta$ for $i = 1, 2, 3$. The $h_{\ell}^{(2)}$ are spherical Hankel functions of the second kind and the P_{ℓ}^m are associated Legendre functions. The vector R has as components the usual spherical coordinates R, θ, ϕ , referred to the Cartesian system of Figure 3.1.

Equations (3.5), together with (3.3), provide an elastic point source representation of the (outgoing) displacement field. The values of the multipole coefficients, $A_{\ell m}^{(j)}(\omega)$, $B_{\ell m}^{(j)}(\omega)$, $j = 1, 2, 3, 4$, prescribe the displacement field at all points in the homogeneous medium where (3.3) applies. Therefore, this is a convenient source form for studying whole space radiation properties, decomposing the field into near- and far-field components, etc. Minster (1973) gives an extensive discussion of the manipulation of sources given in this form including formulas for rotating the source to any desired orientation with respect to a fixed coordinate system. Further, Harkrider and Archambeau

(1976) and Bache and Harkrider (1976) have derived the theory for computing surface and body waves in layered media for sources given in terms of multipole coefficients.

Using the orthogonality of the spherical harmonics, the multipole coefficients are related to the potentials, $\bar{\chi}^{(j)}$, by

$$\begin{pmatrix} A_{\ell m}^{(j)}(\omega) \\ B_{\ell m}^{(j)}(\omega) \end{pmatrix} = \frac{C_{\ell m}}{h_{\ell}^{(2)}(k_{\alpha} \hat{R})} \int_0^{2\pi} \int_0^{\pi} \bar{\chi}^{(j)}(R, \omega) P_{\ell}^m(\cos \theta) \begin{pmatrix} \cos m\phi \\ \sin m\phi \end{pmatrix} \sin \theta d\theta d\phi, \quad (3.6)$$

where

$$C_{\ell m} = \frac{(2\ell+1)(\ell-m)!}{2\pi(\ell+m)!}, \quad m \neq 0$$

$$C_{\ell 0} = (2\ell+1)/4\pi,$$

and \hat{R} is a radius defining a spherical surface on which the integral (3.6) is to be computed. For the finite difference earthquake calculation discussed here, the divergence and curl of the displacement field were monitored at $\hat{R} = 1.5$ km, the "elastic radius" indicated in Figure 3.1. Since a Cartesian grid was used, the actual implementation required a linear interpolation to the spherical surface from nearby grid points. Details of the algorithm for computing the integrals (3.6) from finite difference code output are given in Appendix G of Bache, et al. (1975). The tractability of the surface integrand in (3.6) is clearly dependent on the behavior of the curl and divergence as functions of θ and ϕ . For this earthquake calculation these quantities were quite smooth and well-behaved.

Due to the symmetry of the source, only even order ($\ell = 0, 2, 3, \dots$) multipoles are nonzero. The odd order terms are associated with unilateral propagation effects. The $\ell = 2$ terms represent the quadrupole or double-couple radiation field generated by the source while the higher order terms are perturbations on the double-couple field introduced by propagation effects. Also, there is a single monopole term, $A_{00}^{(3)}(\omega)$, which represents a spherically symmetric rotation about the Z-axis. The monopole shear term arises as a consequence of the out-of-plane rotation of the fault surface (Figure 3.4). As expected from the requirement for the source region to reach static equilibrium, this term vanishes at long time.

The amplitude of the monopole and largest of the quadrupole and octupole coefficients is plotted in Figure 3.6. Note that at low frequencies the source is dominated by the quadrupole terms. In fact these terms fall off with ω^2 at low frequencies while terms of other orders decay with higher powers of ω . At higher frequencies more and more terms are required to insure convergence of (3.5).

3.4 THE SEISMIC WAVE RADIATION CHARACTER OF THE SOURCE

Having the multipole coefficients, computation of displacement spectra at any location, \underline{R} , is a straightforward application of (3.3) and (3.5). Of course, it is necessary to compute enough terms so that (3.5) converges. In the sequel we will restrict attention to the far-field portion of the radiation field which is defined as that portion which decays as R^{-1} . Then the "P" and "S" wave portions of the wave field are conveniently separated with the first term of (3.3) giving the "P wave" and the second term giving the "S wave". In fact, it can easily be shown that:

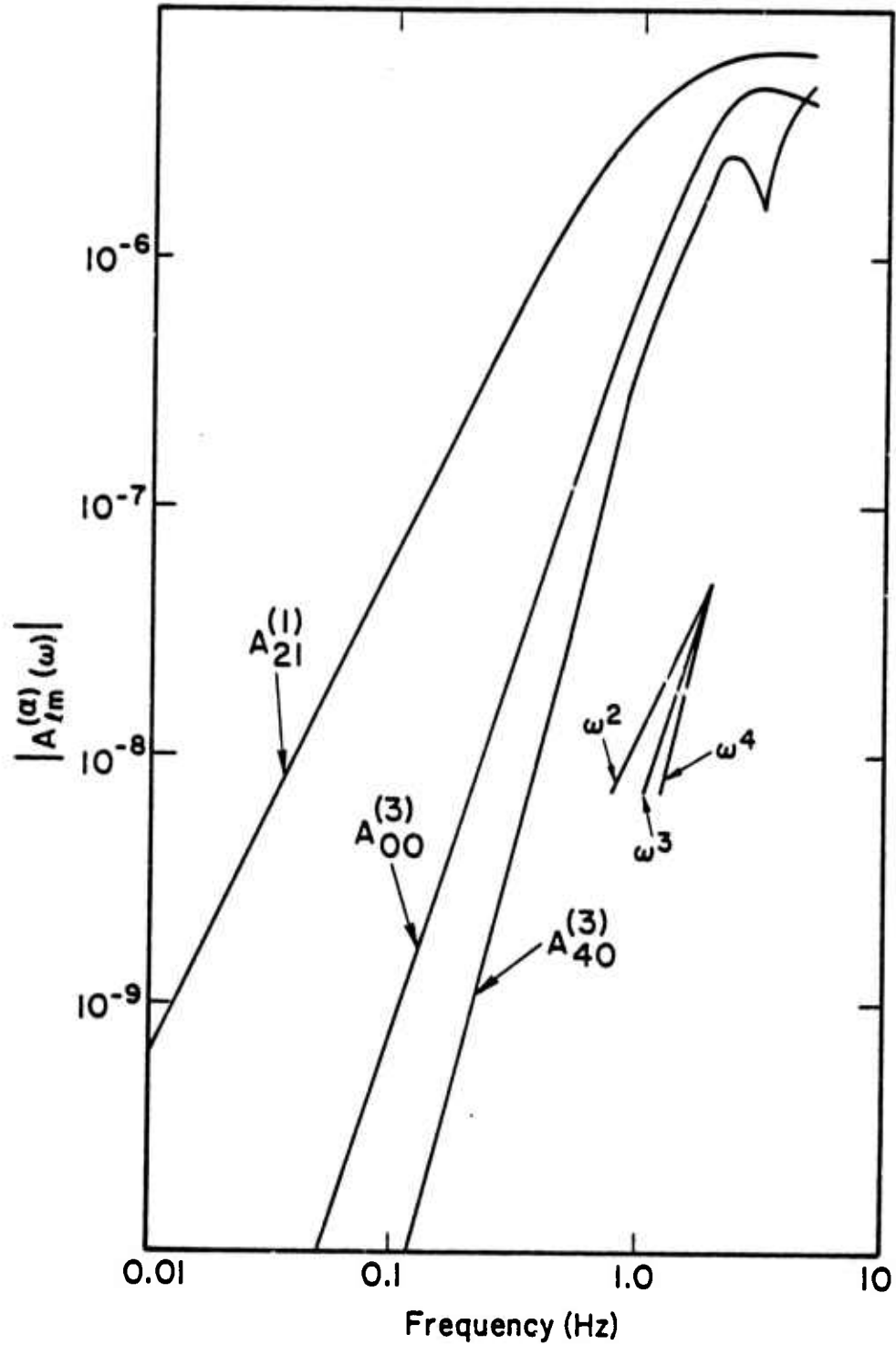


Figure 3.6. The amplitude of the monopole and largest quadrupole and octupole terms for the equivalent elastic source representation of our earthquake referred to the coordinate system of Figure 3.1.

$$\bar{u}_R(R, \theta, \phi, \omega) = -\frac{1}{k_\alpha^2} \frac{\partial \bar{X}^{(4)}}{\partial R},$$

$$\bar{u}_\theta(R, \theta, \phi, \omega) = \frac{2}{k_s^2} \left(\sin\phi \frac{\partial \bar{X}^{(1)}}{\partial R} - \cos\phi \frac{\partial \bar{X}^{(2)}}{\partial R} \right),$$

$$\begin{aligned} \bar{u}_\phi(R, \theta, \phi, \omega) = \frac{2}{k_s^2} & \left(\cos\theta \cos\phi \frac{\partial \bar{X}^{(1)}}{\partial R} + \cos\theta \sin\phi \frac{\partial \bar{X}^{(2)}}{\partial R} \right. \\ & \left. - \sin\theta \frac{\partial \bar{X}^{(3)}}{\partial R} \right), \end{aligned} \quad (3.7)$$

and the derivative with respect to R reduces to

$$\frac{\partial h_\ell^{(2)}(kR)}{\partial R} = i^\ell \frac{e^{-ikR}}{R}. \quad (3.8)$$

The geographic coordinate system and fault geometry for discussing the far-field stress wave radiation properties of the source are shown in Figure 3.7. Position with respect to the fault is denoted by a ray (A) specified by its azimuth (ϕ) and takeoff angle (τ), where $\tau = \pi - \theta$. The radial distance along A is denoted by R . With the coordinate system oriented as in Figure 3.7, the \bar{u}_R , \bar{u}_θ and \bar{u}_ϕ of (3.7) represent the P, SV and SH waves, respectively.

Far-field displacement spectra are shown in Figure 3.8 at two positions on the radiation pattern. The spectra were computed at $R = 1.5$ km but, in view of (3.8), can be scaled to any desired range. Terms through $\ell = 4$ were retained in the multipolar expansion. These are sufficient to insure convergence for the frequencies plotted. Note that the $\phi = 45^\circ$, $\tau = 45^\circ$ position is the same as the left plot in Figure 3.5 where total radial displacement and velocity were plotted.

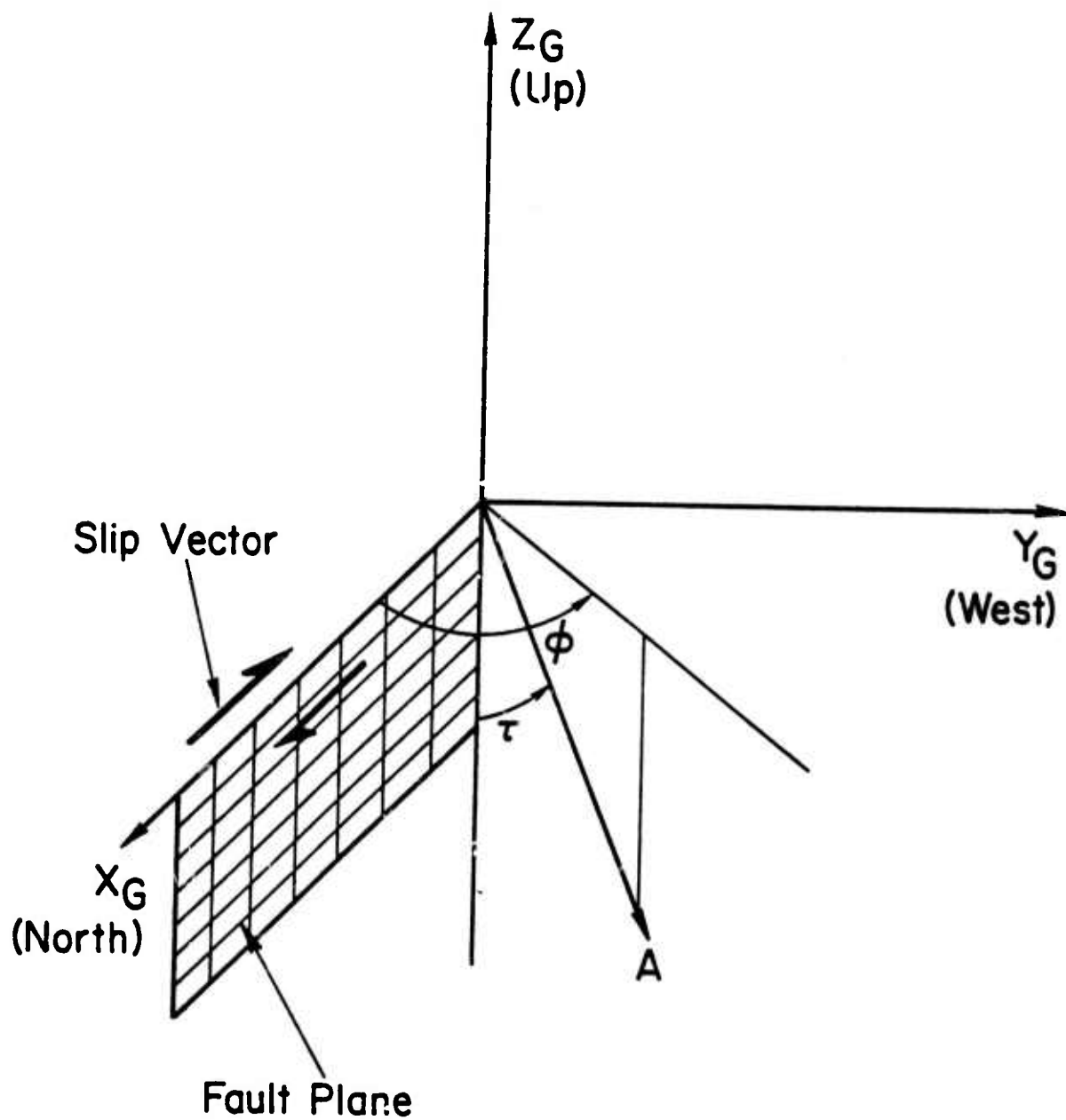


Figure 3.7. Orientation of the fault with respect to the geographic coordinate system.

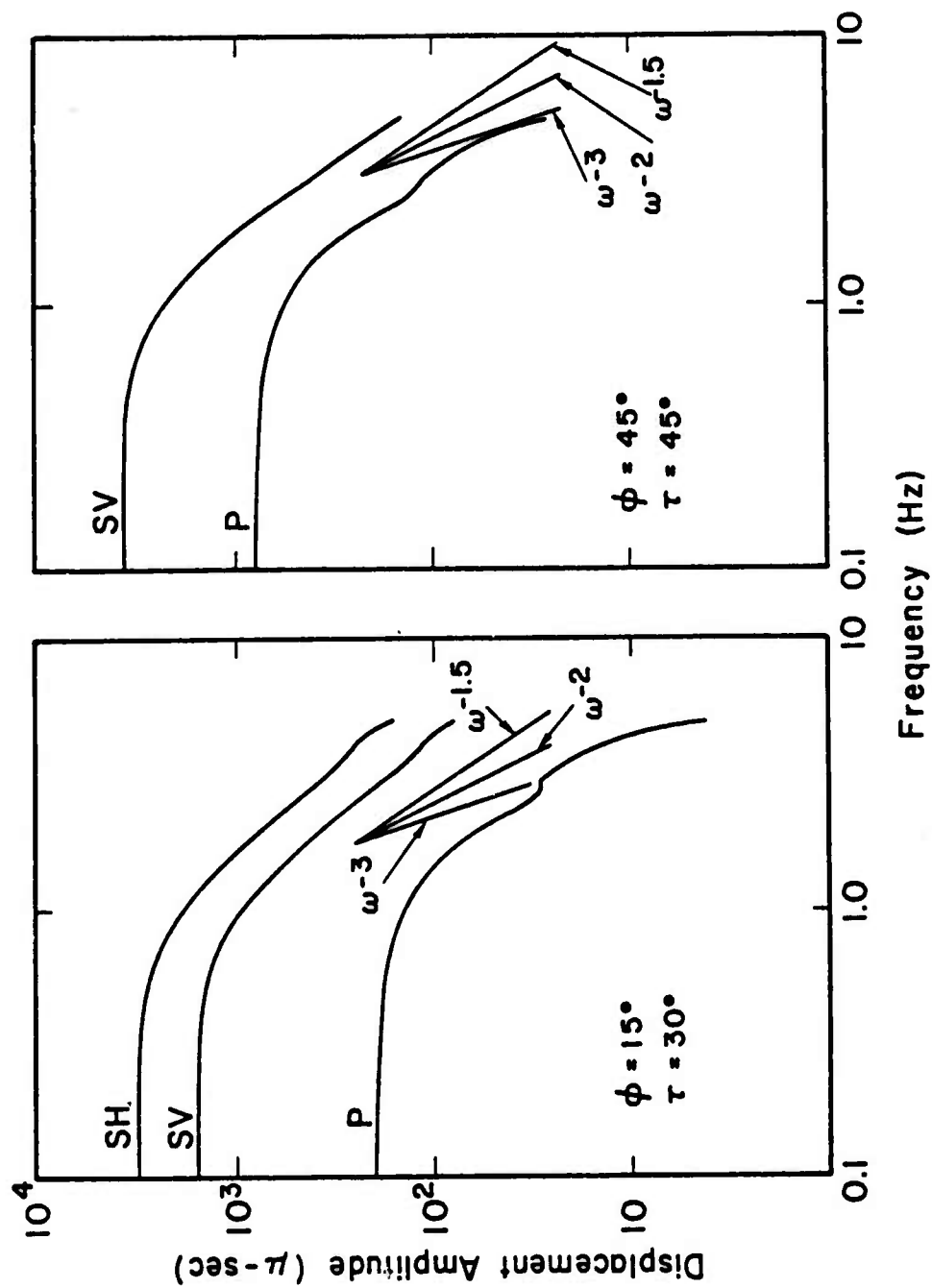


Figure 3.8. Far-field displacement spectra at two locations (specified by ϕ and τ) on the elastic radius ($R = 1.5$ km).

The spectra shown in Figure 3.8 are remarkably simple and can be characterized by three parameters; the long period level, the corner frequency and the logarithmic slope of the high frequency values. The long period level fixes the seismic moment for the event, a quantity that will be discussed in a later section. For the high frequency portion of the spectrum, recall that the grid dimensions impose the restriction that frequencies greater than 3-5 Hz are not propagated accurately. The highest frequencies are then contaminated to some degree by these effects which generally tend to increase the slope. Also, for these frequencies the spectra may still be in a transition region and one should take care when comparing to true high frequency asymptotes obtained from observations or analytic theories.

Corner frequency is a somewhat ambiguous quantity with a value that depends on the measuring technique. Blandford (1975) has suggested that the corner frequency be defined as that frequency at which the spectral value is half its low frequency limit. This definition allows a relatively precise determination of corner frequency and will be used here. Corner frequency is radiation pattern dependent as is indicated by the values given in Table 3.1. Note that for fixed r the corner frequency, P or S, decreases as the observer moves from a position normal to the fault ($\phi = 90^\circ$) toward the direction of rupture propagation ($\phi = 0^\circ$). The corner frequencies of Table 3.1 are all from one octant of the focal sphere, a sufficient sampling because of the source symmetry. Taking the average, the corner frequencies are 1.38 for the P wave and 1.20 for the S wave (SV or SH) with the deviations from these values being less than 0.1 Hz in all but a few cases. On the average, the P wave corner frequency is 1.15 times the S wave corner frequency.

The corner frequency is clearly associated in some way with the fault dimensions. Knowledge of the relationship

Table 3.1. Corner Frequencies at Various Positions on the Radiation Pattern

Wave Type	τ	30					45					90				
	ϕ	0	15	30	45	90	0	15	30	45	90	0	15	30	45	90
P		--	1.38	1.39	1.40	--	--	1.35	1.38	1.42	--	--	1.33	1.37	1.42	--
SV		--	1.19	1.20	1.24	--	--	1.14	1.19	1.24	--	--	--	--	--	--
SH		1.19	1.21	1.27	--	1.25	1.11	1.14	1.21	--	1.34	0.97	1.02	1.07	--	1.58

between the two affords an opportunity to obtain estimates of the fault dimensions from relatively sparse amounts of data. The usual assumption is that

$$D = \frac{C_{p,s}^\beta}{f_{p,s}}, \quad (3.9)$$

where D is the fault dimension, $f_{p,s}$ is the corner frequency and $C_{p,s}$ is a constant for P or S waves. For example, Brune (1970) suggests $C_s = 0.37$. For our computed source we find from the values of Table 3.1, using $D = 1.0$ km, that

$$C_p = 0.39 - 0.42, \quad (3.10)$$

$$C_s = 0.30 - 0.46.$$

Note that the $C_s = 0.46$ is an isolated point (SH waves at $\phi = \tau = 90^\circ$) and the second highest value is $C_s = 0.39$. The average values are $C_p = 0.41$ and $C_s = 0.35$.

From Figure 3.8 it seems clear that, no matter how they are determined, the average ratio of P to S corner frequencies (f_p/f_s) is greater than 1 for our model. This is consistent with the results from volume source models of earthquakes (e.g., Archambeau, 1968). We saw in the previous section, especially Figure 3.3, that in many respects the rupture process studied here behaves very much like that in a dislocation model. Peppin and Simila (1976) summarize the corner frequency characteristics of many of the proposed dislocation models. These authors point out that dislocation models with subsonic and uniform rupture propagation (like in our model) give $f_p/f_s < 1$ (Savage, 1972; Dahlen, 1974). On the other hand, those dislocation models that have $f_p/f_s > 1$ either have supersonic rupture velocity (Brune, 1970; Molnar, *et al.*, 1973; Burridge, 1975), variable rupture velocity (Berckhemer and Jacob, 1968) or slip concentrated near the center of the fault (Sato and Hirasawa,

1973; Madariaga, 1976). Why does our model exhibit corner frequency behavior more like these latter dislocation models and volume source models than a dislocation model such as that of Savage which is superficially more similar? We will return to this question in later sections where more extensive comparison to analytical models is made.

We complete our description of the far-field displacements from our finite difference earthquake source with the radiation patterns shown in Figure 3.9. Patterns are computed from (3.7) for three frequencies and two levels of truncation of the sum (3.5). In the top row only the monopole and quadrupole terms were retained. The octupole term was added for the patterns of the bottom row. Only the P and SH components are nonzero at $\theta = 90^\circ$. We observe that at low frequency the source is nearly pure double couple, with the only variation at 0.5 Hz being that slightly more SH waves are propagated normal to the fault (along Y_G) than in the fault direction (along X_G). At higher frequencies the monopole and higher order terms have greater effect, distorting both the P and SH patterns. Even for this small and rather simple event, terms other than the quadrupole have a significant effect on the short period (≤ 1 sec) energy radiated to the far-field.

The propagation of substantially larger SH waves to azimuths normal to the fault compared to azimuths along the fault (e.g., 50 percent larger at 1 Hz) is an interesting result. For the frequencies plotted, both the monopole and octupole act in this direction. To the extent that the monopole is responsible, the out-of-plane displacement of the fault surface is a major cause. However, the same thing can occur in models which have no such fault surface warping as will be seen in the following section for an analytical model. In this case the cause is interference between waves from either end of the bilateral fault.

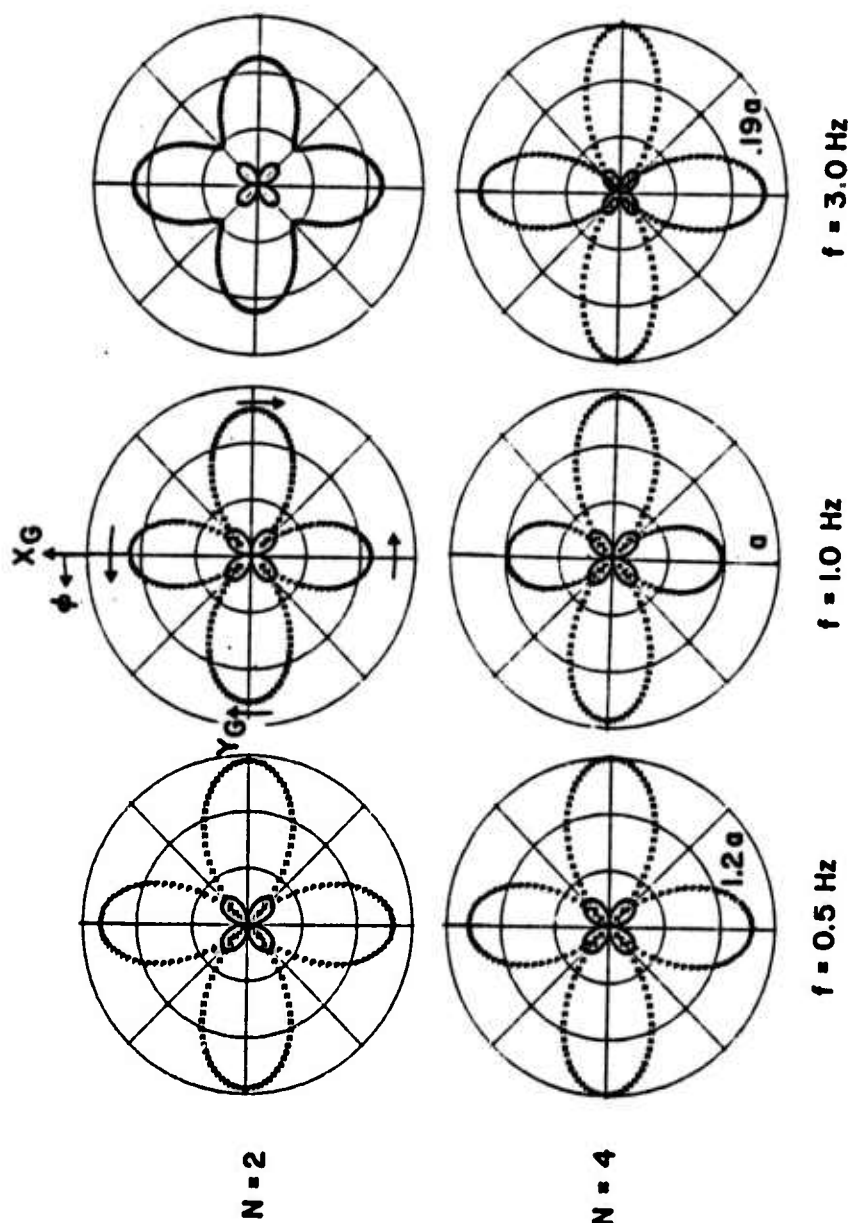


Figure 3.9. Far-field radiation patterns at three frequencies for the finite difference earthquake source. The patterns are for $\theta = 90^\circ$; that is, we plot the amplitude of the SH and P waves radiated in the X_G - Y_G plane. The coordinate system and first motion direction for the SH waves are indicated in the top middle plot. The two rows are for two levels of truncation (N) of the multipolar expansion. The amplitude of the outer ring for each frequency is indicated on the bottom row with $a = 9/R \text{ cm/km}$.

3.5 COMPARISON TO THE ARCHAMBEAU/MINSTER RELAXATION SOURCE MODEL

We saw in a previous section, especially Figure 3.3, that in terms of a kinematic view of the faulting, our finite difference model seems similar to dislocation models. On the other hand, the faulting process is initiated by the introduction of a weak zone in a prestressed medium and in that sense is similar to a relaxation model. Further, there is a finite volume within which nonlinear material response is allowed. In short, our finite difference source bears superficial similarities to both relaxation-volume source models and dislocation models. In the remainder of the paper we shall compare our results to those obtained from various forms of these analytical models.

The Archambeau/Minster elastodynamic source theory (Archambeau, 1968; Minster, 1973) describes the earthquake in terms of the relaxation of a pre-existing stress field about a zone of weakness in which the rigidity modulus vanishes. The theory has been cast in a computationally convenient form for several geometries in which the weak zone is formed by a growing and/or propagating spherical volume. The displacement field solutions for the Archambeau/Minster source theory are given directly in terms of the multipolar expansion (3.5). Since we have described our finite difference earthquake source in the same form, comparison between the two is conveniently accomplished.

Formulation of the Archambeau/Minster source model requires specification of α and β , the elastic wave velocities; V_R , the rupture velocity; and $S^{(0)}$, the prestrain which is equal to the ratio of prestress ($\sigma^{(0)}$) to shear modulus (μ). To control the growth of the weak zone we specify two lengths, $R(t)$ and $d(t)$, which are functions of time. The $R(t)$ is the radius of the spherical volume of vanishing rigidity, while $d(t)$ is the distance of the center of this sphere from the origin. Then $R(t) + d(t)$

grows steadily with velocity V_R . The parameter R_s , introduced by Archambeau to represent the dimension of the pre-stressed region, will be infinite and play no part in the solution.

Three source geometries are of interest:

1. Stationary expanding sphere: If we set $d(t) = 0$, the spherical region expands uniformly about its center point. This form of Archambeau's model has been used (Archambeau, 1972; Archambeau and Sammis, 1970; Bache, 1976) in a number of studies of the tectonic strain release associated with large underground explosions.
2. Tangentially expanding sphere: If $d(t) = R(t)$, the spherical region expands from a fixed point on the boundary. The radiation field from this geometry is extensively discussed by Minster (1973).
3. Growing and propagating sphere: The $d(t)$ and $R(t)$ can take any functional form subject to the restriction that $d(t) + R(t) = V_R t$.

For comparing with our finite difference earthquake the selection of appropriate values for most of the parameters is obvious. We take $\alpha = 5.7$ km/sec, $\beta = 3.4$ km/sec and $V_R = 2.7$ km/sec. Since the stress drop is total in the analytic model, we take $\sigma^{(0)} = 150$ bars or $S^{(0)} = 4.63 \times 10^{-4}$. Specification of the weak zone dimensions depends on the model. Also, we must account for the fact that the finite difference fault is bilateral.

The simplest comparison is made by using the stationary expanding sphere, model 1 above, and associating the diameter with the fault length (L) of 1.0 km. That is, let $R(t)$ grow with velocity V_R to a maximum of 0.5 km. This source approximates our bilateral fault in the sense that it is

growing equally in all directions. However, the source is a pure double-couple; there are no higher order terms representing the interference between waves originating in different regions of the fault.

In Figure 3.8 were shown far-field displacement spectra for our finite difference earthquake. The same quantities were computed for the stationary expanding sphere model described above and the two are compared for $\tau = 30^\circ$, $\phi = 15^\circ$, in the left plot in Figure 3.10 which is typical of the entire radiation pattern.

The results of this first comparison are simply summarized: The long period level and relative excitation of P, SV and SH waves agree almost exactly while the corner frequency is considerably higher for the analytical model. As pointed out by Minster (1973), the long period level for either of the expanding sphere models is controlled by the strain drop ($S^{(0)}$) and the volume of the final sphere ($\approx L^3$). The corner frequency depends on V_R/L .

The natural question to ask is: How much is the short period portion of the spectrum influenced by propagation (interference) effects? The tangentially expanding sphere is the simplest Archambeau/Minster model that includes the effects of asymmetric rupture propagation. To simulate a bilateral rupture we need to use two such models, one with the rupture traveling to the right (S_R) and one with it traveling to the left (S_L). To maintain the long period spectrum at the proper level we take $L = 1.0$ km in both models and obtain the bilateral fault (S_B) from $S_B = (S_R + S_L)/2$. As a result, S_B consists of the even order multipoles ($\ell = 2, 4, 6, \dots$) from S_R or S_L while the odd order ($\ell = 3, 5, 7, \dots$) multipoles drop out.

The comparison of the finite difference earthquake spectra and the bilateral model described above is shown

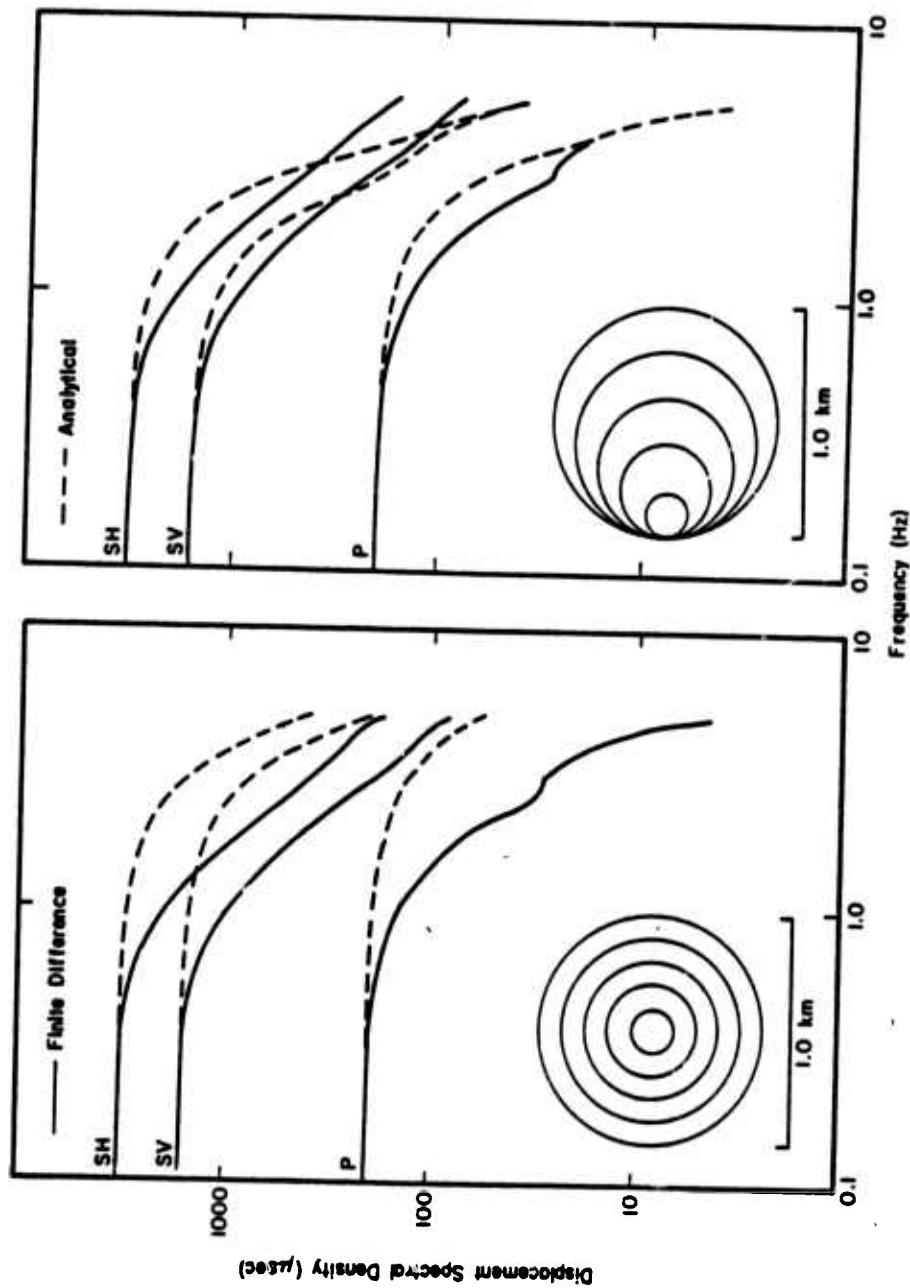


Figure 3.10. Far-field displacement spectra at $R = 1.5$ km, $\phi = 15^\circ$, $\tau = 30^\circ$, for the finite difference model compared to the Archambeau/Minster model with two source geometries. The diameter of the growing spherical volume is indicated at five equally spaced time steps from 0 to 1.0/2.7 sec. Modification of the unilateral rupture (right) to represent a bilateral rupture is described in the text.

on the right in Figure 3.10. The agreement between long period spectra is again nearly exact. We see that addition of the higher order interference terms does considerably enhance the agreement in the short period region. Substantial disagreement between the two models seems to be restricted to the vicinity of the corner frequency where the analytical model breaks much more sharply to its high frequency slope.

Since both the analytic and finite difference source models are given in multipolar form, the most detailed comparison is via the multipole coefficients. To the extent that these agree, the entire radiation pattern, near- and far-field, is the same. Comparison of the amplitudes of the multipoles (for the fault orientation of Figure 3.7) is shown in Table 3.2 at three points in the low, intermediate and high frequency range. For both the finite difference model (FD) and the analytical model (TES) we show the values of the nonzero coefficients, through the octupole, normalized to the leading term, $A_{21}^{(1)}$ (FD), for the finite difference model.

From Table 3.2 it is clear that at low frequency the FD source is essentially a pure double-couple and is nearly identical to the TES source. Agreement between the two is increasingly worse as frequency increases. A notable feature of the high frequency FD values is the importance of the out-of-plane fault displacement terms $A_{00}^{(3)}$ and $A_{20}^{(3)}$ which do not appear in the analytical solution. From this comparison we would expect the radiation patterns for the two sources to be substantially the same at low frequencies and differ as frequency increases. This is illustrated in Figure 3.11 where patterns for the TES that are directly comparable to the FD patterns of Figure 3.9 are shown.

The availability of an analytical model that has an equivalent source with so many features in common with our FD equivalent source is quite useful in attempting to

Table 3.2. Comparison of Multipole Coefficients for the Finite Difference Earthquake (FD) to Those from the Analytical Bilateral Fault Constructed from the Archambeau/Minster Tangentially Expanding Sphere (TES)*

Frequency (Hz)	0.1		1.0		5.0	
$A_{lm}^{(\alpha)} / A_{21}^{(1)}$ (FD)	FD	TES	FD	TES	FD	TES
Monopole $A_{00}^{(3)}$	0.01	0	0.21	0	0.63	0
Quadrupole $A_{21}^{(1)}$	1.00	0.97	1.00	0.89	1.00	0.42
$B_{21}^{(2)}$	1.01	0.97	1.13	0.89	0.67	0.42
$A_{20}^{(3)}$	0.06	0	0.32	0	0.84	0
$A_{22}^{(3)}$	1.04	0.97	1.09	0.89	0.46	0.42
$B_{22}^{(4)}$	0.16	0.15	0.19	0.15	0.19	0.05
Octupole $A_{41}^{(1)}$	-	-	0.02	0.05	0.27	0.26
$A_{43}^{(1)}$	-	-	-	-	0.01	0.02
$B_{41}^{(2)}$	-	-	0.03	0.02	0.27	0.09
$B_{43}^{(2)}$	-	-	-	-	0.01	0.02
$A_{40}^{(3)}$	-	-	0.11	0.07	0.75	0.36
$A_{42}^{(3)}$	-	-	-	0.01	0.07	0.06
$A_{44}^{(3)}$	-	-	-	-	0.01	0.02
$B_{42}^{(4)}$	-	-	-	-	0.01	0.02
$B_{44}^{(4)}$	-	-	-	-	-	-

* The dashed entries signify a nonzero value less than 0.01.

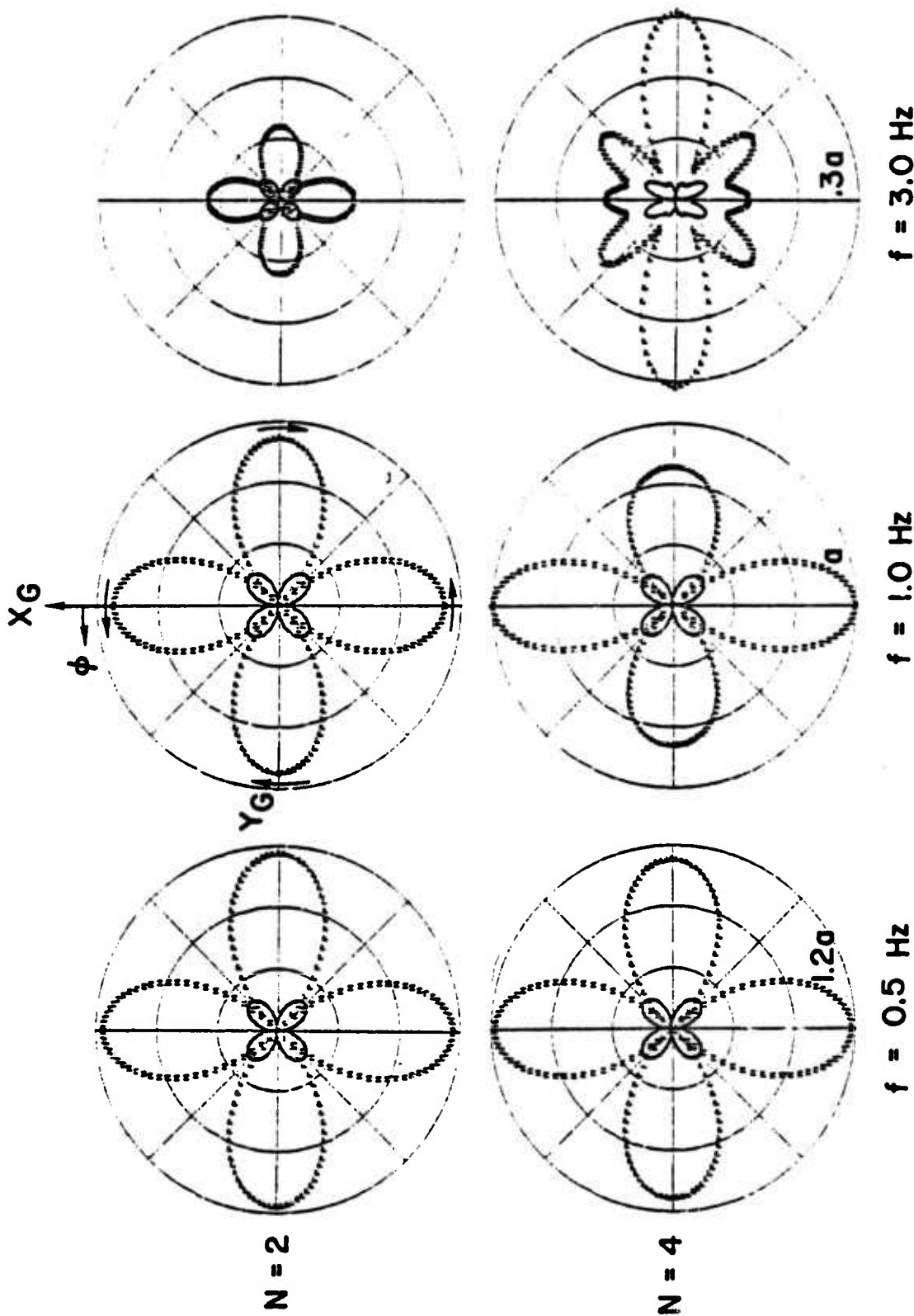


Figure 3.11. Far-field radiation patterns for the bilateral fault (TES) constructed from the tangentially expanding sphere model. These patterns are for $\theta = 90^\circ$ and are directly comparable to those in Figure 3.9 for the finite difference source. Again, $a = 9/R$ cm/km.

understand our results, isolate the origin of the observed effects, etc. Therefore, we might be interested in perturbing the Archambeau/Minster model to get an equivalent source that is even closer to the FD. The third geometry listed above, the growing and propagating sphere model, allows considerable freedom to adjust the radiated wave field as required, though this will not be pursued further here.

To summarize the results of this comparison between analytical and finite difference sources, the first point is that when the fault lengths are the same, the two sources are nearly identical at long periods. This agreement in seismic moment is a remarkable result to which we will return. Agreement at high frequencies is less impressive, but much can be learned from detailed comparison of the two equivalent sources. Finally, if we are willing to adjust the model parameters rather arbitrarily, an analytical model can be found that will have nearly the same equivalent source as that for the finite difference earthquake.

3.6 COMPARISON WITH DISLOCATION MODELS

For the relaxation source model of the previous section we had to select a set of model parameters that seemed appropriate, compute the radiation field and then see how it compared with our source. With dislocation models we take a different approach. From the radiation field we find the "equivalent dislocation model" that best represents the finite difference earthquake. The parameters characterizing this equivalent model will then be compared to the actual parameters in the finite difference calculation.

For the dislocation model geometry we select the often used model of Haskell (1964) as generalized to bilateral faulting by Savage (1972). If we consider the fault

geometry to be as in Figure 3.7, a uniform slip is assumed to propagate a distance L_0 in the $+X_G$ direction and L_π in the $-X_G$ direction on a rectangular fault of length $L_0 + L_\pi$ and width w . Then the amplitude of the Fourier transformed far-field displacement is

$$|\hat{\tilde{u}}^C(\underline{R}, \omega)| = M_0 \tilde{R}^C(\underline{R}) \omega |\hat{G}(\omega)| |F_2^C(\omega, \tau_0, \tau_\pi)|, \quad (3.11)$$

where c is α or β corresponding to P or S waves. The \tilde{R} has as components the spherical coordinates used previously. Also,

$$M_0 = \mu w (L_0 + L_\pi) D_0, \quad (3.12)$$

where D_0 is the final fault offset and

$$\tilde{R}^\alpha(\underline{R}) = \underline{e}_r \sin^2\theta \sin 2\phi / (4\pi\rho\alpha^3 R), \quad (3.13)$$

$$\tilde{R}^\beta(\underline{R}) = [\underline{e}_\theta \sin\theta \cos\theta \sin 2\phi + \underline{e}_\phi \sin\theta \cos 2\phi] / (4\pi\rho\beta^3 R),$$

where $\underline{e}_r, \underline{e}_\theta, \underline{e}_\phi$ are unit vectors in the R, θ, ϕ directions and ρ is density. The $\hat{G}(\omega)$ represents the Fourier transformed rupture time history and F_2 is a factor that includes the modulation of the radiated waves by rupture velocity effects. The F_2 is given by Savage (1972, equation 10) with the exception that his $\cos\theta$ should be replaced by $\sin\theta \cos\phi$.

An equivalent dislocation model for the finite difference earthquake source (FD) should have the same moment (M_0) and a time history of faulting ($G(t)$) that gives the same spectral shape. Let us look first at the moment. We previously pointed out that at low frequencies the FD can be represented by a double-couple. In fact, for ω small (or for a pure double-couple source) the P and SV displacements are

$$\bar{u}_R(R, \theta, \phi, \omega) = \frac{1}{k_\alpha^2} \frac{e}{R} e^{-ik_\alpha R} B_{22}^{(4)}(\omega) P_2^2(\cos\theta) \sin 2\phi, \quad (3.14)$$

$$\bar{u}_\theta(R, \theta, \phi, \omega) = \frac{2}{k_\beta^2} \frac{e}{R} e^{-ik_\beta R} \left[-A_{21}^{(1)}(\omega) + B_{21}^{(2)}(\omega) \right] P_2^1(\cos\theta) \sin\phi \cos\phi.$$

Note that for a pure double-couple source $A_{21}^{(1)} = -B_{21}^{(2)}$.

For the dislocation model Savage (1972) points out that F_2 approaches unity at low frequencies. Then equating (3.11) and (3.14), for small frequencies we find that

$$M_0 i\omega \hat{G}(\omega) = 12\pi\rho\alpha^5 \frac{B_{22}^{(4)}(\omega)}{\omega^2}, \quad (3.15)$$

$$M_0 i\omega \hat{G}(\omega) = 12\pi\rho\beta^5 \frac{\left[-A_{21}^{(1)}(\omega) + B_{21}^{(2)}(\omega) \right]}{\omega^2}.$$

The moment is then obtained from the limit as $\omega \rightarrow 0$. Since $G(\omega) \rightarrow \omega^{-1}$ and $A_{2m}^{(\alpha)}, B_{2m}^{(\alpha)} \rightarrow \omega^{-2}$ (see Figure 3.6) in the low frequency limit, we can compute the moment from (3.15).

From the P waves we find

$$M_0 = 1.62 \times 10^{23} \text{ dyne-cm}, \quad (3.16a)$$

and from the S waves

$$M_0 = 1.51 \times 10^{23} \text{ dyne-cm}. \quad (3.16b)$$

We now turn our attention to the spectral shape. For convenience we normalize the amplitude spectra by dividing by the moment (M_0) and the double-couple radiation pattern (\tilde{R}^C). The normalized far-field spectra for the dislocation model are then

$$A^C(\omega) = \omega |\hat{G}(\omega)| |F_2^C(\omega, \tau_0, \tau_\pi)|, \quad (3.17)$$

and a similar form may be written for the multipole source representation. Note that (3.17) is still radiation pattern dependent via F_2^C which plays a role similar to that of the higher order terms ($l \geq 4$) in the multipolar expansion.

Two forms will be considered for the rupture time history. First, a form suggested by Haskell (1964)

$$G_H(t) = 0, \quad t \leq 0, \quad (3.18)$$

$$G_H(t) = 1 - e^{-t/T}, \quad t > 0.$$

The second is a slightly more complex form suggested by Ohnaka (1973)

$$G_O(t) = 0, \quad t \leq 0, \quad (3.19)$$

$$G_O(t) = 1 - (1-t/T)e^{-t/T}, \quad t > 0.$$

If the rise time is defined as the time to reach 0.9, we have $t_R = 2.3T$ for the Haskell form and $t_R = 3.9T$ for the Ohnaka form. The Fourier transformed amplitudes are

$$|\hat{G}_H(\omega)| = \omega^{-1} (1 + \omega^2 T^2)^{-1/2}, \quad (3.20)$$

$$|\hat{G}_O(\omega)| = \omega^{-1} (1 + \omega^2 T^2)^{-1}.$$

If we select the elastic velocities (α, β), rupture velocity (V_R) and fault length ($L_0 = L_\pi = 0.5$) to be the same as in the finite difference calculation, the only free parameter for matching spectral shapes is T . For each of the time histories of (3.20) a T was selected to bring the corner frequencies into agreement, using the half-amplitude

rule. For any given T the agreement is better in some portions of the radiation pattern than in others, so a value that "optimized" the agreement over the pattern was chosen. It was previously mentioned that the ratio of P to S wave corner frequencies is >1 for our finite difference model but is <1 for dislocation models of this type. To account for this difference a different T was selected for the P wave spectra. The selected "best" values for the equivalent dislocation are as follows: For the S wave and $G_H(t)$ we have $T = 0.19$, $t_R = 0.44$ and for $G_O(t)$, $T = 0.11$, $t_R = 0.43$. For the P wave and $G_H(t)$ we have $T = 0.17$, $t_R = 0.39$ and for $G_O(t)$, $T = 0.10$, $t_R = 0.39$. All values are in seconds. We see that in terms of rise time the two dislocation time histories give the same result. The T values are considered to be ± 0.01 for a reasonable fit to the corner frequencies. An illustration of the resulting fit is shown in Figure 3.12 for S waves at one location on the radiation pattern.

Having specified the moment and rupture time history, we have an equivalent dislocation model. Let us now compare the parameters of this model with the actual faulting in the finite difference code. First consider the rise time. The shape of the rupture time histories shown in Figure 3.3 are compatible with the dislocation model forms of (3.18) or (3.19). However, the rise times are certainly no longer than 0.10 seconds which is a factor of four less than those for the equivalent dislocation model. Can this discrepancy be attributed to the propagation from the fault surface to the elastic radius? The displacement time histories at the elastic radius in Figure 3.5 show a rise time of only ≈ 0.30 seconds even though the interference between the P and S waves seems to be nearly doubling the rise time. Another interesting observation is that the rupture time ($0.5/V_R$) is ≈ 0.19 seconds, a value that seems consistent with the

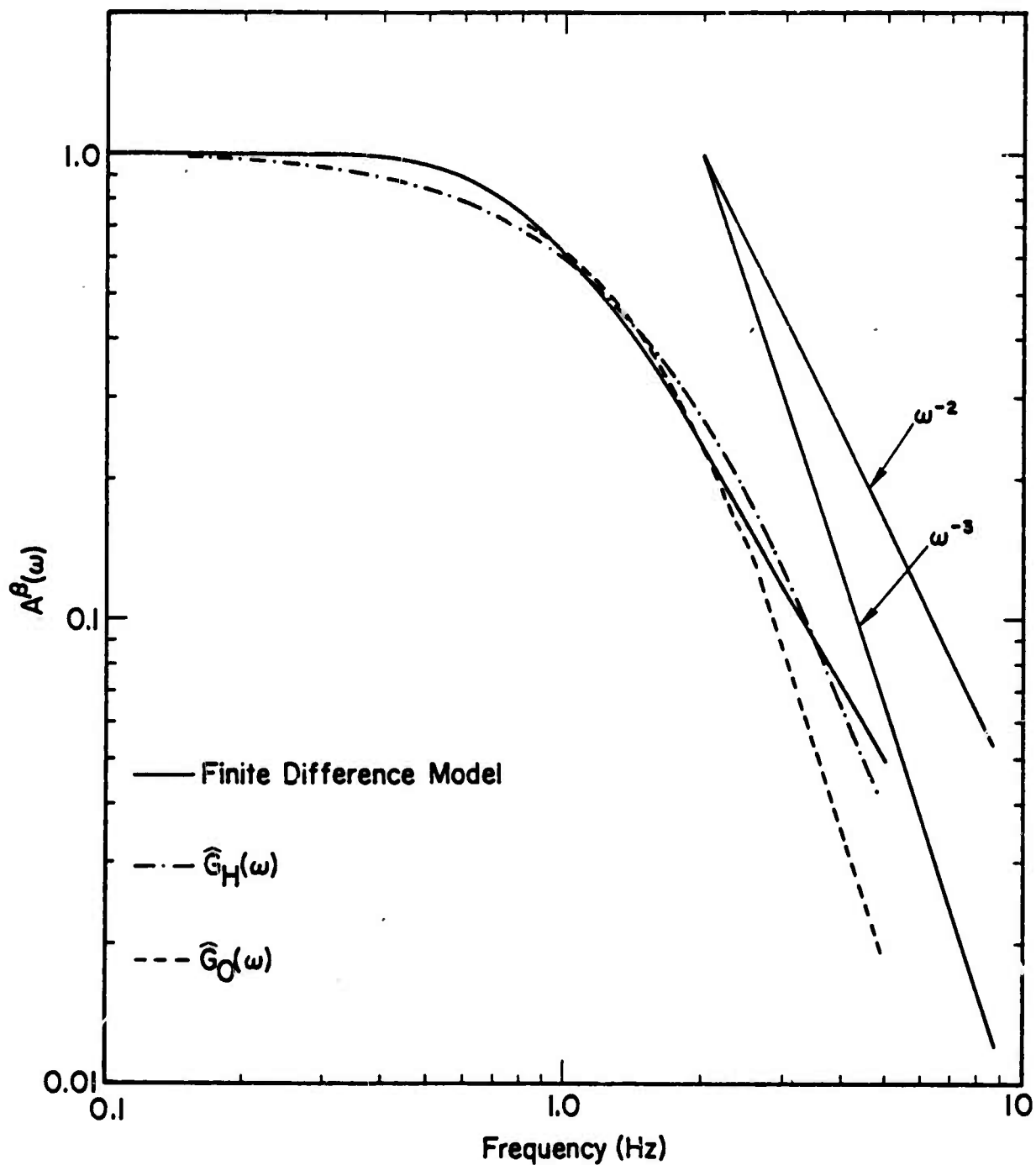


Figure 3.12. Comparison of the far-field SH spectrum at $\tau = 30^\circ$, $\phi = 30^\circ$, for the finite difference earthquake source to spectra from a dislocation model with two rupture time histories (3.18, 3.19). The spectra are normalized by the moment and the double-couple radiation pattern effect. For the dislocation time histories T has been selected to bring the corner frequencies into agreement, using the half amplitude rule.

rise time in Figure 3.5. In short, we are forced to conclude that the rise time for our equivalent dislocation model is a factor of 2-4 larger than the rise times associated with the actual rupture process. Perhaps more complex dislocation model geometries and rupture time histories would reduce the discrepancy but removing it entirely would appear to be a formidable task.

What about the seismic moment? We obtained two estimates in (3.16), one from the P waves and one from the S waves. The dependence of moment on the source parameters is given by (3.12). If we take the fault area to be $0.6 \times 1.0 \text{ km}^2$ and the elastic shear modulus to be $\mu = 324 \text{ kbar}$, we can find the average dislocation, D_0 , for the equivalent dislocation model. The values are 83.6 and 77.5 cm for the P and S wave moments or an average equivalent D_0 of $\approx 80 \text{ cm}$. The actual displacement at five positions on the fault surface was shown in Figure 3.3. Multiplying by two to obtain the dislocation, these values are 22-30 cm. In fact, the average dislocation over the whole fault surface is 26 cm as is shown in the left plot in Figure 3.13. The actual dislocation is then smaller than the equivalent dislocation by a factor of three.

To what can we attribute the dislocation discrepancy? We can hardly suppose that the effective rigidity in the fault zone was much larger than the elastic value. If anything, the plasticity would tend to have the opposite effect. Another possibility is that the equivalent dislocation model sees a different fault area than that on which slip occurs. A nearly maximum effect is obtained by considering the effective fault surface to be the $2.0 \times 1.6 \text{ km}^2$ plane one zone or 0.1 km from the actual fault surface. With this fault area the effective dislocation is $\approx 15 \text{ cm}$. The actual dislocation on this plane in the finite difference grid is shown in the right of Figure 3.13. The average value

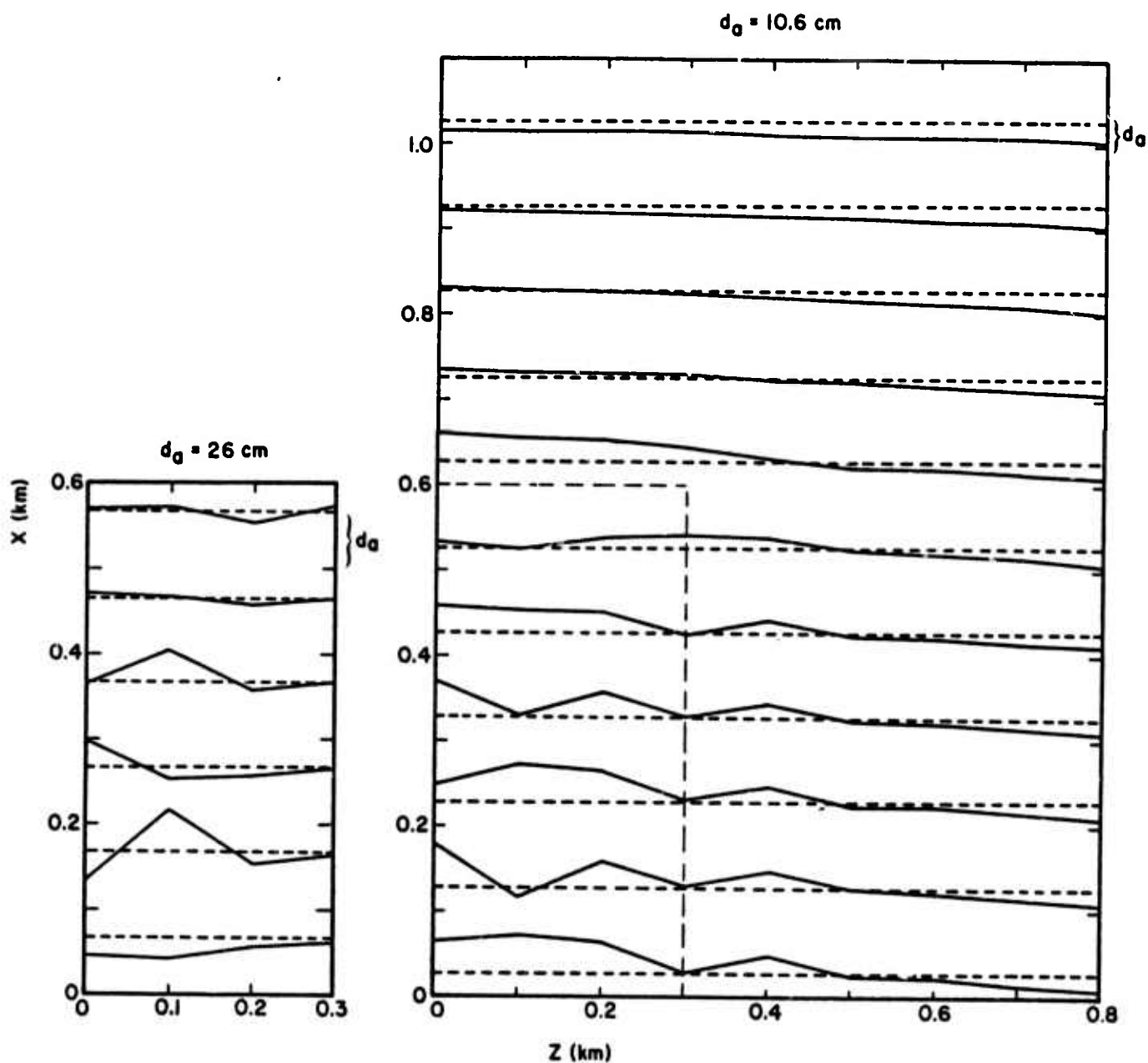


Figure 3.13. The static dislocation on the fault surface (left) and one zone (0.1 km) from the fault surface. The average dislocation (d_a) over the plane is indicated by a dotted line on each plot. The data points are the values at the nodes in the grid. The nodes are indicated by their distance from the $X = 0$ or $Z = 0$ line.

is 10.6 cm and the discrepancy has been reduced to a more satisfactory factor of 1.4. Some further improvement could probably be made by taking an optimum portion of this plane. However, we must address the question: When we construct an equivalent dislocation model for an earthquake, what do we mean, in terms of the physics, by the fault surface and average dislocation?

The product of area times average static displacement for the two planes in Figure 3.13 is greater for the plane away from the fault surface. This kind of radiation of displacements from the fault surface is unlike that in a dislocation model and seems to be due to the plastic adjustment of the stress concentrations that arise near the rupture front. More calculations must be done to be sure we understand the effect of finite difference zone size, details of the material behavior at high stress, etc., but our model of the decay of displacements from the fault surface seems more likely to correspond to physical reality than that in the dislocation model.

3.7 CONCLUSIONS

Our purpose in undertaking this work was twofold. First, we wanted to carry out a three-dimensional simulation of earthquake faulting and to link the finite difference code with elastic wave theory; in other words, to explore the feasibility of the technique. Second, we wanted to see what could be learned about earthquake source theory from the results of our first calculation. Our concluding remarks are directed, in turn, to these two purposes.

The event selected for study was a small bilateral earthquake with a symmetrically propagating, constant velocity rupture. A simple mechanism for relieving the stress concentrations at the crack tip was introduced by

considering the material in the fault zone to behave in an elastic-plastic manner. What seems to be a realistic simulation of stick-slip fault rupture was the result. This numerical simulation is perhaps one of the simplest that can be done. The point is that now much more complex geometries and material behaviors can be introduced and their effects determined.

For propagating the earthquake generated waves very far from the fault, much efficiency is gained by representing the event by an equivalent elastic source. A generally applicable technique for obtaining such a source from finite difference output was developed during the course of this research. The equivalent elastic source representation of finite difference source calculations also has great value in allowing convenient comparison of the source characteristics with those obtained from other theories.

We have presented the results of a single calculation; there are no others. With due caution against pushing the results too far, we find a number of intriguing results when comparing the far-field displacement spectra from our finite difference source to that from the elastodynamic model of Archambeau/Minster (Archambeau, 1968; Minster, 1973) and to that from dislocation models (Haskell, 1964; Savage, 1972). In almost all respects the radiation from our source more closely resembles that from the Archambeau/Minster volume source, relaxation model. The long period level or moment is essentially identical. At frequencies up to the corner frequency the radiation patterns are also nearly the same. While the corner frequencies themselves and the shape of the spectra in this region do differ for the analytical and finite difference sources, it is interesting to note that the ratio of P to S corner frequencies is almost the same over the whole radiation pattern and is

greater than one everywhere. In short, the elastodynamic relaxation source, using the same model parameters as in our finite difference source, is quite similar as a radiator of far-field seismic waves.

Using the dislocation theory of Haskell (1964) extended to bilateral faulting by Savage (1972), we constructed an equivalent dislocation model from the far-field radiation computed for our finite difference source. Optimizing the agreement between corner frequencies, we found that the rise time for the dislocation model time history was a factor of 2-4 greater than the actual rise time for the displacement time histories on the fault surface. Examination of the time histories from which the equivalent elastic source was obtained indicated that this was not due to finite grid attenuation or dispersion effects. Using the actual fault surface and elastic shear modulus, the average fault offset for the equivalent dislocation model was more than a factor of 3 greater than the fault offset in the finite difference calculation.

In terms of a kinematic description of the displacements at the fault surface, our finite difference earthquake looks quite similar to a dislocation model. Nevertheless, we found rather poor agreement between the actual fault parameters and those of the equivalent dislocation model when we consider the absence of errors due to propagation and sampling effects.

Why does the finite difference source look more like a volume source model? It is tempting to think that it is because the entire "fault zone" is yielding in the same way as the spherical volume in the Archambeau/Minster source. But this seems to be not the case. Both P and S waves are radiated directly from the fault surface (Figure 3.5). The plastic work (stress time plastic strain) in the fault zone

is large in the vicinity of the crack tip during rupture. But in most of the fault zone the amount of plastic flow is quite small. We saw in Figure 3.13 that the plastic readjustment of the stress concentrations near the rupture front cause the displacements one zone from the fault surface to be quite different than they would be in an elastodynamic dislocation model. This seems to be the cause of the disagreement between equivalent dislocation and actual model parameters. However, it is not entirely clear why the volume source model agrees so well. Nor do we know whether this agreement is particular to this finite difference earthquake or would be obtained for a whole class of finite difference earthquake simulations. Answers to these questions will emerge from the study of future calculations.

IV. SHORT PERIOD THEORETICAL SEISMOGRAMS FOR A PROPAGATING SOURCE MODEL FOR EARTHQUAKES

4.1 INTRODUCTION

Much of the available evidence for the character of the earthquake source mechanism is contained in recordings of ground motion at great distances from the source. The same can be said for underground nuclear explosions. The far-field seismic recordings are often quite complex with the causes lying in two categories: (1) Complexity of the source, and (2) Modulation of the source generated ground motion by the earth structure intervening between source and receiver. For nearly all seismological studies we want to be able to remove one of these causes of complexity in order to understand the other.

In a previous paper, Bache and Harkrider (1976, subsequently referred to as paper I) set forth a method by which high resolution methods for simulating the complex seismic source can be linked with high resolution elastic wave propagation techniques. The particular application addressed in that paper was to the body waves propagating to the far-field. For surface waves a similar formulation was given by Harkrider and Archambeau (1976).

In this paper the objective is to use the theoretical results given in paper I to compute synthetic seismograms for an earthquake source model that is sufficiently complex to illustrate the potential utility of this theory for seismological research. The earthquake source model chosen is that of Archambeau (1968) and Minster (1973). Most prominent among the "higher order" effects included in the version of the model used here are those due to fault propagation at finite rupture velocity and these can have important effects on the teleseismic short period ground motion recordings.

We begin by describing the rapid and inexpensive techniques being used for computing synthetic seismograms. These techniques include the interfacing of the paper I formulation for the steeply emergent body waves at the base of the crustal model at the source with generalized ray theory (e.g., Wiggins and Helmberger, 1974) for the upper mantle travel path.

The Archambeau/Minster source model is briefly discussed, particularly the scaling with the source parameters. Our intention in this section is primarily to demonstrate the kinds of effects that can now be conveniently included in theoretical seismograms rather than to present a detailed study of these effects. Therefore, only a single source at one orientation (strike-slip) is used for the theoretical seismogram calculations. For this source the dependence of teleseismic body wave recordings on focal depth and fault azimuth is discussed.

4.2 COMPUTATION OF THEORETICAL SEISMOGRAMS

The Fourier transformed equations of motion in a homogeneous, isotropic elastic medium may be written

$$\bar{\mathbf{u}} = - \left(\frac{1}{k_\alpha^2} \right) \nabla \bar{\chi}^{(4)} + \left(\frac{2}{k_\beta^2} \right) \nabla \times \bar{\mathbf{\chi}} , \quad (4.1)$$

where $\bar{\mathbf{u}}$ is particle displacement and k_α and k_β are the compressional and shear wave numbers. The Cartesian potentials $\bar{\chi}^{(4)}$ and $\bar{\mathbf{\chi}}$ can be written in terms of the following expansion in spherical harmonics;

$$\begin{aligned} \bar{\chi}^{(j)}(\underline{\mathbf{R}}, \omega) = & \sum_{\ell=0}^{\infty} h_\ell^{(2)}(k_j R) \sum_{m=0}^{\ell} \left[A_{\ell m}^{(j)}(\omega) \cos m\phi \right. \\ & \left. + B_{\ell m}^{(j)}(\omega) \sin m\phi \right] P_\ell^m(\cos\theta), \quad j = 1, 2, 3, 4, \quad (4.2) \end{aligned}$$

where the $h_{\ell}^{(2)}$ are spherical Hankel functions of the second kind and the P_{ℓ}^m are associated Legendre functions. The vector \tilde{R} has as components the spherical coordinates R, θ, ϕ

As was pointed out in paper I, nearly any proposed seismic source model can be specified in terms of the expansion (multipole) coefficients of (4.2). Therefore, (4.2) together with (4.1) provide an elastic point source representation of the (outgoing) displacement field. For a source prescribed in this form and buried at a depth h in a plane-layered, semi-infinite elastic medium, paper I includes the derivation of the expressions for the steeply emergent body waves emanating into the underlying halfspace at a specified angle θ_n or, equivalently, horizontal phase velocity c . The geometry is shown in Figure 4.1. Polarized into P, SV and SH components, these displacements are (Eq. (33), paper I)

$$\begin{aligned}\bar{U}_P &= \sum_{m=0}^{\ell} \left(-\frac{1}{k_{\alpha_n}} \right) i^m r_{\alpha_n} \hat{\Delta}_n^{(m)} \frac{e^{-ik_{\alpha_n} R}}{R}, \\ \bar{U}_{SV} &= \sum_{m=0}^{\ell} \left(\frac{2}{k_{\beta_n}} \right) i^{m-1} r_{\beta_n} \hat{\omega}_n^{(m)} \frac{e^{-ik_{\beta_n} R}}{R}, \\ \bar{U}_{SH} &= \sum_{m=0}^{\ell} i^m r_{\beta_n} \hat{\varepsilon}_n^{(m)} \frac{e^{-ik_{\beta_n} R}}{R},\end{aligned}\tag{4.3}$$

where all notation is defined in paper I.

To compute theoretical seismograms we take the plane layered model of Figure 4.1 to represent the crust in the source vicinity. Then (4.3) gives the waves propagating into the upper mantle. Other methods are then used to

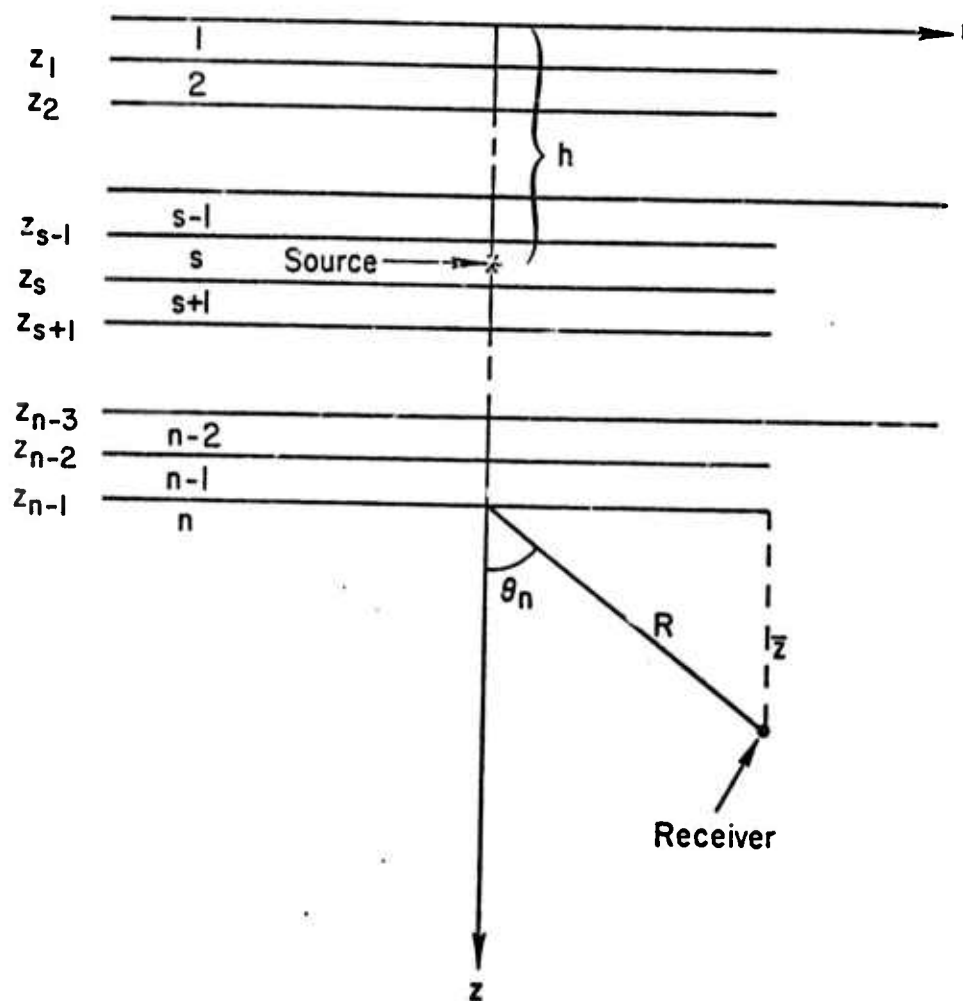


Figure 4.1. The geometry and coordinate system for a source at depth h in a multilayered halfspace.

compute the remainder of the travel path. While there are alternatives, we have found it convenient to use generalized ray theory (Wiggins and Helmberger, 1974) for the upper mantle and Haskell-Thomson matrices (Haskell, 1960, 1962) for the crust in the receiver vicinity. Thus, the travel path is divided into three pieces:

1. The crust at the source to a depth D .
2. The crust at the receiver to the same depth D .
3. A laterally homogeneous upper mantle extending from D to the deepest depth of interest.

The travel path segments are linked by requiring that the velocities at D be the same in all three structures. This scheme gives a great deal of computational flexibility in that portions of the travel path can be varied without repeating the entire calculation. The actual implementation is as follows:

1. A generalized ray theory calculation is done to determine the impulse response at epicentral distances of interest. The source and receiver are at the surface of an earth model in which the top D kilometers have been removed. A ray parameter or horizontal phase velocity (c) is associated with each major arrival at the receiver and this is an input parameter for the crustal response calculations. In practice the crustal response variation with c is sufficiently small that for most distances, certainly all those beyond the triplications, a single c is sufficient.
2. The displacements exiting the source region at phase velocity c are computed using (4.3).
3. A frequency dependent transfer function is computed for the plane layered model of the crust

beneath the receiver. The appropriate transfer functions were given by Haskell (1960, 1962). For example, for P waves the transfer function is

$$T_V(\omega) = 2c \frac{(J_{41}^R - J_{31}^R)}{\alpha_n D_J} ,$$

for the vertical component of motion at the surface and

$$T_R(\omega) = 2c \frac{(J_{42}^R - J_{32}^R)}{\alpha_n D_J} ,$$

for the radial component (all notations are as in paper I). Here

$$D_J = (J_{11}^R - J_{21}^R)(J_{32}^R - J_{42}^R) - (J_{12}^R - J_{22}^R)(J_{31}^R - J_{41}^R) .$$

4. Anelastic attenuation and the attendant dispersion are included via the operator

$$\exp \left\{ -\pi f \frac{T}{Q} \left[1 - \frac{2}{\pi} i \ln \left(\frac{1000}{f} \right) \right] \right\} ,$$

using the formulation suggested by Strick (1970). Here f is frequency and the controlling parameter is T/Q , the ratio of travel time to the average path material quality factor. The T/Q is conveniently input as a constant prescribed for each seismogram calculation. However, it can easily be computed from a postulated Q versus depth model for each ray path. Also, Hasegawa (1971) has pointed out that only minor modifications are required to include the effect of Q in Haskell-Thomson matrix calculations.

5. The sensing instrument is characterized by a frequency dependent transfer function.

The source, source crust, receiver crust, Q and instrument effects are computed in the frequency domain. Numerical Fourier transformation brings their combined effect to the time domain where it is convolved with the upper mantle response to complete the theoretical seismogram calculation.

In later sections we will present theoretical seismograms computed with this method. However, we first describe the source model and its radiation field.

4.3 THE ARCHAMBEAU/MINSTER EARTHQUAKE SOURCE MODEL

Archambeau (1968) and Minster (1973) have developed a relaxation source theory for earthquakes in which the finite rupture velocity causes significant excitation of higher order ($l > 2$) terms in the multipolar expansion (4.2) of the radiation field, particularly at frequencies beyond the corner frequency. These higher order terms have an interesting effect on the body waves propagated to teleseismic distances.

The main features of the elastic radiation field from this earthquake source model are discussed by Minster and Archambeau (1976). For our calculations we shall use the model they call the "tangentially expanding sphere". In this model a spherical volume of vanishing rigidity expands from zero to its final diameter with a point on the diameter fixed in space. This expanding weak zone is assumed to be in a homogeneous elastic medium that is stressed in pure shear. The parameters of the earthquake model are then:

- L - The fault length; equal to the final diameter of the expanding sphere.

- V_R - The rupture velocity; controls the rate of increase of the sphere.
- α, β - The P and S elastic wave velocities.
- $s^{(0)}$ - The prestrain; equal to $\sigma^{(0)}/\mu$, the ratio of prestress to material rigidity. The radiation field scales directly with $s^{(0)}$.
- R_S - The radius of the zone in which the tectonic prestress is released.

Archambeau's assumption of a finite R_S , which is an approximation meant to represent a nonuniform prestress field, has led to considerable controversy (e.g., Molnar, et al., 1973) since the resulting source spectrum is peaked. While the assumed value of R_S has great importance for long period studies or very large faults, its value has almost no effect on short period body waves for moderate fault dimensions. Here we shall simply take R_S to be infinite.

While the scaling of the radiated field with these parameters is discussed in detail in Minster and Archambeau (1976), we should point out several features that will be of importance here. For a particular fault orientation, the multipole coefficients are completely specified by Poisson's ratio (ν), prestrain and the ratios L/V_R and V_R/β (assuming $R_S \rightarrow \infty$). The amplitude of the coefficients is fixed by L/β (or L/α since ν is fixed) while the corner frequency depends on L/V_R . The character of the radiated field also depends on the orientation of the prestrain and rupture direction with respect to the free surface. These can conveniently be specified by strike, dip and plunge angles.

The amplitude dependence on L/β is identical to the behavior of elementary dislocation theories. For example,

given in paper I are the multipole coefficients for a horizontal double-couple (normal strike-slip fault) dislocation source. A typical term is

$$A_{21}^{(1)}(\omega) = - \frac{i \bar{D}(\omega) k_\beta^3 A_f}{24\pi}, \quad (4.4)$$

where $\bar{D}(\omega)$ is the dislocation per unit area and A_f is the fault area. If the fault dimension is $\approx L$ and the strain drop is approximately \bar{D}/L , (4.4) shows that

$$A_{21}^{(1)}(\omega) \approx S^{(0)} \frac{L^3}{\beta^3}, \quad (4.5)$$

which is the same amplitude scaling that occurs in the Archambeau/Minster model.

We shall compute theoretical seismograms for a particular earthquake specified by the following source parameters:

$$\begin{aligned} L &= 10 \text{ km}, & V_R &= 4.14 \text{ km/sec}, \\ \alpha &= 7.9 \text{ km/sec}, & \beta &= 4.6 \text{ km/sec}, \\ S^{(0)} &= 10^{-3}, & R_S &\rightarrow \infty. \end{aligned} \quad (4.6)$$

The fault orientation is assumed to be right-lateral strike-slip along the geographic X_G -axis, assumed to point north. The geographic coordinate system and fault geometry are shown in Figure 4.2. Also shown are the azimuth and takeoff angle (ϕ, τ) for specifying a ray (A). In terms of the coordinates of (4.2) and Figure 4.1, τ may be identified with θ_S measured from the downward vertical in the source layer. Then $\tau \equiv \theta_S = \pi - \theta$ where θ is the spherical coordinate in (4.2).

In deriving the steeply emergent body waves given by (4.3), only the far-field terms (decaying as R^{-1}) were retained. In the far-field the dependence of the expansion (4.2) on R is separable since the Hankel functions reduce

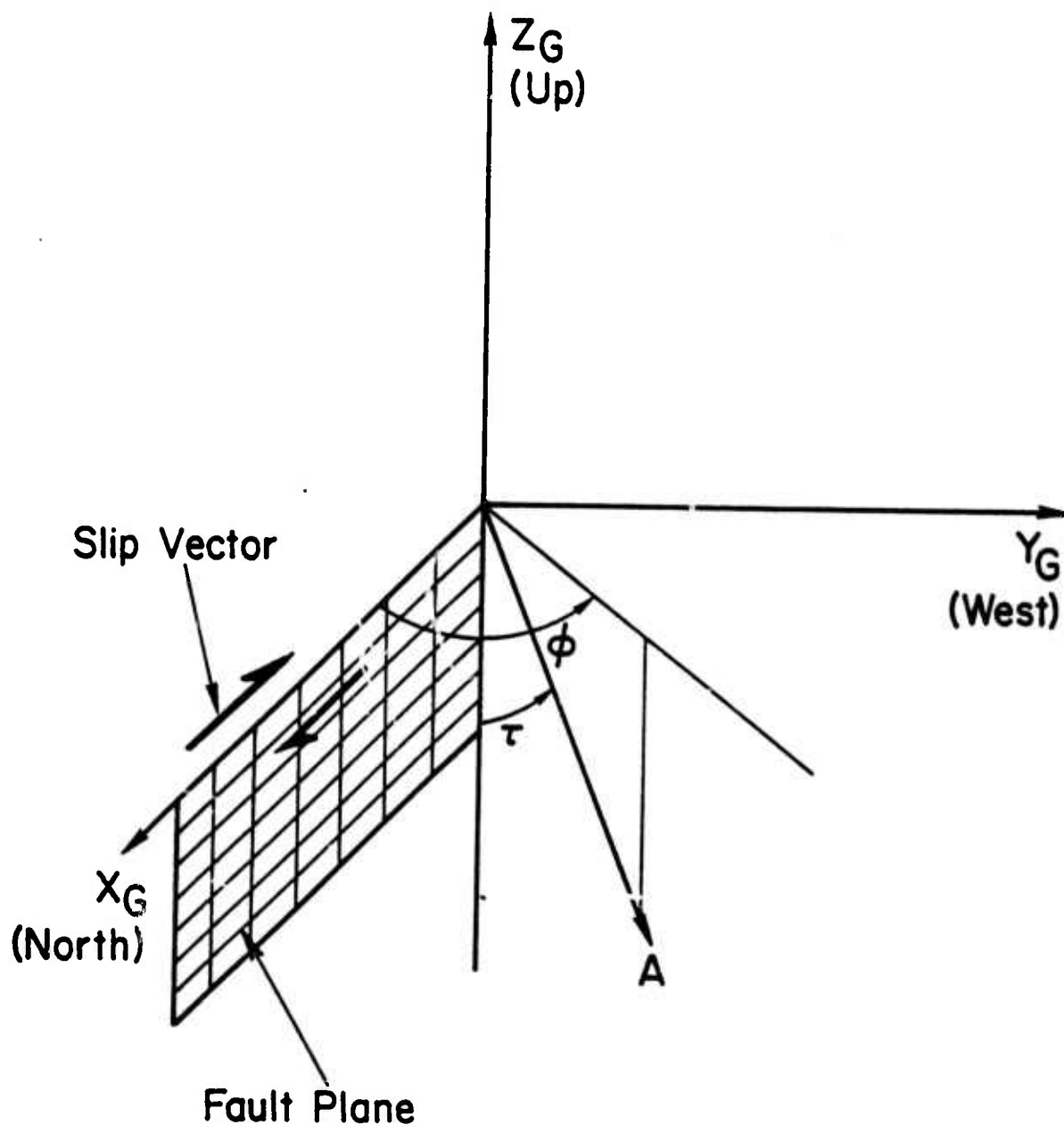


Figure 4.2. The geometry and coordinate system for a right-lateral strike-slip fault. The outgoing displacement field along the ray A is specified by the azimuth ϕ and takeoff angle τ .

to

$$h_{\ell}^{(2)}(k_j R) = i^{\ell+1} \frac{-ik_j R}{k_j R}, \quad j = \alpha \text{ or } \beta. \quad (4.7)$$

Further, the P and S waves separate with the P waves given by the first term on the right side of (4.1) and the S waves given by the second term.

In view of the similarity properties of the model, the multipole coefficients for the earthquake specified by (4.6) are identical to those for an event with fault parameters:

$$\begin{aligned} L &= 7.6 \text{ km}, & V_R &= 3.14 \text{ km/sec}, \\ \alpha &= 6.0 \text{ km/sec}, & \beta &= 3.49 \text{ km/sec}, \\ S^{(0)} &= 10^{-3}, & R_S &\rightarrow \infty. \end{aligned} \quad (4.8)$$

While the multipole coefficients are identical, the stress drop ($\mu S^{(0)}$) differs depending on the shear moduli. From (4.1), it is clear that the far-field P and S wave displacements are proportional to α^2 and β^2 , respectively.

Before presenting theoretical seismograms for the strike-slip earthquake source (4.6) or (4.8), it is useful to develop some insight into the behavior of the source as a radiator of elastic waves in a whole space. Far-field displacement radiation patterns are presented in Figures 4.3 and 4.4. These are computed from (4.1) and (4.2), retaining only far-field terms, using the source described by (4.6). The patterns are equally valid for the source (4.8) with the amplitudes being scaled by the square of the velocity ratios or $(6.0/7.9)^2$.

In Figure 4.3 the far-field displacement radiation patterns are shown for a number of frequencies and several levels of truncation for the infinite series (4.2). These

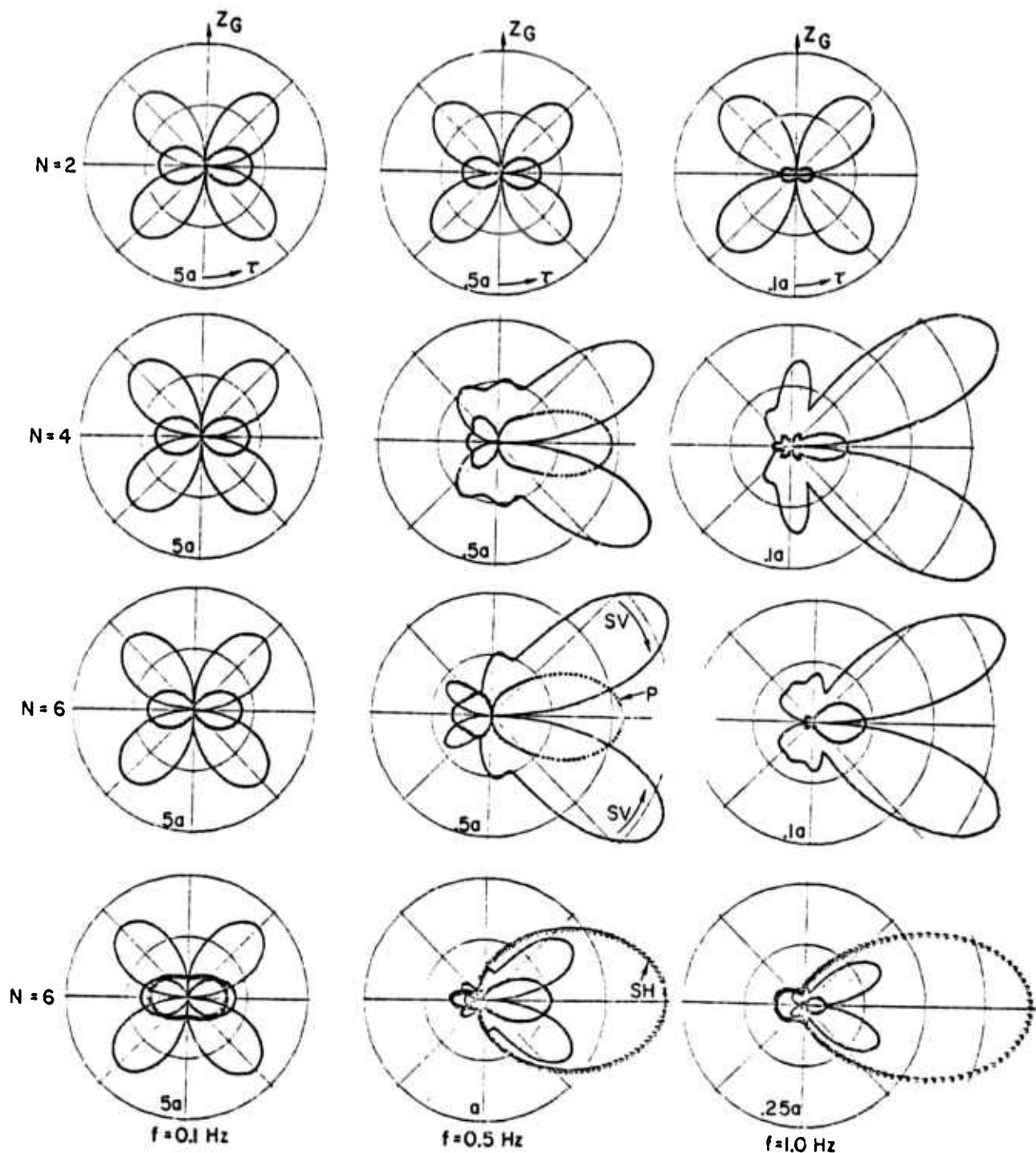


Figure 4.3. Far-field displacement radiation patterns at three frequencies (plotted vertically) and three levels of truncation of the multipolar coefficients. The patterns are for fixed azimuth $\phi = 45^\circ$ and are oriented with respect to the system of Figure 4.2 as indicated in the double-couple patterns of the first row. The SH component is suppressed on the $N = 4$ and first set of $N = 6$ plots. (The meaning of the plot symbols is indicated on the last two plots of the center row.) The displacement amplitude at the outer circle is indicated in units of a , $a = 1.98$ cm-sec.

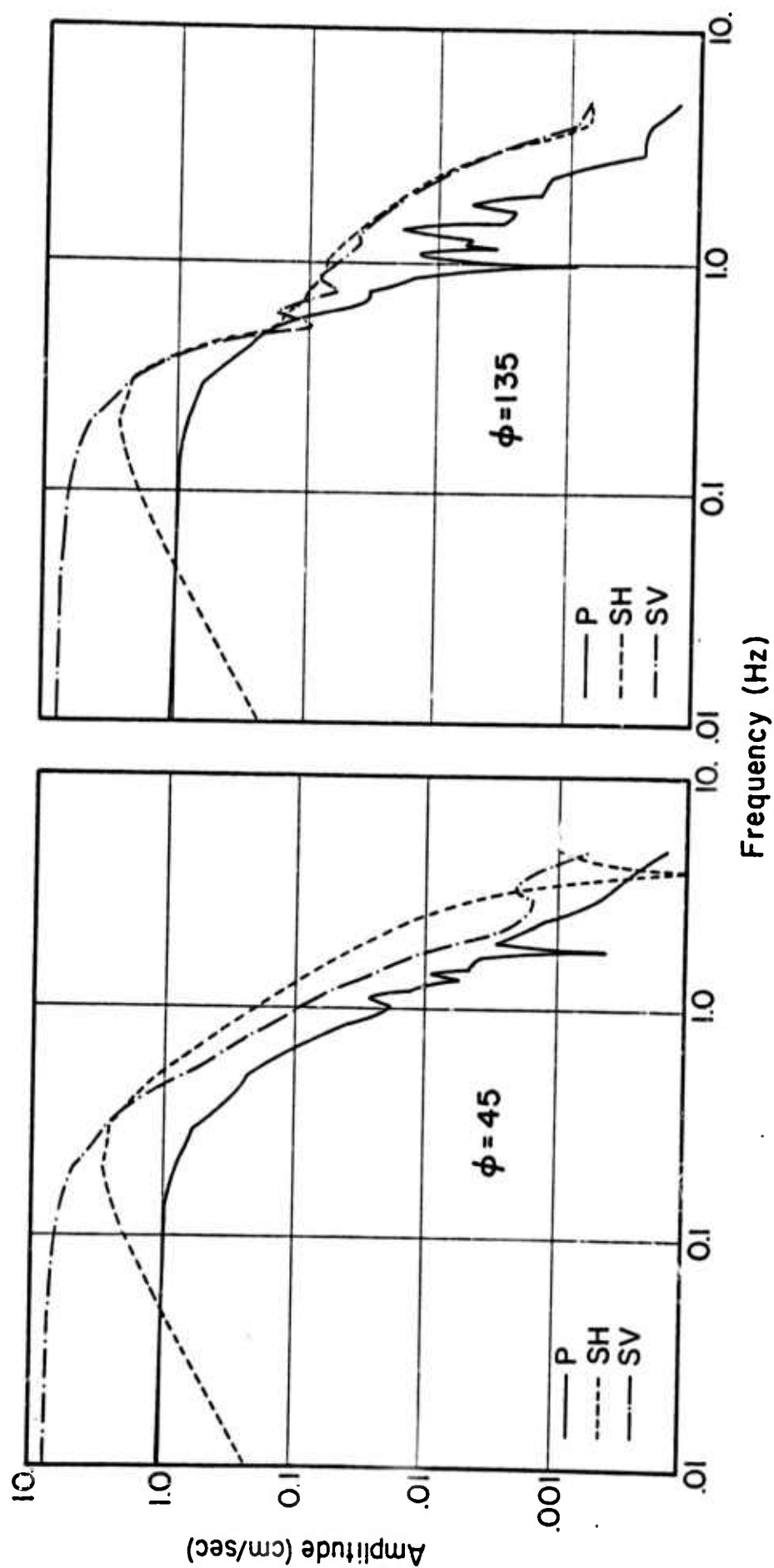


Figure 4.4. Free-field displacement spectra at $R = 100$ km, $\tau = 30^\circ$ for two azimuths.

radiation patterns are for the three components (u_R or P, u_θ or SV and u_ϕ or SH) of the amplitude $|\bar{u}(R, \theta, \phi, \omega)|$ of the displacement spectrum at fixed R, ϕ, ω and varying θ . The azimuth is $\phi = 45^\circ$ and we have chosen the frequencies $f = 0.1, 0.5, 1.0$ Hz. The spectral amplitudes are for $R = 100$ km, though in view of (4.7) they can easily be scaled to any R of interest. Truncating the series (4.2) at $\ell = 2$, the source is a quadrupole or double-couple. We then show the effect of adding the higher order terms as we truncate at $\ell = 4$ and $\ell = 6$. The level of truncation or maximum ℓ is denoted N . For the double-couple ($N = 2$) the $\phi = 45^\circ$ orientation is a node on the SH wave pattern. However, a strong SH component appears upon adding higher order terms. For clarity this component is suppressed on the $N = 4$ patterns and the $N = 6$ patterns are shown with and without the SH waves.

From Figure 4.3 we see that at low frequencies the source is rather well approximated by a double-couple. At higher frequencies the higher order terms have a pronounced effect, skewing the radiation pattern toward the direction of fault propagation. The large SH component is, of course, only present due to the higher order multipoles. The 0.5 and 1.0 Hz patterns are typical of those controlling teleseismic bodywaves. Taking higher order propagation effects into account, these patterns are certainly quite different from those for a pure double-couple.

Further insight into the properties of the source as an elastic wave radiator is provided by the spectra of Figure 4.4. For the three displacement components (P, SV, SH) spectra are shown at a forward ($\phi = 45^\circ$) and backward ($\phi = 135^\circ$) azimuth for the takeoff angle $\tau = 30^\circ$. For these spectra the series truncation is at $N = 6$. The measured (from the high and low frequency asymptotes) P

and S corner frequencies for the $\phi = 45^\circ$ spectra are $f_0(P) \approx 0.3$ Hz and $f_0(S) \approx 0.22$ Hz. We mention in passing that these are in rough agreement with empirically determined values for actual earthquakes with similar source dimensions (e.g., Wyss and Shamey, 1975).

Below the corner frequency, the source is predominantly double-couple. At greater frequencies the higher order terms assume increasing importance and come to dominate, as is apparent in the radiation patterns. In fact, truncating the series after six terms, convergence has not yet been attained for frequencies much beyond 1 Hz. Minster (private communication) has found that the addition of more terms acts to smooth the spectrum, removing the spectral holes. However, the theoretical seismograms to be presented are insensitive to details of the source spectrum beyond 1 Hz and we need not be concerned with the complicated structure in this spectral region.

4.4 THEORETICAL SEISMOGRAMS

We now specify an earth model and compute theoretical teleseismic short period seismograms for the earthquake source described in the previous section. The source crustal model is representative of the Basin and Range Province in the western United States (Hill and Pakiser, 1967) and is tabulated in Table 4.1. The crust at the receiver (tabulated in Table 4.2) is an average continental crust which has almost no effect on the seismogram shape.

The upper mantle model is HWNE (Helmberger and Wiggins, 1971) with the top 50 km removed for compatibility with our computational scheme. The generalized ray theory calculation was done for a range of 4000 km. For the total epicentral distance it is necessary to add corrections for the travel in the crust at the two ends. At this distance

Table 4.1. Basin and Range Crustal Structure

<u>Depth</u> <u>(km)</u>	<u>α</u> <u>(km/sec)</u>	<u>β</u> <u>(km/sec)</u>	<u>ρ</u> <u>(gm/cm³)</u>	<u>μ</u> <u>(kbar)</u>	<u>ν</u>
2.5	4.2	2.6	2.40	162	0.189
18.0	6.0	3.49	2.82	343	0.244
31.0	6.7	3.85	3.00	489	0.254
46.0	7.9	4.6	3.30	698	0.244
50.0	8.0	4.6	3.30	698	0.253

Table 4.2. Average Continental Crust

<u>Depth</u> <u>(km)</u>	<u>α</u> <u>(km/sec)</u>	<u>β</u> <u>(km/sec)</u>	<u>ρ</u> <u>(gm/cm³)</u>
22.0	6.03	3.53	2.8
37.0	6.70	3.80	3.0
50.0	8.00	4.60	3.3

the dominant energy arrives with horizontal phase velocity $c = 12.99$ km/sec, the value used for the crustal structure calculations. With this c the distance correction for the receiver crust is ≈ 30.7 km while the source crust correction is generally smaller, depending on source depth. At 4000 km the upper mantle response is little different from a constant spreading factor with a value of about 0.95×10^{-4} . Finally, the anelastic attenuation operator was applied with $T/Q = 1.05$ and the ground motion was filtered by the response of a standard LRSM short period Benioff seismometer.

Setting up the theoretical calculations this way, only the source itself and its modulation by the local geology varies from one theoretical seismogram to another. That is, all features of the computations are held fixed except the ground motion propagating from the base of the crust at the source which is computed from (4.3). For the earthquake source specified by the source parameters (4.6) or (4.8) and the orientation of Figure 4.2, we are interested in the dependence of teleseismic ground motion on azimuth, focal depth and the proximity of major velocity discontinuities in the crust. While only the strike-slip orientation is being considered, we should point out that one of the advantages of the multipolar source representation is the availability of computational algorithms (e.g., Minster, 1973) for conveniently rotating the source to any desired orientation.

We now consider the earthquake source at focal depths of 10, 15, 25, 35, 45 km in the structure of Table 4.1. For each depth it is the multipole coefficients that remain constant and the source parameters then change according to the similarity properties of the model. The appropriate parameters are (4.6) and (4.8) and one intermediate to these and are summarized in Table 4.3. The stress drop for $S^{(0)} = 10^{-3}$ is given as well as the strain drop corresponding to events with constant stress drop, $\sigma^{(0)} = 100$ bars. Since each seismogram scales directly with $S^{(0)}$ or $\sigma^{(0)}$ it is easy to correct to other convenient values. The radiation patterns and spectra of Figures 4.3 and 4.4 apply equally well to any of these events, being scaled by the square of the velocity ratios. Note that for fixed strain drop, this is little different from scaling by stress drop ratios since $\sigma^{(0)} = \rho \beta^2 S^{(0)}$.

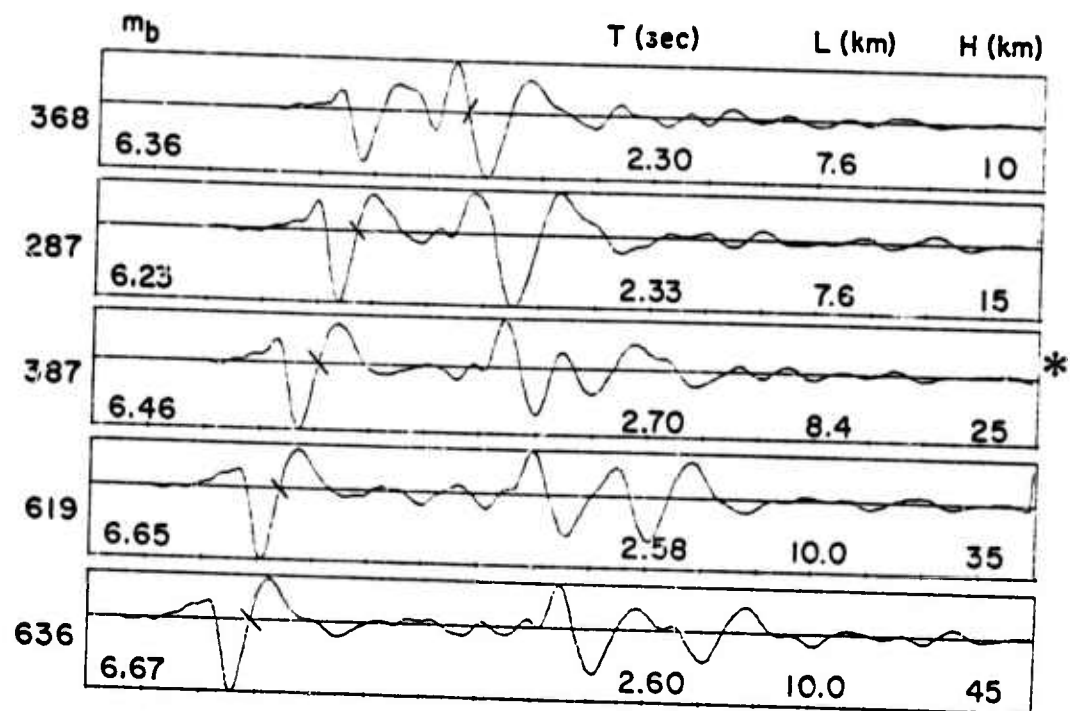
The synthetic seismograms are shown in Figures 4.5 and 4.6. These and all subsequent seismograms are for a

Table 4.3. Source Parameters for Events at Five Focal Depths

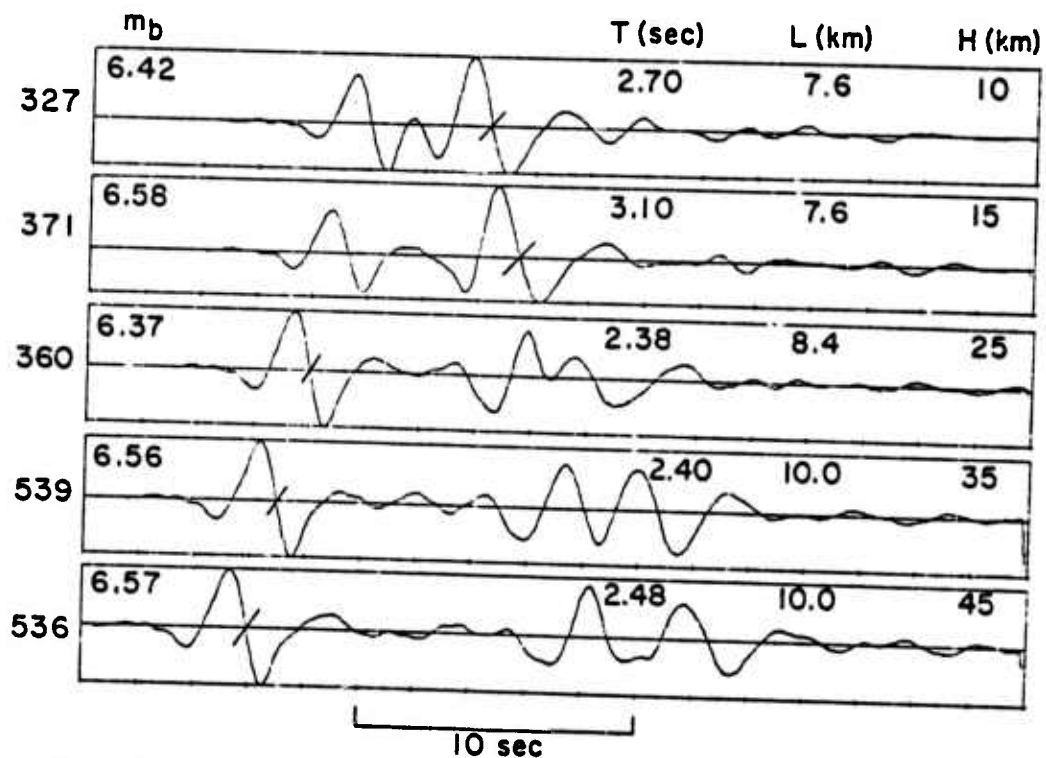
Source Depth h (km)	Fault Length L (km)	Rupture Velocity V_R (km/sec)	Stress Drop $\sigma^{(0)}$ (bars)	Strain Drop for $\sigma^{(0)} = 100$ bars
10, 15	7.6	3.15	343	0.29×10^{-3}
25	8.4	3.47	489	0.20×10^{-3}
35, 45	10.0	4.14	698	0.14×10^{-3}

constant stress drop of 100 bars. In Figure 4.5 are shown the records for events at the five focal depths and at two azimuths, $\phi = 45^\circ$ and 135° . The focal depth and fault length are indicated on each record together with the m_b , the phase from which the amplitude measurement was made and the apparent period of this phase. We have attempted, as much as possible, to analyze these records following standard field practice. The m_b was computed from $m_b = \log A/T + 3.3$ where A is measured peak-to-peak. The major influence of the apparent period, T , is in correcting to "true" ground motion since the instrument correction is large and rapidly varying in this period range.

In Figure 4.6 the azimuthal variation is shown for the 25 km focal depth event. Only azimuths from 0° to 180° are shown since the pattern is symmetric about the north-south (X_G) axis except for a change in sign. Of particular interest are the seismograms near $\phi = 90^\circ$ where the sense of first motion reverses. This azimuth is a node on the pattern for a simple double-couple representation of a strike-slip fault.



a. Azimuth, $\phi = 45^\circ$



b. Azimuth, $\phi = 135^\circ$

Figure 4.5. Theoretical seismograms at an epicentral distance of ≈ 4050 km and two azimuths with respect to the strike-slip earthquake sources of Table 4.3. All records have been scaled to stress drop $\sigma(0) = 100$ bars. The focal depth, fault length and m_b are indicated on each record. At left is the maximum peak-to-peak amplitude in millimicrons at 1 Hz. The bar indicates the phase at which the m_b measurement is made and T is the apparent period of this phase.

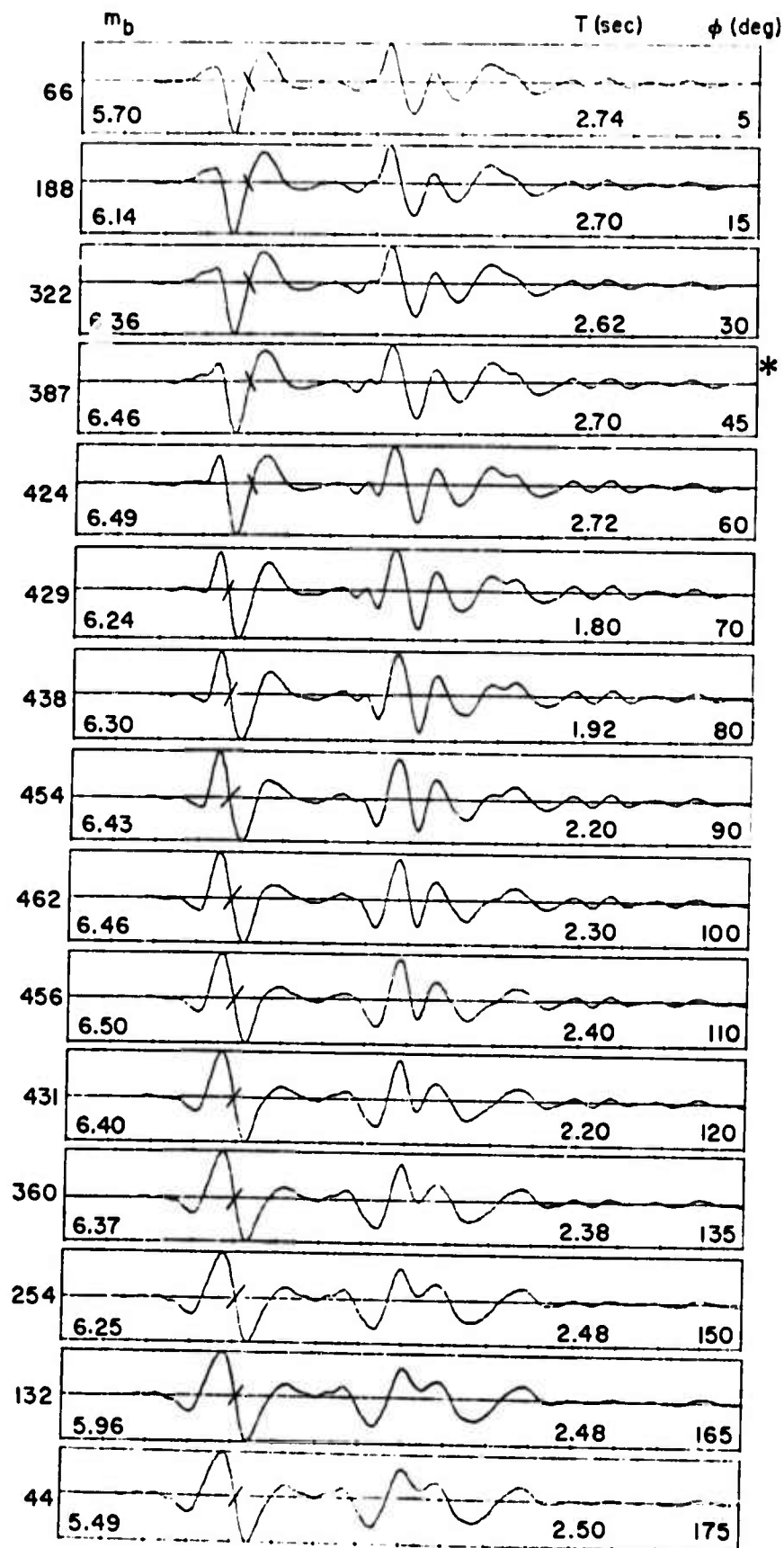


Figure 4.6. Theoretical seismograms at 15 azimuths ($0 < \phi < 180$) for the $L = 8.4$ km source at a 25 km focal depth. The m_b phase from which it was computed, apparent period of this phase and maximum peak-to-peak amplitude (1 Hz) are shown as in Figure 4.5.

4.5 ANALYSIS OF THEORETICAL SEISMOGRAMS

Our intention here is primarily to demonstrate the kinds of effects that can be included in the theoretical seismogram calculations. A detailed study of these effects and their implications for source mechanism studies is now underway. However, several interesting aspects of the theoretical seismograms of Figures 4.5 and 4.6 will be discussed. In particular, we address the questions: (1) What is the influence of the propagation effects introduced by the higher order multipoles?; and (2) How are the seismograms influenced by details of the crustal structure in the source region?

In Figure 4.7 we compare theoretical seismograms which differ only in the level at which the multipolar expansion is truncated. The $N = 6$ seismogram also appears in Figures 4.5 and 4.6 where it is marked with an asterisk. At this azimuth the most important effect of the higher order terms seems to be on the frequency content of the seismogram, as the dominant period of the maximum phase reduces markedly with addition of higher terms. Otherwise the pure double-couple ($N = 2$) seismogram includes most of the major features. Further computations verify that convergence is essentially attained at $N = 6$.

A fourth record is included in Figure 4.7 to demonstrate that the upper mantle response used in the computation is not frequency-independent but spreads the wave form somewhat. For this record a constant geometric spreading factor (GS) was used to represent the upper mantle rather than the response computed with a generalized ray theory program.

An overall view of the effect of the higher order multipoles (representing propagation) is given in Figure 4.8. Here the maximum amplitudes for the records of Figure 4.6 are normalized to the value for $\phi = 45^\circ$ and plotted versus azimuth. For a double-couple the amplitude ratios are $\sin 2\phi$ as

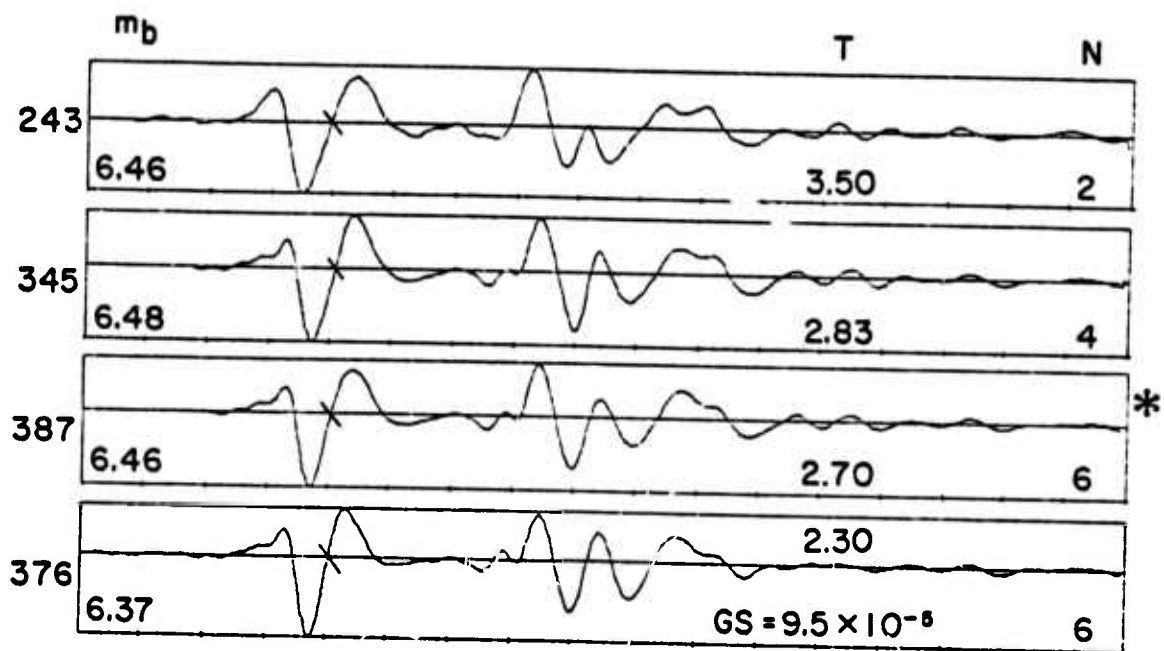


Figure 4.7. Theoretical seismograms at several levels of truncation (N) of the multipolar expansion. Otherwise the calculation is identical to that for Figure 4.5a. The fourth record differs from the third in that a constant spreading factor (GS) was used to represent the upper mantle.

indicated by the broken line on the figure. (Note that the amplitude for the $N = 2$ record of Figure 4.8 is 1.3 on the scale of this plot.) If m_b is plotted in this way the contrast with a double-couple pattern is somewhat greater due to the azimuthal variation of T . The figure shows that the higher order effects have a rather small influence on the average amplitude (or m_b) for a uniform azimuthal sampling but cause the pattern to be shifted strongly in the direction of fault propagation.

The records of Figures 4.5 - 4.7 are quite simple; all the important energy is in the P, pP and sP phases. The lag time between these phases is determined by the crustal structure, which otherwise has little influence on the seismogram. This is verified in Figure 4.9 where seismograms are shown that are identical to those in Figure 4.5a except that the source region crustal structure is now essentially a halfspace. (The properties of the first three layers of Table 4.1 were changed to $\alpha, \beta, \rho = 7.9, 4.6, 3.3$.) Comparing Figures 4.5a and 4.9, we see little alteration due to reflections from velocity contrasts within the structure. The pulse distortion due to the layering is, of course, strongly dependent on frequency but the long periods that dominate these records do not "see" velocity contrasts on the scale of those in the crustal structure used.

The amplitudes on the seismograms of Figure 4.9 are relatively constant; variations are primarily due to interference between the direct and free surface reflected phases. For the same (in terms of multipole coefficients) source in a layered crustal model, the amplitudes are considerably more varied as we saw in Figure 4.5. How much of this amplitude variation is dependent on the source parameter changes (Table 4.3) and how much is due to other properties of the layered model?

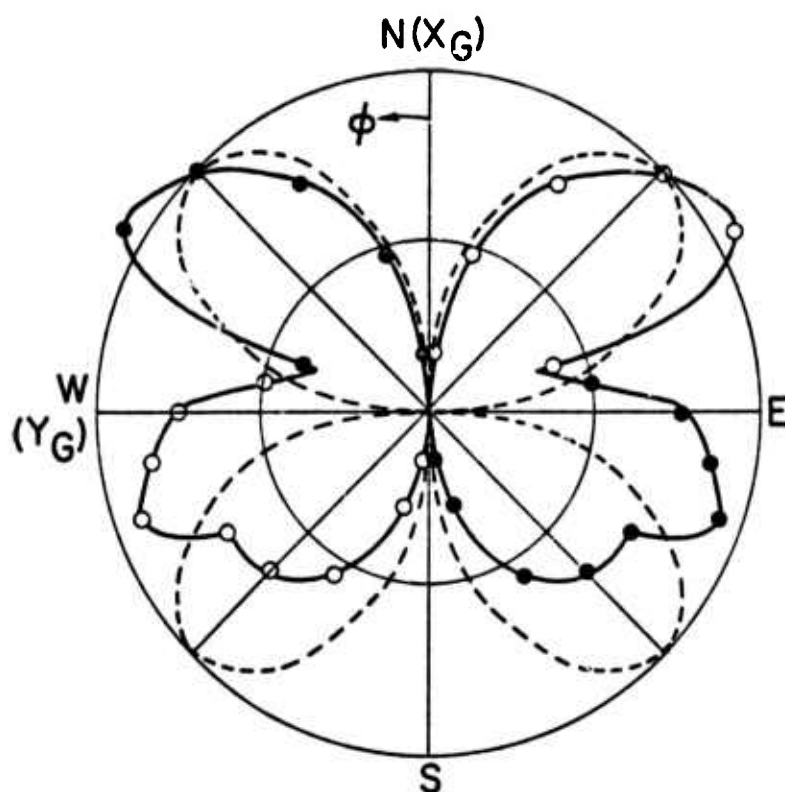


Figure 4.8. The maximum peak-to-peak amplitude versus azimuth for the strike-slip source at 25 km focal depth. The amplitudes are from the records of Figure 4.6 and are normalized to that for $\phi = 45^\circ$. The closed circles represent an upward (compressional) first motion and the open circles are for downward first motion. The broken line indicates the normalized amplitudes expected for a simple double-couple source. The circles are for amplitude ratios of 0.5 and 1.0.

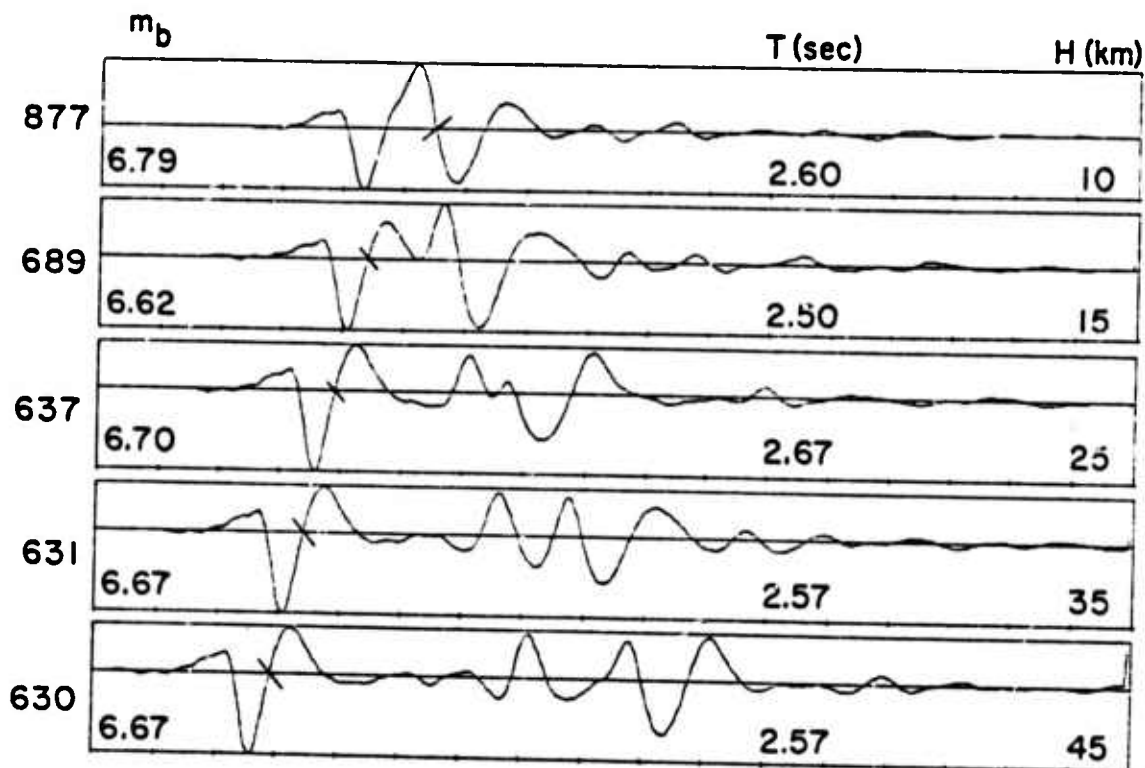


Figure 4.9. Seismograms like those of Figure 4.5a except that the first three layers of the source region crustal structure have been made identical to the fourth. The source at all depths is that specified by (4.6).

Assume that we can measure an amplitude on the seismogram that is proportional only to the direct P wave at a fixed frequency. This is nearly the case for the amplitude of the first cycle on the record which we denote by b . Then

$$b = \underline{P} \cdot \underline{T} \cdot \underline{U} , \quad (4.9)$$

where

\underline{P} - The transfer function applied to the displacements exiting the base of the crust. This is a constant for all seismograms shown here.

\underline{T} - The transfer function representing the crust at the source.

\underline{U} - The source generated displacement field at the period at which b is measured and along the ray that propagates to the receiver.

From (4.1) and (4.2) the \underline{U} may be written in the simplified form:

$$\underline{U} \approx \alpha_S^2 f(\tau, \phi) \underline{A}^\sigma(\omega) , \quad (4.10)$$

where α_S is the P wave velocity of the source material, $f(\tau, \phi)$ is the radiation pattern effect and $\underline{A}^\sigma(\omega)$ represents the multipole coefficients. For all the seismograms of Figures 4.5 - 4.7 and 4.9 we have fixed v , L/V_R , V_R/β and the stress drop $\sigma^{(0)}$. The $\underline{A}^\sigma(\omega)$ is then proportional to strain drop for which the variation with depth is indicated in Table 4.3. The superscript σ indicates that $\sigma^{(0)}$ is fixed. The $f(\tau, \phi)$ is determined from radiation patterns, like those of Figure 4.3, at the dominant frequency for the b cycle. The takeoff angle for the $f(\tau, \phi)$ is not constant with depth but varies according to Snell's law.

That is,

$$\tau \approx \sin^{-1} \alpha_S / c , \quad (4.11)$$

the c being fixed by the upper mantle response.

Bache, et al. (1975) showed that the crustal transfer function, T , reduces to approximately α_S^2 / α_b^2 , where α_b is the P wave velocity of the underlying "basement" material that is common to all events. Combining all these factors we see that:

$$b \approx \alpha_S^4 f(\tau, \phi) A_z^\sigma(\omega) . \quad (4.12)$$

The success of (4.12) in predicting the b amplitude for the seismograms of Figure 4.5 is summarized in Table 4.4. The $A_z^\sigma(\omega)$, $f(\tau, \phi)$ and the predicted and measured b are all normalized to the values for the deepest source. The T_b is the apparent period of the b phase from the records and is seen to be nearly constant. Radiation patterns at $T_n = 1.67$ for $\phi = 45^\circ$ and $T_n = 2.94$ for $\phi = 135^\circ$ were used to determine the $f(\tau, \phi)$. This value was then adjusted to the apparent period of the measurement by multiplying by $(T_b/T_n)^2$, this correction being motivated by the slope of the spectrum in this period range (see Figure 4.4).

Comparison of the predicted and actual normalized b amplitudes in Table 4.4 indicates that (4.12) gives a reasonably good prediction of the relative amplitudes on the body wave seismograms. The differences can be attributed to measurement errors and the fact that the approximations employed are not exact.

The scaling given by (4.12) should be taken into account when evaluating the dependence of teleseismic amplitudes on the source parameters. We have employed the scaling

to events with constant v , L/V_R , V_R/β and $\sigma^{(0)}$ where the multipole coefficient factor $A^\sigma(\omega) \approx \mu_S^{-1}$. It has been suggested (e.g., Kanamori and Anderson, 1975) that strain drop is relatively constant for large events. For constant strain drop events the $A^\sigma(\omega)$ is replaced by $A^S(\omega)$ which is invariant for the events compared in Table 4.4. However, in this case the relative amplitudes on the seismograms are scaled by ratios of μ_S and the normalized amplitudes in the table remain the same.

Table 4.4. Scaling of b Amplitudes for the Records of Figure 4.6

Depth (km)	α_S (km/sec)	$A^\sigma(\sigma^{(0)}) =$ \approx 100 bars)	$f(\theta, \phi)$	Predicted b	Actual b	T_b
$\phi = 45^\circ$						
10	6.0	2.03	0.53	0.35	0.37	1.63
15	6.0	2.03	0.61	0.41	0.48	1.75
25	6.7	1.43	0.64	0.47	0.55	1.67
35	7.9	1.00	0.98	0.98	0.90	1.72
45	7.9	1.00	1.00	1.00	1.00	1.74
$\phi = 135^\circ$						
10	6.0	2.03	0.64	0.43	0.45	2.90
15	6.0	2.03	0.55	0.37	0.38	2.70
25	6.7	1.43	0.69	0.51	0.55	2.80
35	7.9	1.00	1.05	1.05	1.08	3.07
45	7.9	1.00	1.00	1.00	1.00	3.00

If we restrict attention to body wave recordings at distances beyond the upper mantle triplication and from stations where the local crustal reverberations are small, most of the travel path effects are minimized and the record complexity can be attributed to the complexity of the source. This observation is born out by at least some teleseismic recordings of large underground explosions. However, even when the travel path effects are minimized, most earthquake recordings remain quite complex. In this sense the synthetic seismograms presented here are too simple to be realistic. An actual earthquake, especially one with a fault length near 10 km, can hardly be a single event characterized by a single stress drop, rupture velocity, etc. In fact, we would expect such an earthquake to be composed of many smaller events, each with its own fault parameters. From this point of view our single source model is too idealistic to provide a detailed synthesis of an actual earthquake recording. But this was not really our objective.

The development of a capability for simulating the earthquake source and propagation of the resulting seismic waves is a step-by-step process in which increasing levels of complexity are added as the need arises. Techniques for including more detail in both the source and propagation models are being considerably improved and the computational methods used in this paper were designed to link the two. At least one important "higher order" source effect is conveniently included in the Archambeau/Minster earthquake model used here; that is, the effect of finite velocity rupture propagation. The far-field radiation from such a source is quite different from that from a pure double-couple source representation as we saw in the patterns of Figure 4.3. For teleseismic body wave observations, the consequences include a pronounced shift of the teleseismic

body wave radiation pattern in the direction of rupture propagation (Figure 4.8).

A scaling law for teleseismic body wave amplitudes, subject to certain similarity constraints on the source, is an interesting consequence of the seismogram computations presented. The first constraint is that Poisson's ratio be fixed for the source regions being compared. Then if the ratio of fault length to rupture velocity (L/V_R) and rupture velocity to shear velocity (L/β) are fixed,

$$a \approx \alpha^4 f(\tau, \phi) \tilde{A}(\omega) \quad (4.13)$$

where a represents the amplitude of either the direct P or S wave. The $f(\tau, \phi)$ is the radiation pattern effect which depends on the azimuth (ϕ) and takeoff angle (τ) for the ray contributing to the a amplitude. The $\tilde{A}(\omega)$ represents the source strength (the multipole coefficients) and it is to this term that the similarity constraints apply. The dependence of $\tilde{A}(\omega)$ on the source parameters is discussed by Archambeau and Minster (1976). One important property is that $\tilde{A}(\omega)$ is directly proportional to strain drop ($S^{(0)}$). The α^4 factor includes α^2 for converting $\tilde{A}(\omega)$ to displacement and α^2 which accounts for the propagation from the source material into the underlying mantle material that is assumed to be fixed for the events being compared.

V. THE MULTIPLE ARRIVAL RECOGNITION SYSTEM

5.1 INTRODUCTION

This section of the report is devoted to a description of the mode of operation of the Multiple Arrival Recognition System (MARS) computer code and the application of this code to explosion seismograms. The MARS code is proving to be particularly effective for detecting, isolating and timing the various seismic phases (P_g , P^* , P_n , S_g , S^* , S_n , etc.) that are recorded on event seismograms in the near-regional and regional distance ranges. This signal analysis capability is finding immediate application to the problem of depth determinations for shallow focus events. More accurate event depth determinations can be obtained by incorporating P and S wave arrival times in standard hypocentral location routines and by the combined use of spectra of the isolated body waves for identification of spectral nulls caused by the interference of direct and free-surface reflected phases. Future tests on the MARS code should involve a systematic analysis of three-component data recorded at near-regional, regional and teleseismic distances from Eurasian events.

As reported in previous reports written under this contract (Bache, et al., 1975; Savino, et al., 1975), the relatively effective spectral discriminant, referred to as the variable frequency magnitude (VFM) discriminant, is embodied in the MARS code. In Chapter VI of this report, we will describe the results of the application of the VFM discriminant to synthetic seismograms and to observed seismograms for earthquake and explosion populations in Eurasia and North America.

5.2 DESCRIPTION OF MARS

The central feature of the MARS signal analysis code is the use of narrow band frequency filters to break up or

decompose a time series consisting of signal plus noise or just noise into a set of quasi-harmonic modulated "signals". This set of filtered signals, one for each filter center frequency, can then be used to determine the energy arrival time (the group time, t_g) and amplitude of the signal for each filter frequency by analysis of the time modulation of the filter outputs. Further, both the instantaneous phase and frequency of the individual filter outputs, that is the apparent phase and frequency of the quasi-harmonic filter output as a function of time, can be determined quite simply. Thus, if two components of the same vector wave field are analyzed in this fashion, the difference in the instantaneous phase between the two components is a direct measure of the polarization of the wave field.

Thus, the decomposition of the signal wave train, possibly composed of many individual signal pulses, into quasi-harmonic signals provides the means of determining arrival time, amplitude and wave polarization all as functions of frequency. This then is the basic signal information that can be used to detect a given type of signal in terms of its dispersion and polarization characteristics and to obtain its spectrum as well as its time and amplitude relation with respect to other signals present in a complex wave train.

Figures 5.1 and 5.2 are two different versions of the flow of operations in the MARS code. Figure 5.1 gives a verbal outline while Figure 5.2 summarizes the key mathematical operations performed in this signal analysis code. More detailed developments of the theory and operation of MARS were presented in Bache, et al. (1975) and Savino, et al. (1975).

Seismic data are read into MARS in the form of a time series (Figures 5.1 and 5.2) generally of about 500 - 2000 points in length. The data are then optionally detrended,

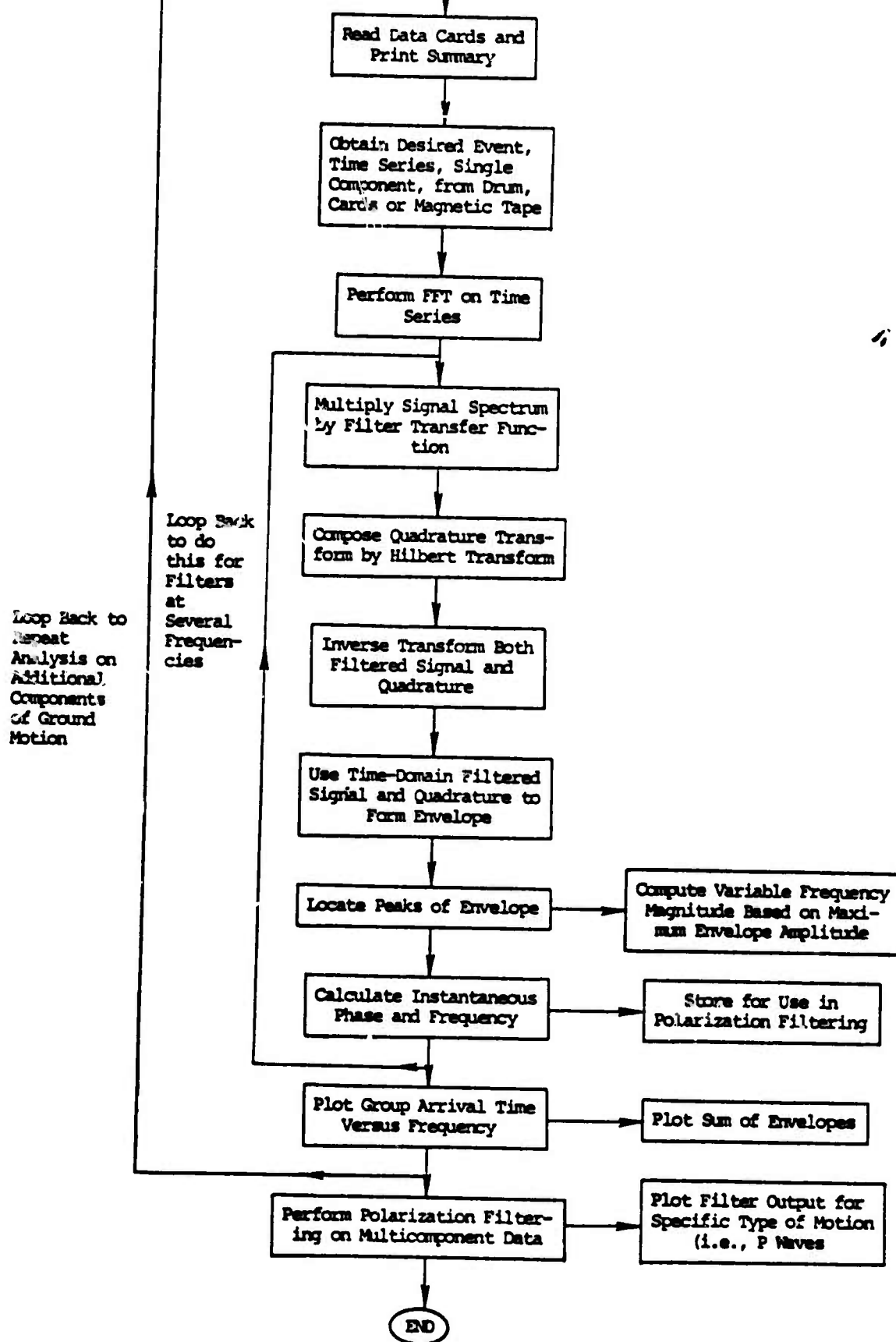


Figure 5.1. MARS flowchart.

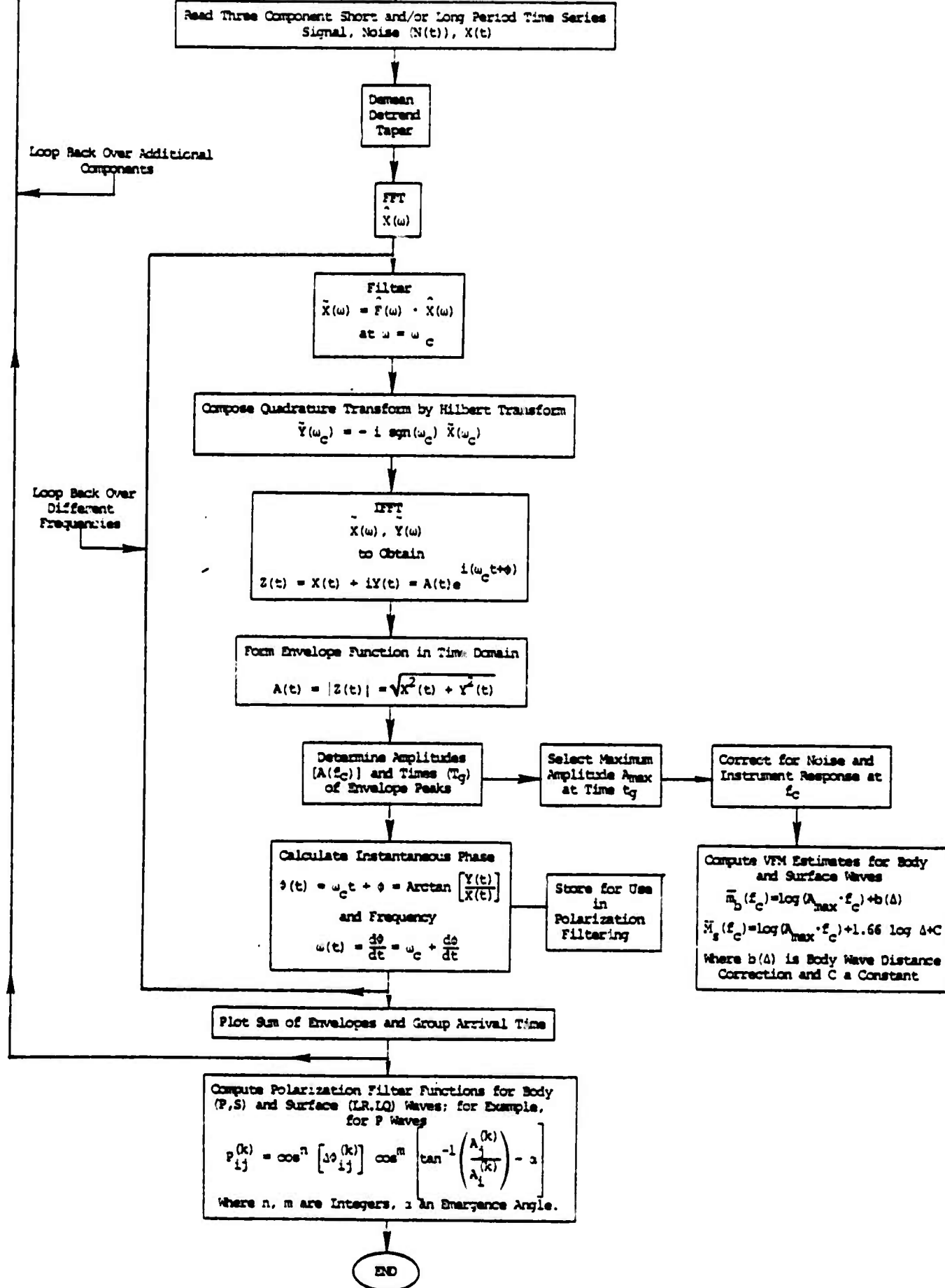


Figure 5.2. Flowchart indicating principal mathematical operations embodied in the MARS code.

mean removed and tapered at the tail end by a cosine bell. MARS then selects the smallest power of two which is greater than the number of points input and performs a discrete Fourier transform using the algorithm of Cooley and Tukey (1965). Both the original time series and the spectrum are plotted for examination.

Referring to Figures 5.1 and 5.2, the signal is next filtered in the frequency domain by multiplication with a narrow-band cusp-shaped filter. This particular filter form is selected to satisfy two goals: (1) minimum width in the frequency domain, and (2) maximum ripple suppression in the time domain. A well-known consequence of the Uncertainty Principle (Sampling Theorem to electrical engineers) is that one cannot simultaneously satisfy these two goals to arbitrary precision. The filter employed in MARS was selected for its optimal time and frequency domain characteristics within the limits of the Uncertainty Principle.

Once the signal has been narrow-band filtered, MARS corrects it for the appropriate instrument response; the filtered signal transform is divided by the instrument transfer function. The resulting complex spectrum is then inverse Fourier transformed into the time domain, to produce what will hereafter be referred to as the filtered signal.

The narrow-band filtered signal will appear as a quasi-sinusoidal carrier wave contained within a smooth envelope. The next step in the MARS code (Figures 5.1 and 5.2) is to construct the envelope function by means of the Hilbert transform. This method is followed in MARS: the transform of the filtered signal is multiplied by $-i \operatorname{sgn}(\omega)$ and then brought to the time domain by an inverse transformation. The maximum of the envelope function is utilized in the VFM discriminant while the instantaneous frequency and phase are stored for subsequent use in polarization filtering with additional components of ground motion.

The narrow-band filtering procedure can be performed on a particular component seismogram (time series) at a number of different frequencies within some band of interest. Correlation of the resulting envelope functions indicates the arrival times of the various frequency components. Then, for example, the group velocity dispersion can be deduced from the variation of the wave group arrival time (t_g) with filter center frequency (f_c). An application of MARS for determining Rayleigh wave dispersion along a North American travel path was discussed by Barker, et al. (1976).

In the event that multicomponent ground motion data are available, polarization filters, designed to pass ground motion having the appropriate particle motion, can be applied to the filtered data for the purpose of identifying and separating waves of differing polarization. Polarization filtering in MARS is always performed on time series which have previously been narrow-band filtered. The rationale for this procedure is that, in general, the spectral content of the signal (e.g., body wave) differs from that of the recorded background noise. As a result, the application of filters of appropriate frequencies can usually enhance the signal-to-noise ratio thereby partially isolating frequency components of the signal for further processing.

5.3 MARS ANALYSIS OF THE NTS EXPLOSION CHARTREUSE

On May 6, 1966, at 15:00:00.1 GMT, the underground explosion code-named Chartreuse was detonated in the Pahute Mesa area at the Nevada Test Site (NTS). Digitally recorded seismograms for Chartreuse were obtained from two stations of the Long-Range Seismic Measurements (LRSM) network for processing with the MARS code. These stations and epicentral distances are: Mina, Nevada (MNNV) at 201 km and Kanab, Utah (KNUT) at 312 km.

We are primarily interested in detecting and identifying the body-wave phases that are not commonly noted in near regional explosion seismograms. To detect and identify shear vertical phases hidden in dominating Rayleigh wave signals requires the utilization of polarization filtering.

The instantaneous phase ϕ_n determined from variable frequency narrow-band filtering is input directly to the polarization filter routine of the MARS. The linear polarization fraction can be defined using the instantaneous phase difference between the vertical (z) and radial (r) seismic components. Thus, the linear polarization fraction (P_L) is defined as

$$P_L(t) = \cos [\phi_z(t) - \phi_r(t)],$$

and the circular polarization fraction as

$$P_C(t) = \sin [\phi_z(t) - \phi_r(t)].$$

Therefore, it is clear that

$$P_L^2 + P_C^2 = 1,$$

and the two are, in a sense, mutually exclusive (Savino, et al., 1975).

For z-r data, different types of wave motion can be identified:

$$\text{P-wave: } P_L > 0 \text{ and } P_L > |P_C|;$$

$$\text{SV-wave: } P_L < 0 \text{ and } |P_L| > |P_C|;$$

$$\text{Rayleigh wave: } P_C < 0 \text{ and } |P_C| > |P_L|.$$

These types of motion can be displayed in time by multiplying the polarization fraction having the appropriate constraints

by the quasi-harmonic modulated waves resulting from the narrow-band filtering. Such results can then be displayed in the time versus frequency plane to provide arrival time estimations by alignment of non-dispersed P and S waves and indicated dispersive qualities of the Rayleigh waves. Refinement of arrival time estimations is achieved by forming the envelope functions (S) and averaging the envelope peaks over many frequencies. The envelope functions are formed in the following manner.

For the P wave

$$S_P(t) = \max(P_L(t), 0) \cdot \sqrt{S_Z^2(t) + S_R^2(t)}.$$

For the SV-wave

$$S_{SV}(t) = \max(-P_L(t), 0) \cdot \sqrt{S_Z^2(t) + S_R^2(t)},$$

and for the Rayleigh wave

$$S_R(t) = \max(-P_C(t), 0) \cdot \sqrt{S_Z^2(t) + S_R^2(t)},$$

where S_Z and S_R are narrow-band filtered time series of the vertical and radial seismic components.

Figure 5.3a shows the recorded vertical ground displacement at Kanab, Utah (KNUT). As a consequence of the short distance (312 km) between source and receiver, the record is very complicated, with many arrivals compressed into a fairly brief time interval. The time $t = 0$ on this record is actually 43.1 seconds after detonation time.

Simple visual inspection reveals that for the first 20-25 seconds, the record is dominated by motion at a relatively high frequency, the amplitude of which then decreases as the record is taken over by lower-frequency oscillations. In fact, at approximately 27 seconds into the record, two distinct

Charleuse KN-UT
5 May 1966

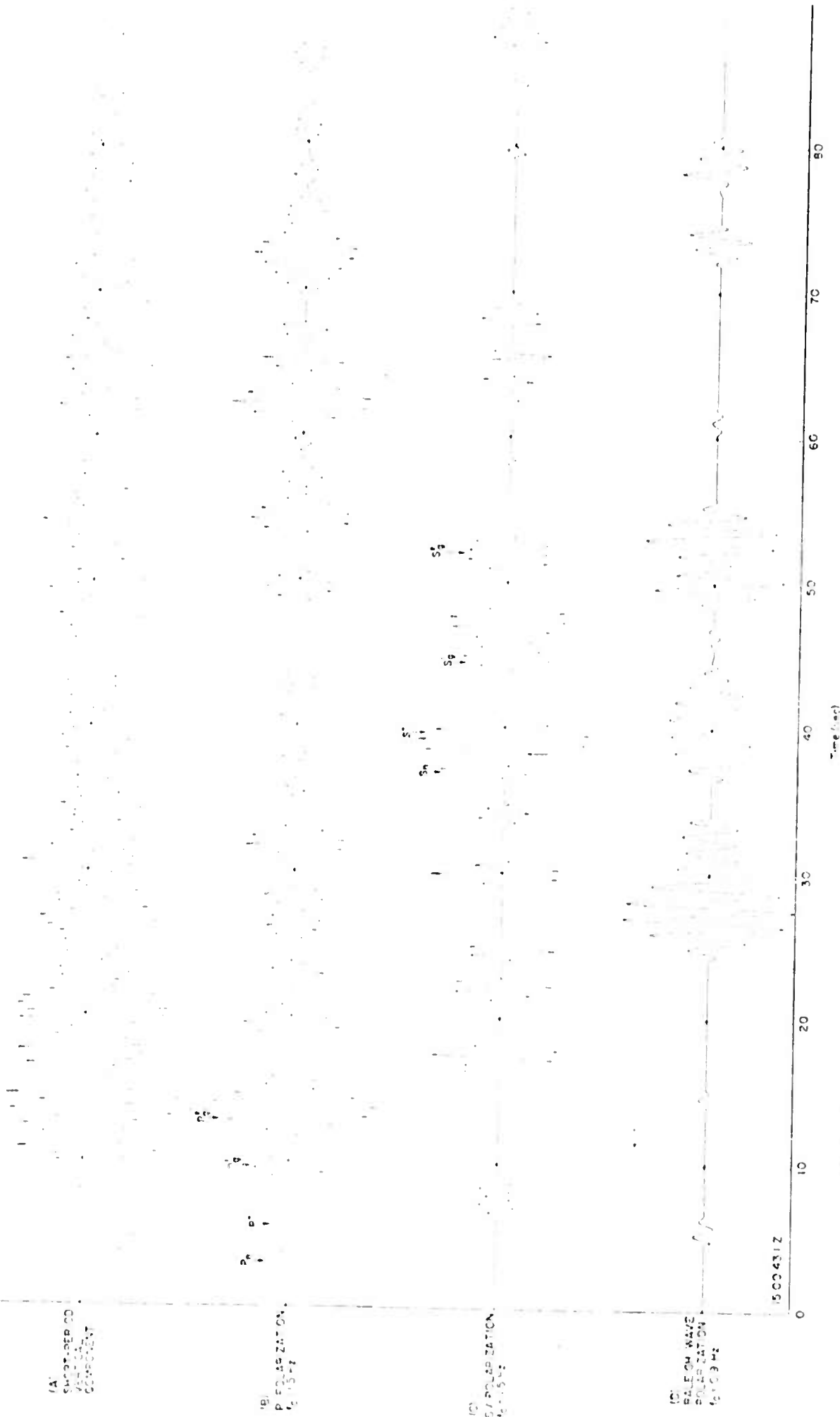


Figure 3.3. Polarization filtering of Charleuse-Punt record ($L = 312$ km) where indicated arrivals (arrows) are indicated times.

frequency components can be clearly seen. It would appear, from observation, that some improvement in phase separation could be made by narrow-band and polarization filtering.

The vertical and radial components of the Chartreuse-KNUT record were processed by the MARS code, with an eye to phase separation. The rapidly varying oscillations at early times appear to be at approximately 1.5 Hz. When this frequency is used for the narrow-band filter, the resulting P- and SV-waves are as shown in Figures 5.3b and 5.3c, respectively.

Formulae for the travel times of certain body wave phases were given by Gutenberg (1944) and modified by Evernden (1967) who shows that for the path from NTS to KNUT a Moho P velocity of 7.8 to 7.9 is appropriate. For the travel path of interest, the travel times for P-waves are as given below:

$$t(P_n) - t(0) = X + \frac{\Delta}{7.8} = 46.2 \text{ sec},$$

$$t(P^*) - t(0) = 4.4 + \frac{\Delta}{6.94} = 49.4 \text{ sec},$$

$$t(P_g^1) - t(0) = 1.2 + \frac{\Delta}{6.05} = 52.8 \text{ sec},$$

$$t(P_g^2) - t(0) = \frac{\Delta}{5.58} = 55.9 \text{ sec}.$$

In these equations, $X = 6.2$ is the surface-to-Moho travel time, and $\Delta = 312$ km. The four computed times are indicated in Figure 5.3b; it must be kept in mind that the origin is shifted by 43.1 seconds. It is clear that MARS has identified P wave phases with arrival times approximately the same as in the tables. The remaining bursts of 1.5 Hz P-wave energy are not currently identifiable, and are presumably due to more complicated travel times, involving multiple reflections.

Gutenberg (1944) gives travel time equations for corresponding shear body phases. These times work out to be:

$$t(S_n) - t(0) = Y + \frac{\Delta}{4.31} = 80.9 \text{ sec}$$

$$t(S^*) - t(0) = 6.9 + \frac{\Delta}{4.10} = 83.0 \text{ sec}$$

$$t(S_g^1) - t(0) = 2.1 + \frac{\Delta}{3.65} = 87.6 \text{ sec}$$

$$t(S_g^2) - t(0) = \frac{\Delta}{3.28} = 95.1 \text{ sec}$$

where $Y = 8.5$ seconds and $\Delta = 312$ km. The appropriate times are indicated in Figure 5.3c, where they clearly correspond to recognizable S-wave arrivals. Additional wavepackets are visible, some at earlier times, but these are presumably attributable to P-S converted waves which travel most of the distance at the longitudinal wave speed.

The low frequency oscillations which are visible in Figure 5.3a can be brought out by the application of an 0.9 Hz narrow-band filter. When this is done, the P_n wave appears quite distinctly, the P^* disappears, while the P_g^1 and P_g^2 merge into one wavepacket. The 0.9 Hz P-waves are not illustrated here, since they do not show anything not previously seen.

For 0.9 Hz, the projected Rayleigh waves are as shown in Figure 5.3d; several clear arrivals can be seen between record times of 25 and 55 seconds. Given the distance of 312 km, and the $t = 0$ offset of 43 seconds, these wavepackets have been traveling at between 3.2 and 4.6 km/sec. These group velocities are consistent with the values for higher mode Rayleigh waves observed by others for the Basin and Range region, Alexander (1963).

Figure 5.4a shows the vertical ground displacement at Mina, Nevada (MNNV). In general this record is similar to that shown for KNUT (Figure 5.3a). However, this station is

Chartreuse VN-NV
6 May 1966

(A)
SUPERSEED
1500-1500
1500-1500

(B)
P POLARIZATION
1500-1500

(C)
SV POLARIZATION
1500-1500

(D)
RAISON WAVE
POLARIZATION
1500-1500

150027.2

80

70

60

50

40

30

20

10

0

Time (sec)

Figure 5.4. Polarization filtering of Chartreuse-VN-NV record ($L = 201$ km) where indicated arrivals (arrows) are predicted times.

located 201 kilometers from the Chartreuse epicenter, which is considerably closer to the explosion than KNUT (312 km). Thus, similar individual seismic signals identified at the KNUT station will arrive earlier and closer together in time. Consequently, separation of these individual seismic signals can only be accomplished with the use of relatively higher frequency narrow-band filters.

In the following figures, 5.4b, 5.4c and 5.4d, we show the polarization filter outputs for the frequency (2.8 Hz body waves and 0.9 Hz Rayleigh waves) that best delineate in time the individual seismic signals. At this station we are unable to identify a P^* or S^* (Figures 5.4b and 5.4c). Gutenberg (1944) and Herrin (1961) travel-time tables indicate that for this distance P^* should arrive about one second later than the P_n . On the other hand, Herrin (1968) travel-time curves indicate that P^* should arrive several tenths of a second earlier than P_n . Further, for the total series of narrow-band filters applied, we observed no clear seismic P arrival between the P_n and P_g^1 seismic phase.

As for KNUT, we show the projected Rayleigh waves at 0.9 Hz for MNNV, and as before the group velocities of the major wave packets are consistent with the values for higher mode Rayleigh waves observed by others for the Basin and Range region.

Rayleigh wave motion dominates the later (in time) portion of both the MNNV and KNUT seismograms; however, polarization filtering clearly defines the important SV phases which would be most difficult if not impossible to pick from the original seismograms (Figures 5.3a and 5.4a).

Comparison of the predicted P and S travel-times to the corresponding observed travel-times are given in Table 5.1. Differences between predicted and observed times range up to 0.7 second.

Table 5.1. Predicted Versus Observed Travel-Times

Travel-Times for KNUT			
Phase	Predicted (sec)	Observed (sec)	Residual (sec) (Predicted-Observed)
P _n	46.2	46.4	-0.2
P*	49.4	48.7	+0.7
P _g ¹	52.8	52.8	0.0
P _g ²	55.9	56.2	-0.3
S _n	80.9	80.4	+0.5
S*	83.0	82.7	+0.3
S _g ¹	87.6	88.1	-0.5
S _g ²	95.1	95.2	-0.1
Travel-Times for MNNV			
P _n	32.0	32.3	-0.3
P _g ¹	34.4	34.1	+0.3
P _g ²	36.0	36.4	-0.4
S _n	55.1	55.4	-0.3
S _g ¹	57.2	57.3	-0.1
S _g ²	61.3	61.0	+0.3

Thus, with the use of MARS we have detected, identified, isolated and accurately times P, S and Rayleigh seismic phases at a small epicentral distance. Especially noteworthy is the detection of S_n since this phase is rarely observed from explosions.

5.4 DISCUSSION OF DEPTH ESTIMATION

5.4.1 Location Programs

If very accurate estimates of the origin time are available, one can generally determine the depth of focus with considerably less error than when neither origin times nor focal depth are constrained. In many cases, one can use P and S travel-times together to improve estimates of location and depth, though this fact has not been exploited in widely used location programs.

One method of determining the origin time of a seismic event is to measure the arrival times of P and S waves that follow the same propagation path from source receiver (e.g., $t(P_n)$, $t(S_n)$; $t(P_g)$, $t(S_g)$; and etc.). Several stations at varying distances are required such that when plotting P versus S arrival times, the point $t(S) - t(P) = 0$ is well determined. This time will be the event origin time.

Evernden (1969) performs an exercise utilizing P_g and S_g arrival times for the Bilby and Aardvark NTS explosions and determines origin times within 0.5 seconds of the real times. He also points out that the errors in picking the P_g and S_g times are commonly on the order of 2 seconds. Application of MARS for determination of various P and S arrival times will significantly reduce the error and the number of stations required. This allows a more accurate estimate of

origin time. Evernden (1969) indicates that if the origin time is constrained with an error of 0.5 seconds, the location computation gives depth estimates of 0 ± 4.5 km for NTS explosions. The travel-time curves used by Evernden in the location computation were those of Herrin (1961). These are not entirely accurate for the western United States, but even if they were, the depth errors would have been only slightly less so. Very accurate travel-time curves are required for accurate depth estimations when using unconstrained origin times and depths in the location computation.

Figure 5.5 is a plot of the P and S arrival times determined and discussed previously for MNNV and KNUT. A mean line determined by a least squares fitting to the origin time of 14:59:59.8 or 0.3 seconds earlier than the actual origin time. The standard deviation of the points normal to the line is ± 0.3 seconds. These results are remarkable. However, we must keep in mind that only two stations were used and the excellent results may be fortuitous. More station data at differing distances would provide added confidence in the origin time estimate.

In conclusion, substantially improved depth estimates can be obtained by using MARS to pick accurate arrival times for P and S phases from seismograph recordings at distances of 150 to 1500 km. With the accurate arrival times we can closely constrain the event origin time which, in turn, is used to constrain the depth estimate.

5.4.2 Spectra for Narrow-Band Filtering

When the location computation indicates that the depth is shallow (0 ± 4 or 5 km), the spectra of the various body waves that are identified and isolated with the use of the MARS can be utilized to refine the depth estimation. Spectral nulls will occur due to the interference in the time

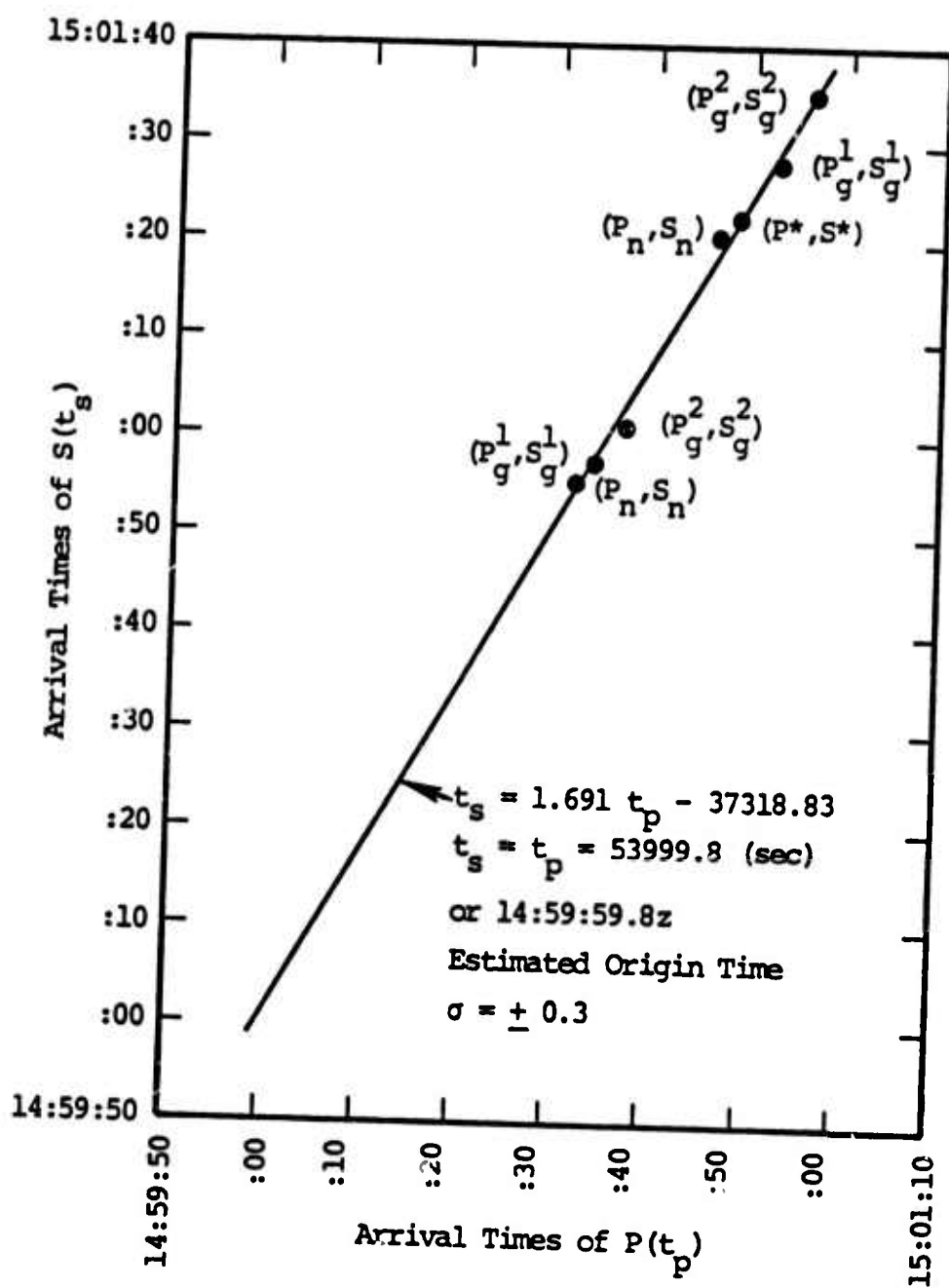


Figure 5.5. P and S arrival times at KNUT and MNNV from Chartreuse.

series of the depth phase (free-surface reflection) with the more direct downgoing wave.

Phase interference of this type may be represented by the following:

$$z(t) = y(t) - \beta y(t + \tau)$$

where

τ = delay time associated with the surface reflection,

$y(t)$ = initial source time function,

β = the surface reflection coefficient ($\beta \leq 1.0$).

The power spectrum of $z(t)$ is then:

$$P(\omega) = \left| \int_{-\infty}^{\infty} z(t) e^{-i\omega t} dt \right|^2$$

which becomes

$$P(\omega) = |Y(\omega)|^2 [1 + \beta^2 - 2\beta \cos \omega \tau].$$

Thus, nulls in the spectrum will occur $1/\tau$ Hz apart.

In Figure 5.6, we show the amplitude spectra for the seismic phases P_n , P^* , and P_g^2 as obtained from the series of narrow-band filters applied to the Chartreuse-KNUT record. We would expect that the delay times τ would increase with the increase of distance that the reflected wave must travel due to the increasing angle of incidence corresponding to each of these phases (P_n , P^* and P_g^2). This should be especially true for P_g^2 as compared to P_n since P_g^2 phase travels in the upper crust layers. In Figure 5.6 we observe that τ does increase as expected. This type of comparative spectral

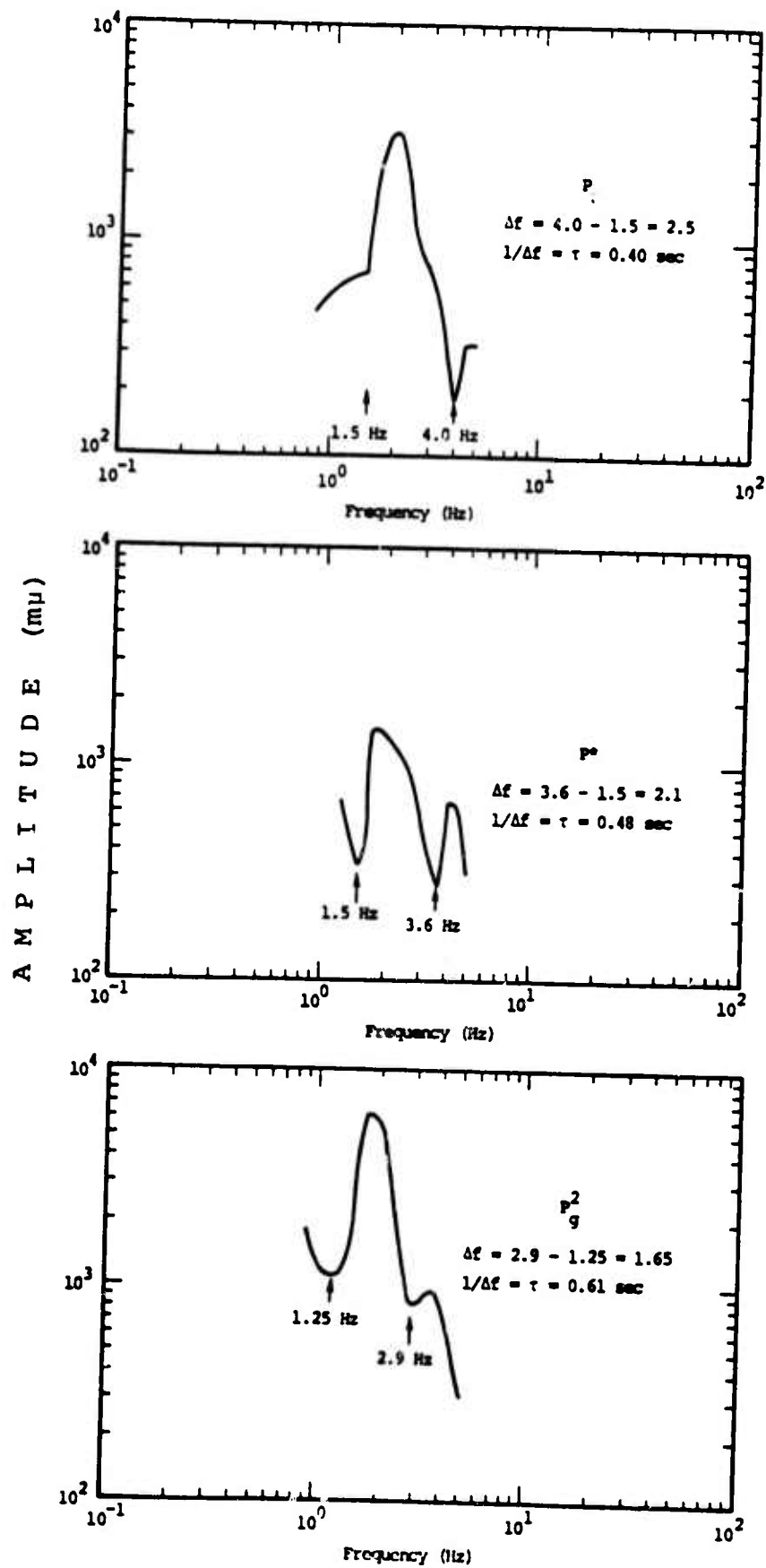


Figure 5.6. P_n , P^* , and P_g^2 amplitude spectra for Chartreuse-KNUT.

analysis greatly increases the confidence that can be placed on the selection of the spectral nulls for depth estimations of shallow events observed at one station. The inclusion of other station data will have the same effect. In fact, from stations having common seismic phase spectra, summation of these spectra will enhance the spectral nulls due to depth-phase interference and tend to cancel varying path and receiver effects.

5.5 SUMMARY AND RECOMMENDATIONS

We have demonstrated in part the utility of the MARS code from the seismic analyst's point of view. The specific problem of seismic event depth estimation was addressed. In this respect the MARS capability to detect, isolate, identify and accurately measure travel times and amplitudes of seismic phases making up an extremely complicated record can be used in a simple and effective way to obtain accurate estimates of event depth of focus.

In particular, the use of accurately determined arrival-times for various P and S waves that follow the same propagation path from source to receiver to obtain event origin times will yield improved depth estimations in the location computation. For those very shallow events, such as underground explosions, the use of various individual body wave spectra to clearly identify spectral nulls should virtually solve the problem of depth determinations for shallow seismic events, especially so if data from several recording sites are combined.

Future work should be concerned with a systematic test of the discussed procedures on a suite of Eurasian events recorded at stations located within near regional, regional and small teleseismic distances.

VI. VARIABLE FREQUENCY MAGNITUDE DISCRIMINANT

6.1 INTRODUCTION

An important aspect of the research program supported by the subject contract has been the development and testing of optimal procedures for discrimination between earthquakes and both single and multiple underground explosions. As previously reported (Bache, et al., 1974; Savino and Archambeau, 1974; Bache, et al., 1975; Savino, et al., 1975), this program has resulted in the formulation of a very effective variable frequency magnitude (VFM) discriminant which exploits spectral differences between earthquakes and explosions.

To date our attention has focussed on the application of the VFM technique to short period body waves recorded from events at teleseismic distances. A well-known limitation to the applicability of the much heralded M_s - m_b discriminant results from the inability of presently existing seismic networks to detect surface waves from low-yield explosions. For example, Basham and Whitham (1971) estimated that the detection threshold for 20 second Rayleigh waves from explosions was 0.5 to 0.7 magnitude units higher than the P wave threshold for the same event population. In the case of the VFM discriminant, obviating the requirement for recording surface waves from small explosions results in an extended magnitude range over which this discriminant can be applied. Based on the North American and Eurasian event populations examined so far, complete separation of earthquakes and explosions is achieved with the VFM technique down to event magnitudes, m_b , in the range 4.0 to 4.5.

Following a brief description of the physical basis for the VFM discriminant, the computational procedure followed in applying this technique will be outlined. Next the results of the application of the VFM technique to several large populations of explosions and shallow and deep focus

earthquakes recorded at the LASA, NORSAR and Yellowknife, Canada, arrays will be discussed. Then the effectiveness of the VFM technique for discriminating a simulated multiple explosion scenario will be tested. This section of the report will conclude with the application of the VFM discriminant to synthetic seismograms for earthquakes and explosions, and a comparison of the synthetic and observed VFM results.

6.2 PHYSICAL BASIS FOR THE VFM DISCRIMINANT

The variable frequency magnitude discriminant, originally proposed by Archambeau, et al. (1974), exploits spectral differences between underground explosions and earthquakes. The approach employed makes use of spectral body wave magnitudes computed from narrow-band filter outputs at frequencies generally in the range 0.4 Hz to 5 Hz, the actual frequencies being dependent on the particular source-to-receiver propagation path studied. These spectral magnitudes are denoted as $\bar{m}_b(f)$. In this report we will consider body wave magnitudes at different frequencies ($\bar{m}_b(f_1) : \bar{m}_b(f_2)$) for discrimination.

Differences in the far-field short period P-wave spectra for earthquakes and underground explosions have been reported by many investigators (Lacoss, 1969; Wyss, et al., 1971; Molnar, 1971). In general the observations indicate that if explosion and earthquake spectral levels are comparable at frequencies lower than 1 Hz (e.g., 0.5 Hz), then at higher frequencies (e.g., 2 Hz) the explosion spectrum is enriched relative to that for the earthquake. These observations led to the formulation of several different discrimination techniques designed to exploit these spectral differences; spectral ratio (Lacoss, 1969), and higher moments of frequency (Anglin, 1971; Manchee, 1972).

The combined effects of the free surface reflection, smaller source dimension, and peaked source function have

been invoked to explain the shape of short-period explosion spectra relative to earthquake spectra. The observed degradation of the lower frequency portion of explosion spectra has been attributed to the superposition of the direct P wave and the free surface reflected wave, pP (lagged in time and of opposite polarity to P), which results in differentiation of the spectral band with wavelength longer than twice the explosion depth (Fuchs, 1966). Spectral densities at frequencies smaller than $f_H = v_p/2H$, where v_p is the average overburden velocity and H the explosion depth-of-burial, should decrease with frequency. For typical values of v_p and H, f_H is near 1 Hz; slightly lower values for very large yield bombs and higher values for very low-yield bombs. While similar pP cancellation can occur for earthquakes, that portion of the spectrum affected is generally outside the teleseismically recorded short-period band owing to the greater focal depths of most shallow earthquakes.

Several authors (Wyss, et al., 1971; Molnar, 1971) have pointed out that the low frequency ($f < 1$ Hz) degradation in observed explosion spectra is usually faster than f , more like $f^{1.5}$. This has been attributed to the combined effects of a peaked source function and depth-of-burial.

Finally, the higher corner/peak frequencies for explosions as compared to corner frequencies for earthquakes of comparable m_b is thought to be a result of the smaller source dimensions of explosions (Wyss and Brune, 1968; Hasegawa, 1973; Wyss, et al., 1971). Rather dramatic examples of this are given in the paper by Wyss, et al. (1971), where four Aleutian earthquakes with magnitudes similar to the explosion Milrow were observed to have source dimensions at least an order of magnitude larger than those computed for Milrow.

The spectral characteristics that were discussed in the preceding paragraphs for earthquakes and explosions are displayed in Figure 6.1. This figure shows theoretical amplitude spectra for an explosion and an earthquake as viewed at

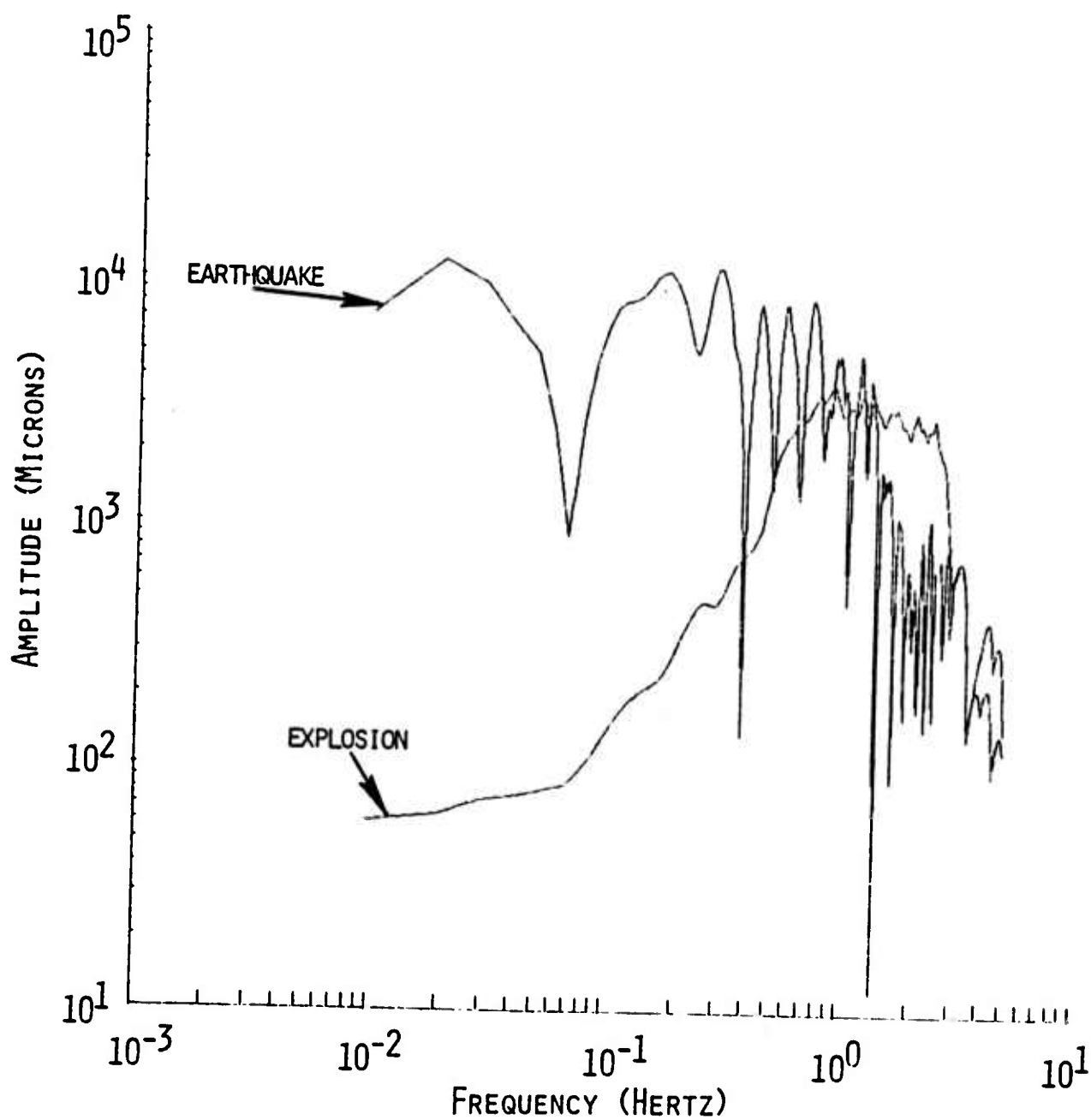


Figure 6.1. Event spectra at base of crust in the source region.

the base of the crust in the source region. These two events have equivalent body wave magnitudes at approximately 1 Hz. The effects of the free surface reflection and crustal reverberations are included in these spectra.

The explosion spectrum was computed for a 50 kt device at a depth-of-burial less than 1 kilometer. The source spectrum was computed using a finite difference computer code to model the nonlinear processes and elastic wave techniques to model the propagation of the resultant stress waves to the base of the crust (Bache, et al., 1975).

The earthquake spectrum is representative of a vertical strike-slip event with a fault length of 2 kilometers and a focal depth of 15 kilometers. The earthquake source model used in this calculation (see Section IV of this report) is that of Archambeau (1968, 1972) and Minster (1973).

As mentioned previously, the VFM discriminant is based on a comparison of spectral magnitude estimates made at a low frequency (e.g., $f \sim 0.4$ to 0.5 Hz) and a relatively high frequency (e.g., $f \sim 2$ to 3 Hz). Examination of the event spectra in Figure 6.1 indicates that the application of the VFM procedure in these frequency bands would clearly discriminate these two events. While the holes or nulls in the earthquake spectrum, which are due to reverberations in the crust, could certainly hamper discrimination for certain combinations of frequencies, with the use of several frequencies and a larger band width between the VFM estimates this potential problem can be avoided.

Propagation of both events through the same upper mantle and receiver structure will alter both spectra in the same way; however, if other stations or distances are used in combination for VFM discrimination, then such path effects must be carefully taken into account.

6.3 NARROW-BAND FILTERING

Determination of the VFM discussed above is accomplished with the use of a series of narrow-band filters. These filters form the basic analytic portion of the MARS signal processing code described in the previous section of this report. The signal is filtered in the frequency domain by multiplication with a cusp-type narrow-band filter of the form:

$$F(f) = \begin{cases} 1 - \cos \frac{\pi}{3} \left[\frac{f - \left(f_c - \frac{3}{2} \Delta f \right)}{\Delta f} \right] , & f_c - \frac{3}{2} \Delta f \leq f \leq f_c \\ 1 - \cos \frac{\pi}{3} \left[\frac{\left(f_c + \frac{3}{2} \Delta f \right) - f}{\Delta f} \right] , & f_c \leq f \leq f_c + \frac{3}{2} \Delta f \\ 0 , & \text{otherwise} \end{cases}$$

The filter is shown in Figure 6.2 and was chosen to minimize the time-domain ripple as discussed in Bache, et al. (1975). The width at one-half maximum amplitude is designated Δf .

Once a signal has been narrow-band filtered, MARS then corrects for the instrument response. If the resulting complex spectrum were inversely Fourier transformed into the time domain; it would represent a modulated carrier wave of the form:

$$x(t) = A(t) \cos (\omega_c t + \phi) , \quad \omega_c > 0 .$$

However, we compute the Hilbert transform of $x(t)$ by multiplying the complex spectrum by $-i \operatorname{sgn}(\omega)$ and then transforming into the time domain by an inverse transform (see Savino, et al., 1975, for the details). Using the signal and its Hilbert transform, the envelope and instantaneous frequency are produced.

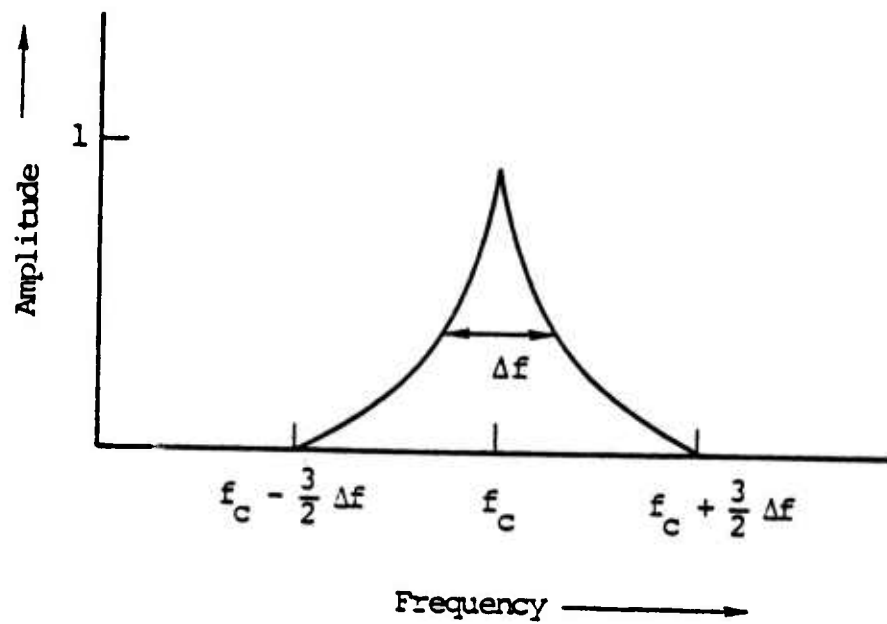


Figure 6.2. Narrow-band filter used in MARS.

Corresponding to each filter center frequency and envelope maximum (A_{\max}) a seismic body wave magnitude is determined. The procedure followed in MARS is to define the body wave magnitude as

$$\bar{m}_b(f_c) = \log (A_{\max} \cdot f_c) + B(\Delta)$$

where

$B(\Delta)$ = standard or conventional distance correction factor.

Each signal envelope maximum is corrected for noise by subtracting the maximum amplitude of an envelope function, computed in exactly the same manner as for the signal envelope, based on a noise segment immediately preceding the signal onset.

Examples of narrow-band filtered outputs for a presumed Eurasian explosion recorded by the Oyer subarray in Norway are shown in Figure 6.3. In this figure the unfiltered time series for the explosion is shown in the top left frame. The remaining frames show the outputs of five narrow-band filters of increasing center frequency ($f_c = 0.3$ to 6.0 Hz) going from top to bottom and left to right. The emergence of the signal from the noise at $f_c > 1.0$ Hz is quite remarkable. The persistence of high frequency signal energy is likely due to propagation along a high-Q path.

As defined in the previous paragraph, the $\bar{m}_b(f_c)$ estimates for this event would be based on the maximum amplitudes of the filter envelopes. As an example, the $\bar{m}_b(3.0 \text{ Hz})$ estimate would be based on the amplitude of the 3.0 Hz filter envelope at about 27 seconds into the filtered seismogram. This procedure for estimating $\bar{m}_b(f_i)$ will be applied to observed and synthetic waveforms in the following subsections of this report.

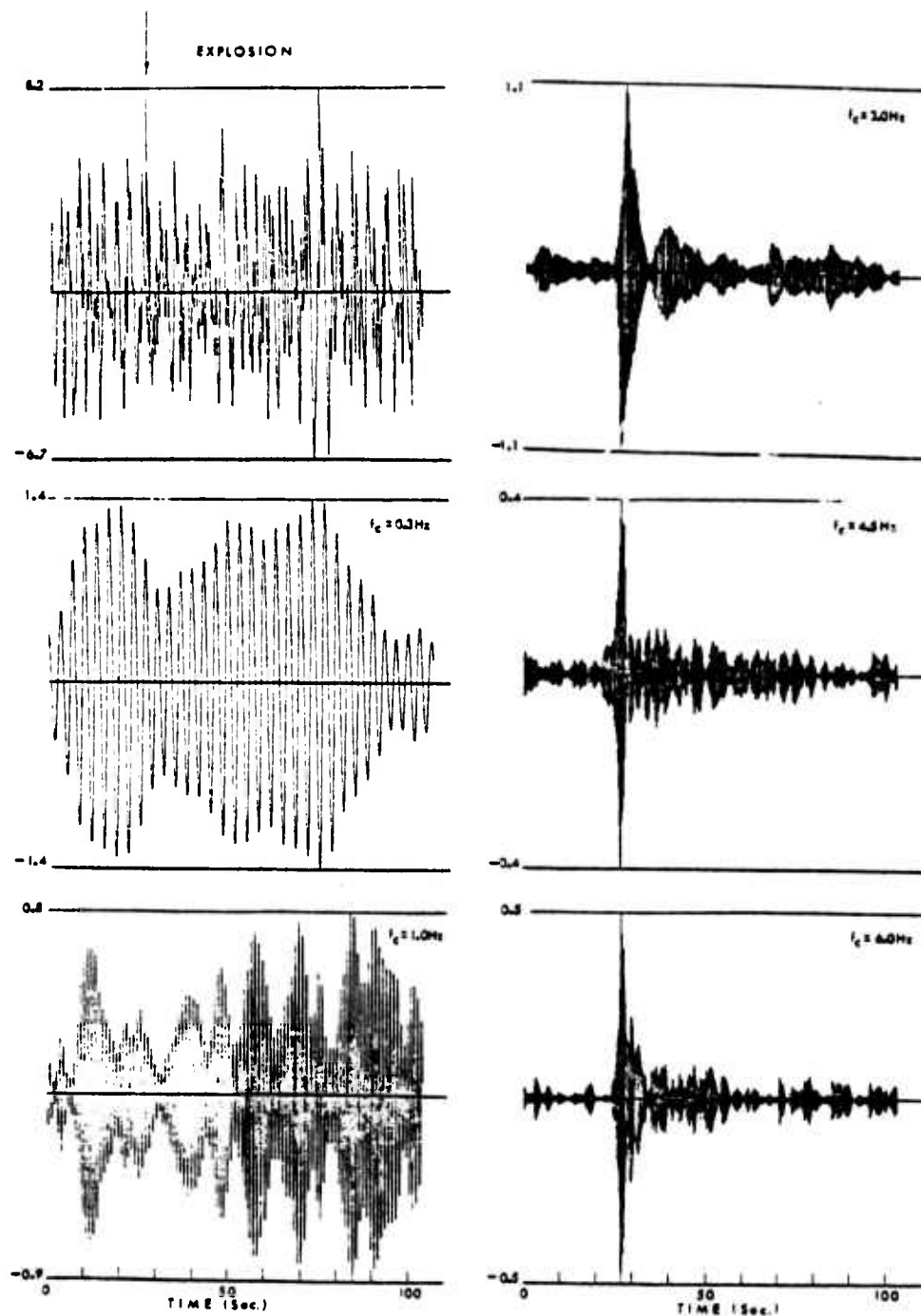


Figure 6.3. Examples of increasing signal-to-noise ratio for a presumed explosion (top left frame) recorded at Norway with successive application of high frequency narrow-band filters. Arrow at top denotes approximate arrival times of the P-wave on the unfiltered trace.

6.4 APPLICATION OF THE VFM TECHNIQUE TO OBSERVED EVENTS

6.4.1 Shallow Events Recorded at LASA and Norway

The data base employed in the first test of the VFM discriminant consists of LASA short-period recordings of P-wave trains from 34 presumed explosions and 156 earthquakes (Lacoss, 1969). Thirty of the presumed explosions originated within the mainland USSR, two in Novaya Zemlya, one (Longshot) in the Aleutians and one in the Sahara Desert. The earthquakes are distributed along the Alpine seismic belt, the Kuril-Kamchatka arc and the Arctic Ocean. The epicentral distances of these events range from 45° to about 100° with more than half of the events between 65° and 85° from LASA.

Figure 6.4 is a plot of spectral magnitude estimates, $\bar{m}_b(f_c)$, at a low frequency ($f_c = 0.45$ Hz) versus a high frequency ($f_c = 2.25$ Hz) for all 34 presumed explosions and those earthquakes in the data base that were reported in the Monthly Listing of Events, published by the USGS (formerly NOAA), as having shallow focal depths, $h < 70$ km. This figure clearly demonstrates the enriched high frequency content of the explosion body wave spectra as compared to the earthquake spectra. For instance, for a given value of $\bar{m}_b(0.45 \text{ Hz})$ the explosions exhibit $\bar{m}_b(2.25 \text{ Hz})$ values that are typically 0.6 to 1.0 unit larger than the $\bar{m}_b(2.25 \text{ Hz})$ values for earthquakes.

The high degree of discrimination of earthquakes from explosions evident in Figure 6.4 is especially significant in view of the non-regionalization of the event population. The variety of tectonic settings of this event population ranges from relatively stable shield regions to seismically active oceanic arc systems. An indication that discrimination could be further enhanced by regionalizing the event population comes from the fact that for $\bar{m}_b(2.25 \text{ Hz}) > 4.0$ the two presumed explosions (#35 and #138) plotting closest to the

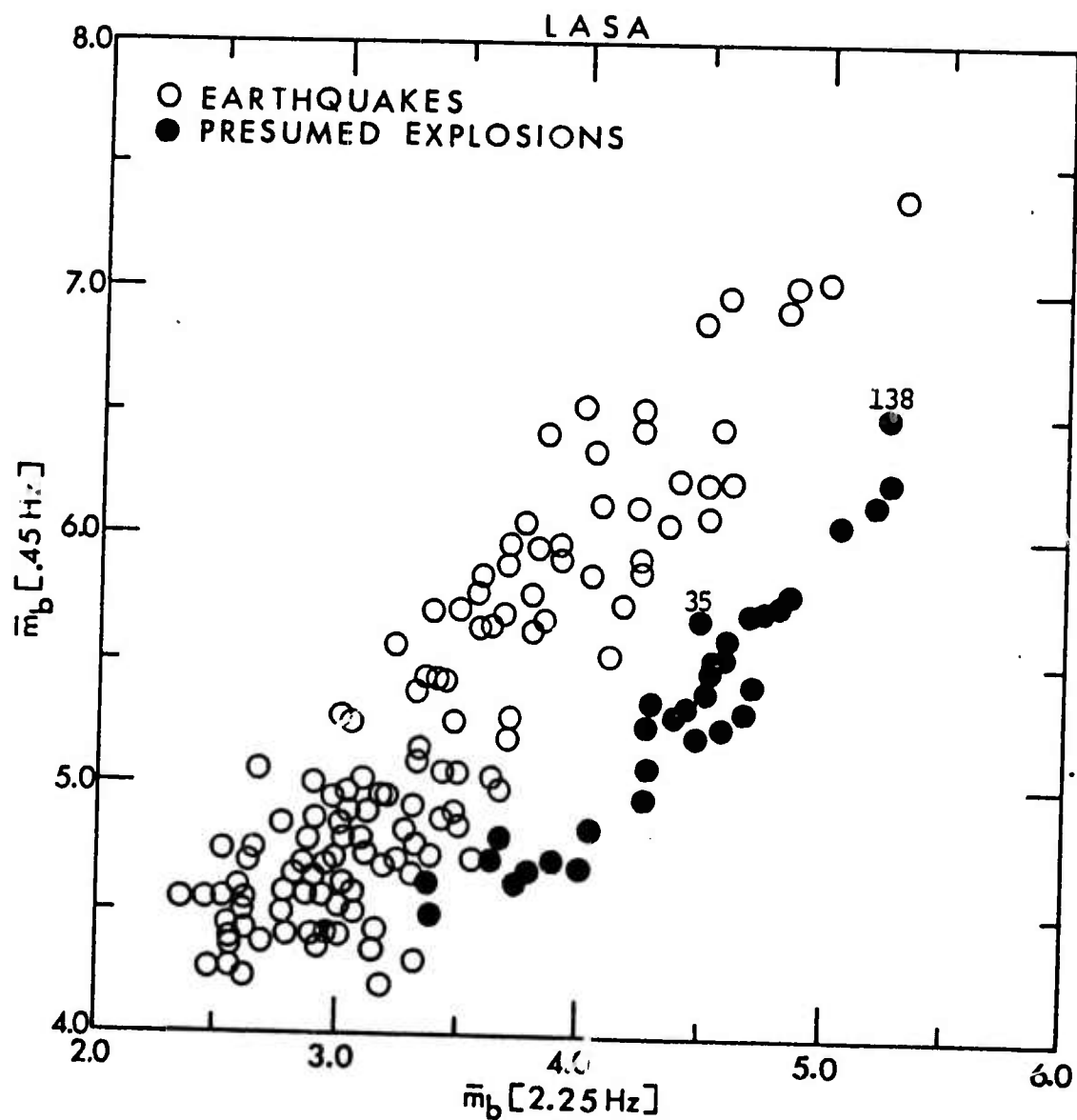


Figure 6.4. Spectral magnitudes, \bar{m}_b , computed at 0.45 Hz and 2.25 Hz. The presumed explosions numbered 35 and 138 occurred at Novaya Zemlya.

earthquake population occurred at Novaya Zemlya. In addition, several of the earthquakes that plot closest to the explosion population occurred along the Kurile-Kamchatka arc or at locations far removed from the explosion epicenters.

A subset of the shallow event ensemble recorded by LASA was also recorded by the limited Oyer array at Norway. The VFM technique was applied to this small subset of events and the results are shown in Figure 6.5. Analogous to the results for LASA, there is discrimination of events over most of the magnitude range except for the smallest magnitude explosion.

The apparent bending of the explosion population into the earthquake population at \bar{m}_b , (2.25) < 3.5 at LASA and \bar{m}_b (5.0) < 4.0 at Norway is mainly the result of microseismic noise enhancing the low frequency \bar{m}_b estimates for the small (signal-to-noise sense) explosions. Correction for this noise at Norway, results in complete separation of earthquakes and explosion populations (Figure 6.6). There was insufficient noise data available for LASA to make similar corrections for noise to that data set.

For a given recording site the limitation of the low frequency end of the seismic bandpass of the VFM discriminant is controlled by the microseismic noise field at that station. At the high frequency end of the seismic bandpass there are three factors that limit the VFM discriminant to small magnitude teleseismic events. These three factors are source spectrum, anelastic attenuation and high frequency background noise.

Extensive study of various VFM discriminant parameters indicates that optimum discrimination would result for spectral magnitudes computed at frequencies (f_c) separated by a decade or more such as observed at Norway. However, noise and anelastic attenuation of the earth combine to constrain

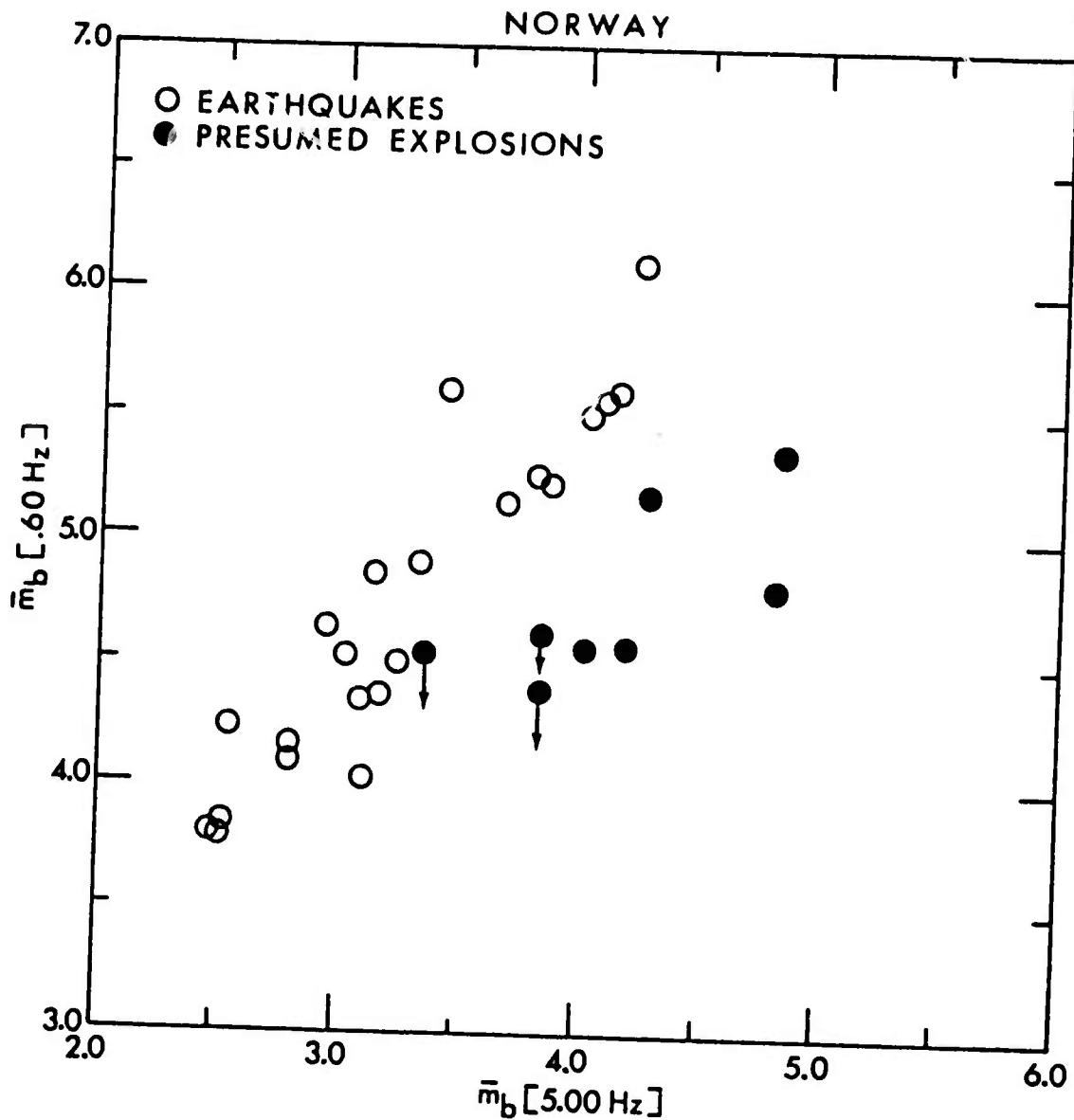


Figure 6.5. Spectral magnitude estimates at $f_c = 0.6 \text{ Hz}$ and $f_c = 5.0 \text{ Hz}$ for an event population recorded at the Oyer array in Norway. The arrows attached to several of the closed circles indicate that the low frequency (0.60 Hz) \bar{m}_b estimates are at the prevailing noise level as determined from recording segments immediately preceding each signal onset.

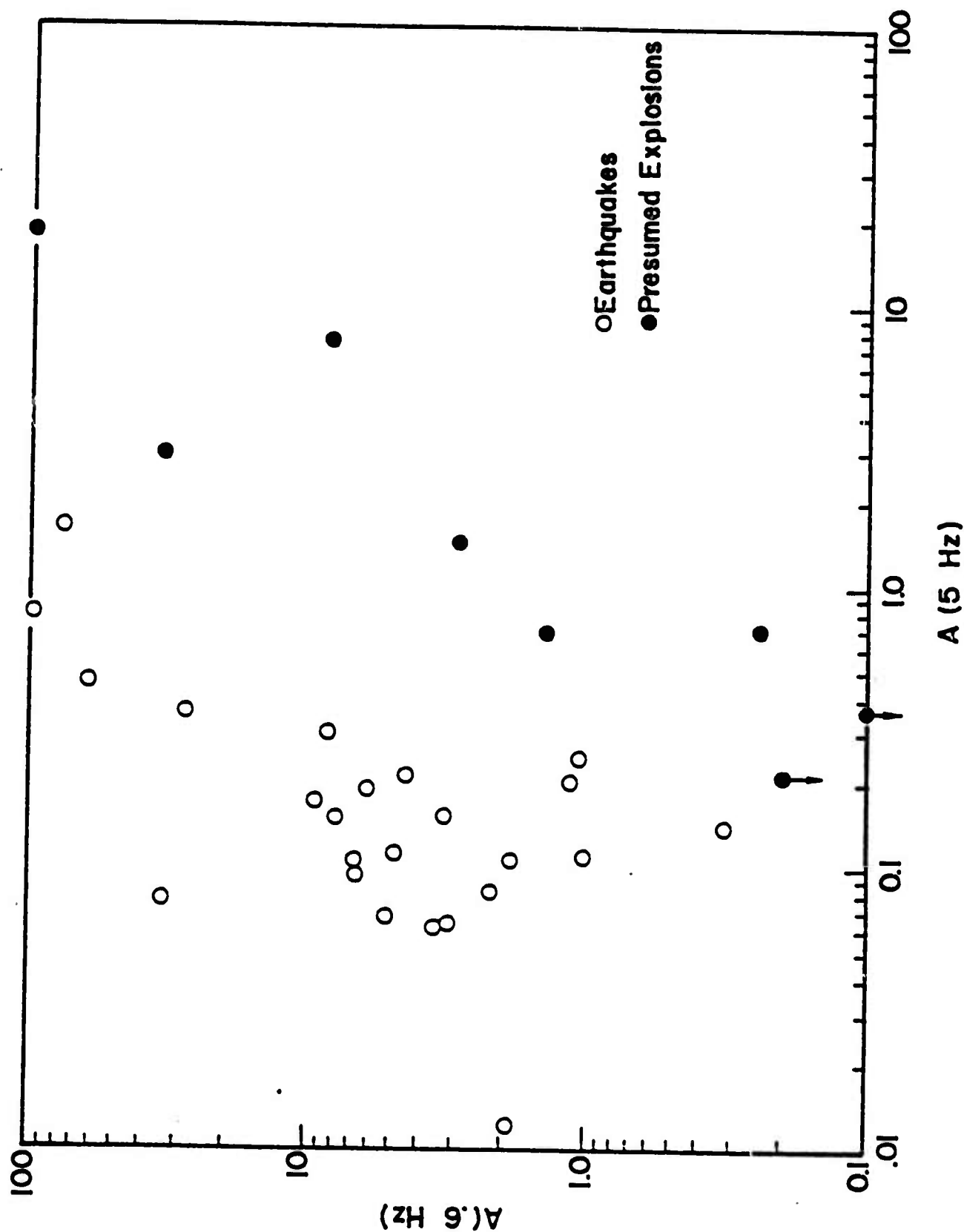


Figure 6.6. Maximum filter amplitudes with noise correction for the same event population plotted in Figure 6.5.

the usable bandwidth of frequencies in the case of LASA data set to approximately one-half a decade.

6.4.2 VFM for Deep Events ($h \geq 70$ km)

At LASA, twenty events in the depth range of 80 km to 580 km were included in the data base and at Norway eleven events with depths greater than 70 km were included. Figures 6.7 and 6.8 show the results of the application of VFM to these data as compared to the results obtained for shallow events (contoured solid and dashed lines).

Deep earthquakes often fail to separate from explosion populations when examined with any of the discriminants, short- and/or long-period, proposed to date. A number of reasons have been proposed for the failure of the discriminants when applied to many deep earthquakes. These include the hypotheses that the deep earthquakes are characterized by impulsive source time functions and/or small source dimensions or that the source-receiver paths are characterized by high Q .

While some of the deep earthquakes overlap into the explosion populations, they are really not as troublesome as they might seem since these events can be identified as naturally occurring earthquakes on the basis of other information (e.g., hypocentral location, using P , pP , and/or sP travel times).

A rather dramatic example of the short-period spectral similarities between an explosion and a deep earthquake is shown in Figure 6.9. Approximately 80 seconds of an unfiltered explosion time series and the output from three narrow-band filters ($f_c = 0.3, 1.0$ and 6.0 Hz) applied to the time series are shown on the left-hand side of the figure. A similar sequence of pictures is shown on the right-hand side for a deep earthquake ($h = 511$ km). Note the

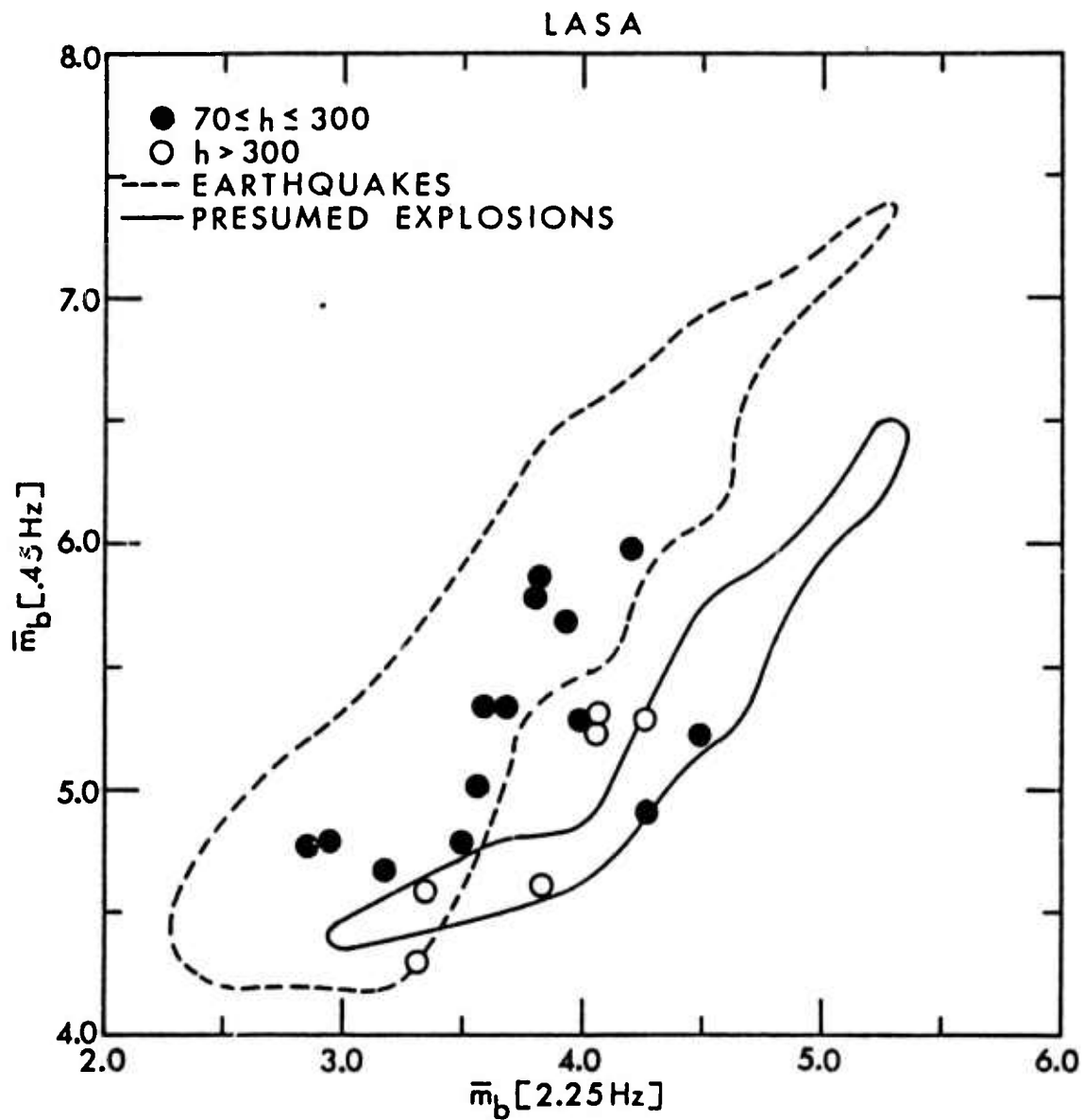


Figure 6.7. Spectral magnitude estimates of deep earthquakes recorded at LASA. The shallow earthquake and explosion populations plotted in Figure 6.4 are contoured in this figure.

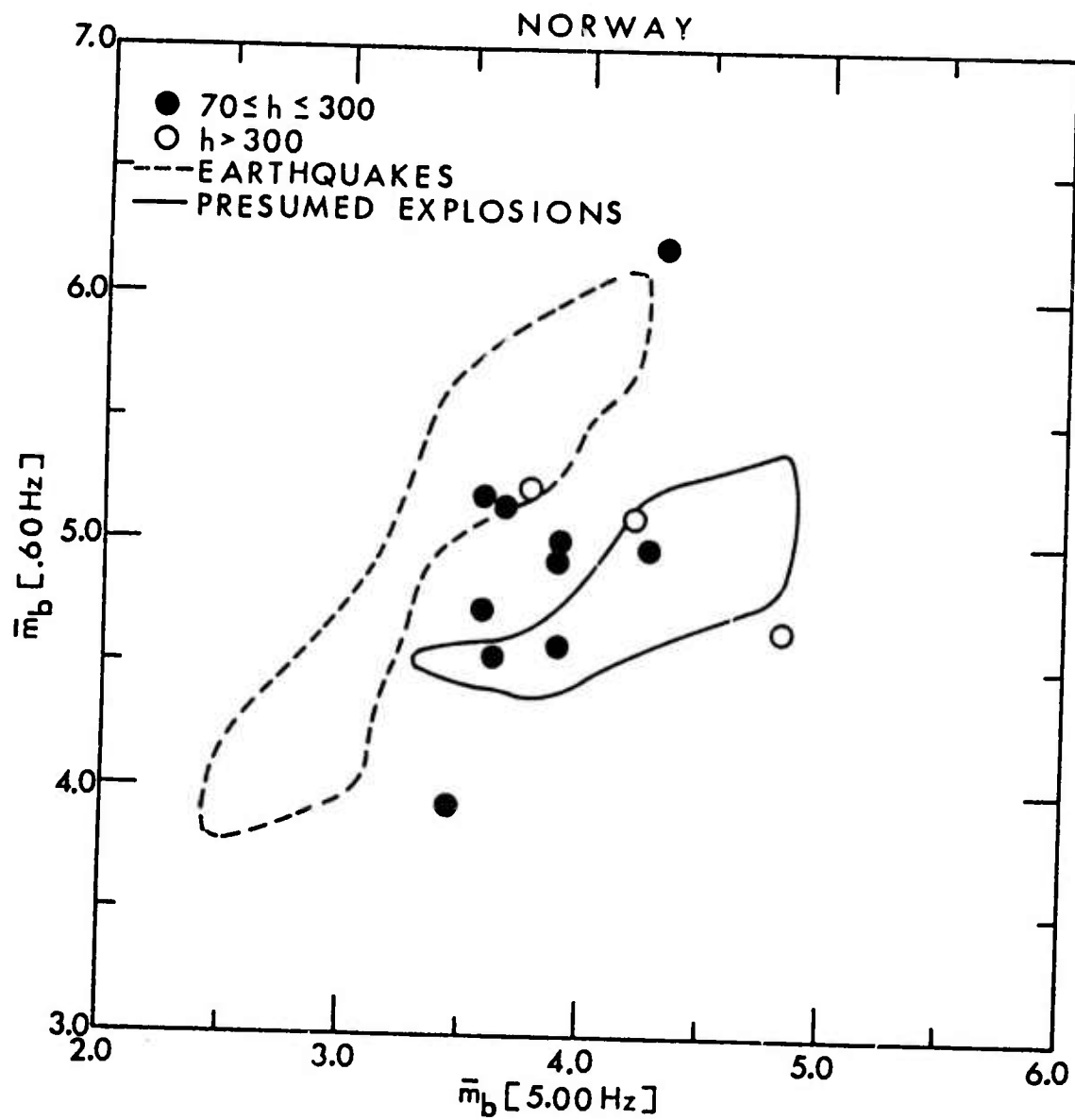


Figure 6.8. Maximum filter amplitudes corrected for noise for deep earthquakes recorded at Norway and compared with the shallow event populations.

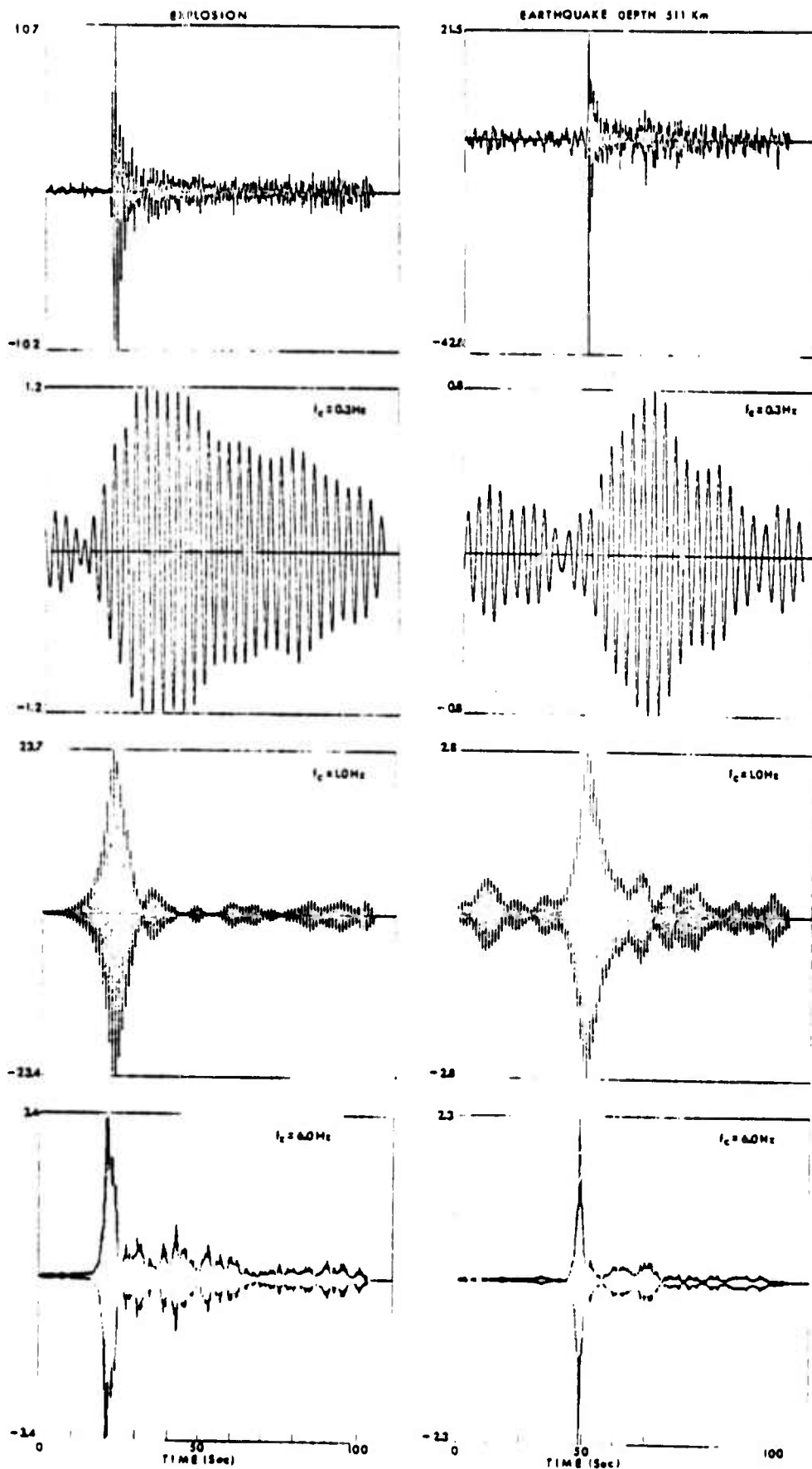


Figure 6.9. Narrow-band filter outputs at three different center frequencies ($f_c = 0.3, 1.0$ and 6.0 Hz) for an explosion (left-hand side) and a deep earthquake (right-hand side).

enhancement of signal-to-noise ratio for the explosion and earthquake signals at the higher frequencies ($f_c \geq 1.0$ Hz).

6.4.3 North American Events Recorded in Canada

Data in digital format for a large population of North American earthquakes and underground explosions recorded at the 19-element short-period Yellowknife array in Canada (Manchee, 1972) were recently acquired. These data consist of vertical-component recordings of P-wave trains (preceded by at least 25 seconds of background noise) from approximately 40 earthquakes occurring in the Gulf of California and 49 underground explosions detonated at the Nevada Test Site (NTS). While signals recorded on all 19 array elements were supplied for most of the events in the data base, our first test for discrimination with the VFM technique was performed on single-element (sensor B5 located at the crossover point of the L-shaped array arms) recordings only.

Each of the time series tested for discrimination in this study was first divided into a noise sample and a signal sample. In the case of the explosions, both noise and signal windows were chosen to be 24 seconds long. For the earthquakes, a 24 second noise window and signal windows up to 66 seconds in duration were examined. The longer duration of the earthquake signal windows was dictated because of the difficulty in identifying the exact signal onset time.

Each of the signal time series was filtered by twenty narrow band filters with center frequencies ranging from 0.25 Hz to 4.0 Hz. The frequency range was selected after examining spectra of ten different earthquakes and explosions. Magnitude estimates, $m_b(f)$, based on a narrow band filter with a relatively low center frequency, f_c , were then plotted versus estimates based on high frequency

filters. This was repeated for various combinations of center frequencies and all of the plots were then examined for discrimination.

Figure 6.10 shows results for the North American data base. The filter center frequencies that have yielded the best discrimination results are, as indicated, 0.425 Hz and 2.5 Hz. In this figure the Gulf of California earthquakes are denoted by the open circles, the NTS explosions by the X's. In general most of the earthquakes on this figure, which are reported in the Preliminary Determination of Epicenters to be shallow focus, separate from the explosion population. While the results in Figure 6.10 are not nearly as impressive in terms of complete separation of event populations (e.g., as in Figure 6.4 for Eurasian events at LASA), a very important and positive point about the discrimination test in Figure 6.10 is the complete separation of the very small magnitude events.

6.5 MULTIPLE EXPLOSION SCENARIO

The VFM technique is especially suited for identification and discrimination of multiple explosion sequences that are designed to appear earthquake-like in terms of the conventional (M_s - m_b , depth of focus, complexity, first motion) discriminants. A multiple event scenario, somewhat similar to one proposed by Kolar and Pruvost (1975), was devised by superposing eight scaled seismograms of a presumed Kazakh explosion recorded at LASA. This explosion signature is shown on the bottom center of Figure 6.11.

The array of explosions and their relative yields were designed to produce earthquake-like seismograms over a wide range of azimuths. The particular array configuration (spacing and firing order) is indicated in the center of the figure. Each seismogram comprising the multiple event was delayed in time relative to the first and scaled in amplitude. The

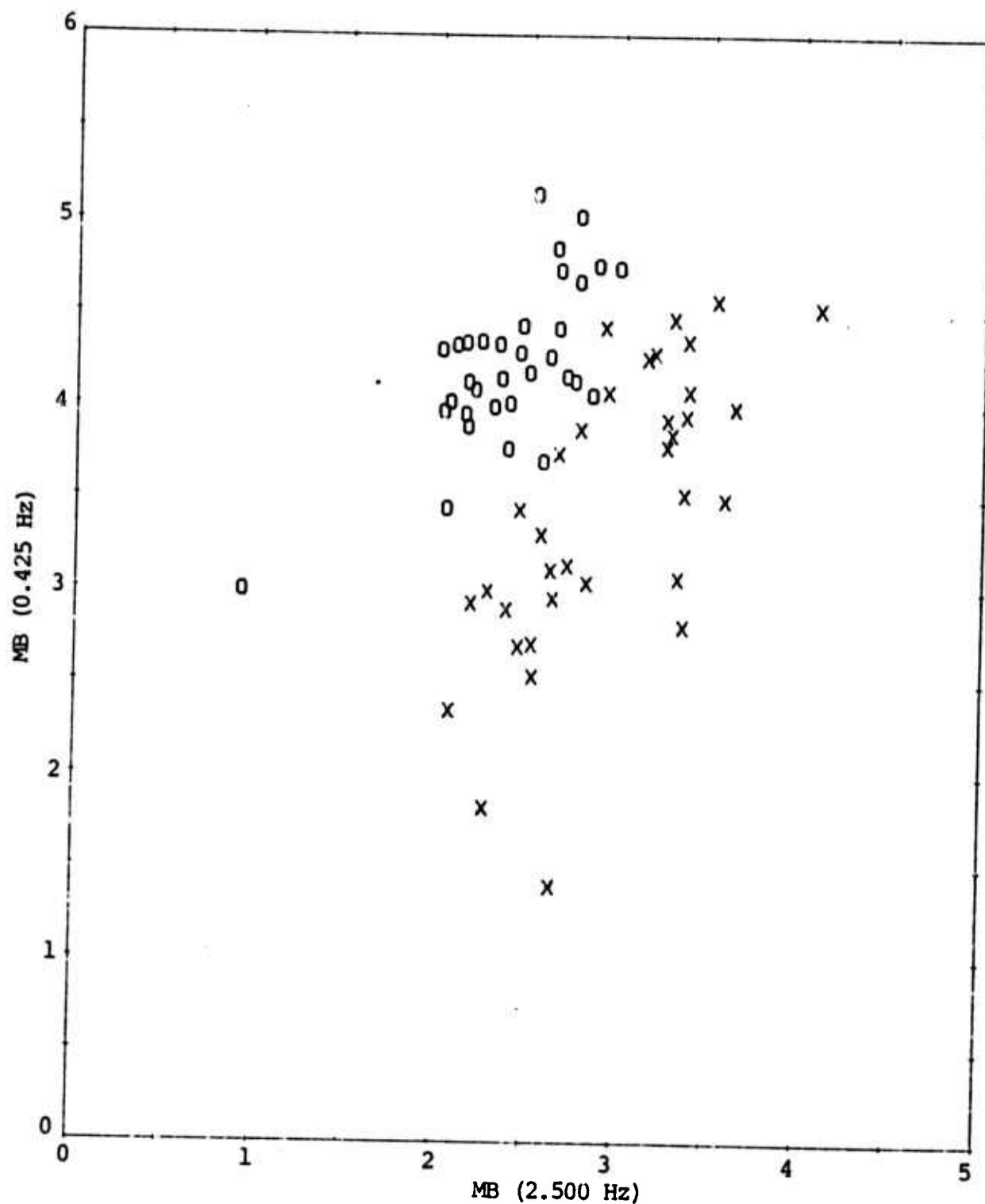


Figure 6.10. Variable frequency magnitude estimates, $m_b(f)$, computed at 0.425 Hz and 2.5 Hz for a population of Gulf of California earthquakes (O's) and NTS explosions (X's).

SIMULATED MULTIPLE EXPLOSIONS

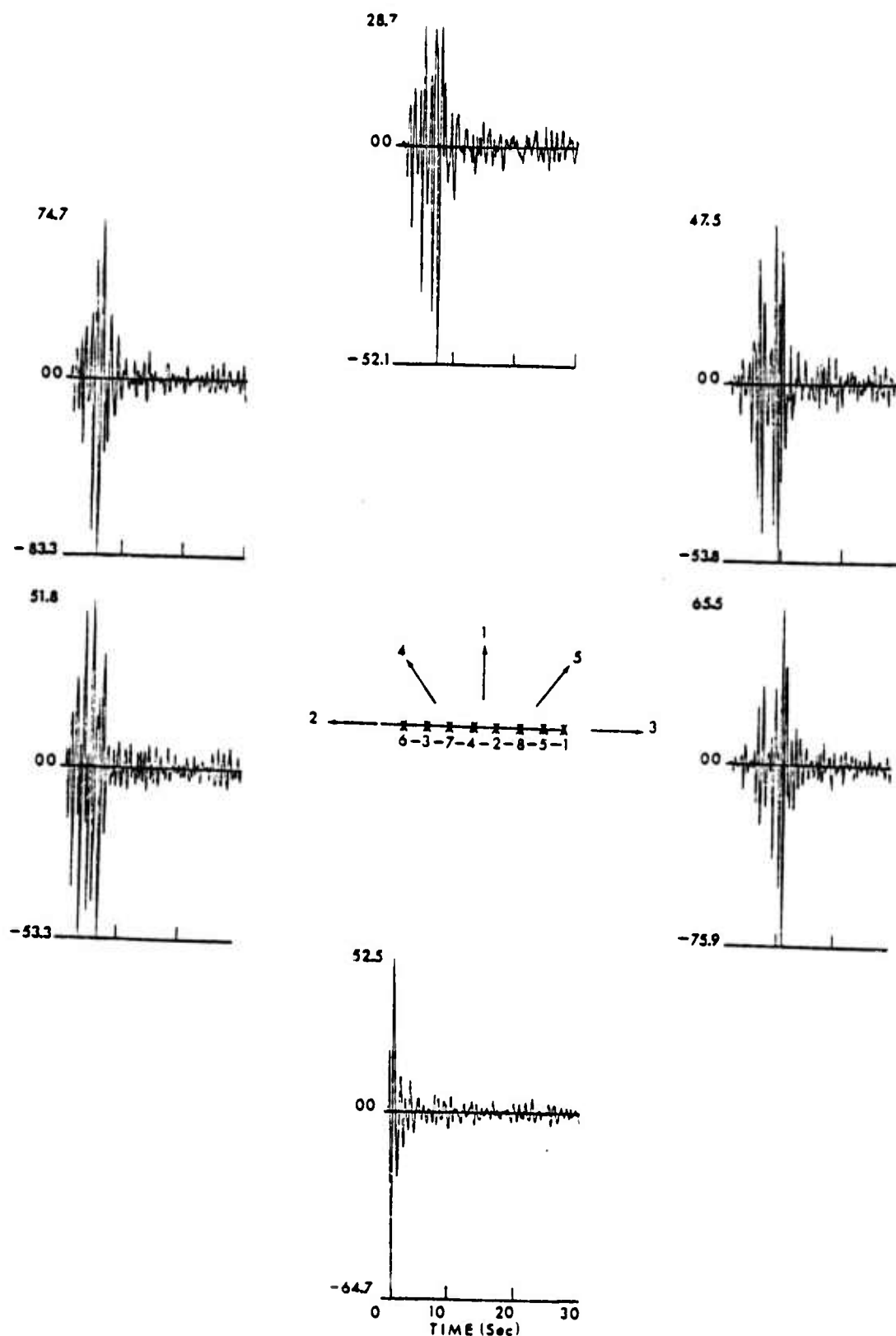


Figure 6.11. Primary explosion signature (bottom-center) used to make composite seismograms at five different azimuths from the array of eight explosions. The firing order and spacing of the explosions are indicated in the center.

explosion delay times between sources are: 0.0, 0.35, 1.2, 2.9, 4.7, 5.7, 6.0 and 6.3 seconds, respectively. The amplitude scaling for all eight explosions is 1, 3.1, 5, 10, 10, 20, 15 and 12.5. The largest explosion in the set is the sixth event and is scaled to give the same ground motion as the primary signal.

The composite seismograms are shown in Figure 6.11 for five different azimuths (1-5) with respect to the shot array. The first point to be noted about these composite seismograms is that with the addition of noise at the beginning of each seismogram, the first motion at azimuths 1, 3 and 5 would most likely be picked as rarefactions. Secondly, the complexity of each composite signal has been significantly increased over that of the primary signal.

Two factors work together to make the multiple event scenario appear earthquake-like on the M_s - m_b basis. First the analyst making amplitude measurements in the conventional manner for the determination of m_b would undoubtedly pick amplitudes corresponding to the earlier smaller explosion in the sequence. On the other hand, the M_s measurements would be based on the superposed surface waves from the three largest explosions occurring later in the sequence. The results would be to reduce the m_b and enhance the M_s estimates and place the composite event in the earthquake population on an M_s - m_b plot.

However, application of the VFM technique results in complete discrimination of the multiple explosion scenario. In Figure 6.12 the VFM estimates determined for the five azimuths are indicated by the X's. A most significant result is that the VFM estimates of the multiple explosion sequence at the five azimuths cluster around the estimates of the primary signal used to form these composite signals (the closed circle immediately to the right of x^1). This means that the VFM technique has based the magnitude

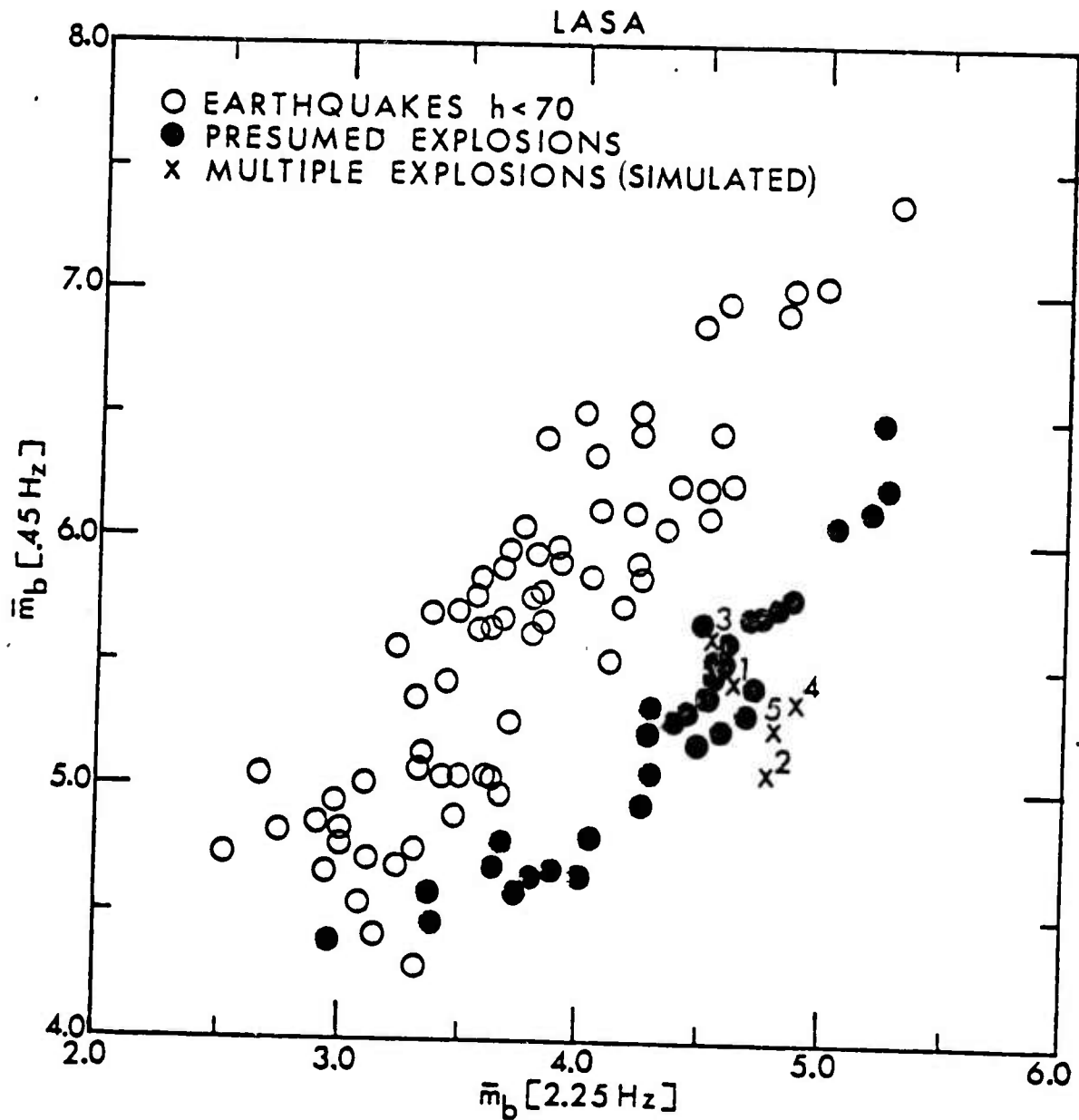


Figure 6.12. Spectral magnitudes for same event population and filter parameters as in Figure 6.4 with estimates for multiple explosions (X's) showing complete discrimination.

estimates on the largest amplitude arrival in the wavetrain, corresponding to the largest yield explosion in the sequence. This is an important result for yield determination of both single and multiple explosions.

6.6 APPLICATION OF VFM TO THEORETICAL SEISMOGRAMS

In this section we compute VFM values for a suite of synthetic earthquake and explosion seismograms. Our purpose in doing this is twofold. First, theoretical seismograms provide a controlled data set for testing and improving a data analysis technique, such as the VFM. With theoretical seismograms the controlling parameters and their effect are thoroughly understood. Second, we want to compare the theoretical VFM values to the observed values to see how well our theoretical seismograms match actual data with regard to this spectral measure.

This section is divided into four parts. We first briefly describe the computation of the synthetic seismograms used in the study. Then the VFM estimates are computed, first for explosions, then for earthquakes. Finally, the theoretical VFM values are compared to those from observations.

6.6.1 Calculation of Synthetic Seismograms

The techniques used to compute short period body wave theoretical seismograms have been developed under this contract and have been described in previous semi-annual reports (Bache, et al., 1974, 1975; Savino, et al., 1975). The technique is outlined in Chapter IV of this report and a number of examples are given there. Here we shall rely upon the discussion in Chapter IV and simply point out features peculiar to the synthetic seismograms for the VFM study.

Synthetic seismograms were computed for five different events which are intended to be typical of NTS. The

characteristics of these five events are summarized in Table 6.1.

Table 6.1. Characteristics of Explosion Events for Synthetic Seismograms

<u>Event</u>	<u>Test Area</u>	<u>Source (#)</u>	<u>Yield (kt)</u>	<u>Burial Depth (km)</u>
1	Yucca Flat	Dry Tuff (134)	10	0.35
2	Pahute Mesa	Dry Tuff (134)	50	0.42
3	Pahute Mesa	Wet Tuff (131)	400	0.875
4	Pahute Mesa	Rhyolite (125)	1000	1.20
5	Pahute Mesa	Rhyolite (125)	1500	1.35

The coupling of explosion energy into elastic waves varies with the characteristics of the material type. In our computations the equivalent elastic source is specified by a reduced displacement potential which is computed using finite difference methods. The procedure for computing the source has been described by Cherry, et al. (1974). The sources 134, 131 and 125 were computed for NTS dry tuff, wet tuff and rhyolite, respectively, and are discussed by Bache, et al. (1975).

For the synthetic seismogram calculations two source region crustal structures were used, one for Pahute Mesa and one for Yucca Flat. These are tabulated in Tables 6.2 and 6.3.

Except for the source specification in terms of a reduced displacement potential and the velocity profile in the source region, the synthetic seismogram calculations are identical to those for earthquakes described in Chapter IV. Once again, the upper mantle model is HWNE (Helmberger

Table 6.2. Yucca Flat Crust for Theoretical Seismograms

<u>Layer</u>	<u>Depth (km)</u>	<u>Thickness (km)</u>	<u>P Wave Velocity (km/sec)</u>	<u>S Wave Velocity (km/sec)</u>	<u>Density (gm/cm³)</u>
1	0.3	0.3	1.585	0.9	1.65
2	0.375	0.075	2.286	1.212	1.73
3	0.6	0.225	2.13	0.99	1.7
4	0.955	0.325	2.5	1.43	1.9
5	1.175	0.25	4.4	2.75	2.2
6	2.3	1.125	5.0	3.1	2.4
7	4.3	2.0	5.5	3.2	2.6
8	20.0	15.7	6.0	3.5	2.8

Table 6.3. Pahute Mesa Crust for Theoretical Seismograms

<u>Layer</u>	<u>Depth</u>	<u>Thickness</u>	<u>P Wave Velocity</u>	<u>S Wave Velocity</u>	<u>Density</u>	<u>Material</u>
1	0.256	0.256	2.74	1.3	2.0	
2	0.36	0.104	3.6	1.9	2.3	
3	0.65	0.29	2.13	1.1	2.1	Dry Tuff
4	0.8	0.15	2.5	1.56	1.85	Wet Tuff
5	1.4	0.6	4.2	2.62	2.4	Wet Rhyolite
6	2.1	0.7	4.3	2.4	2.6	Wet Rhyolite
7	6.0	3.9	4.7	2.6	2.6	
8	12.0	6.0	5.4	2.7	2.7	
9	20.0	8.0	6.0	3.5	2.8	

and Wiggins, 1971) and an average continental crust (Table 4.2) is used at the receiver. The T/Q is 1.05, a value found to be appropriate for NTS northeast profiles.

At a single epicentral distance seismograms for events 1 - 5 of Table 6.1 will illustrate the effect of variations in the source function (reduced displacement potential), the yield and the burial depth or P-pP lag time. We also would like to see the effect of differences in the upper mantle travel path so seismograms were computed for two distances; 3735 and 2360 km. The synthetic seismograms are shown in Figure 6.13. At 3735 km the upper mantle response is beyond the triplication range and the seismograms are quite simple. The response at 2360 km is within the triplication range and the seismograms are considerably more complex.

The computation of synthetic seismograms for earthquakes using the Archambeau/Minster source model was described in detail in Chapter IV. In that chapter the scaling of seismogram amplitudes with the source parameters is discussed. Using these techniques and precisely the same earth models used for the seismograms of Chapter IV, a suite of theoretical seismograms were computed in which the parameters varied include the depth of focus, the fault length, the fault orientation and the epicentral distance. We also should mention that the form of the Archambeau/Minster source used for these calculations is not identical to that of Chapter IV, but that the spherical volume of vanishing rigidity both expands and propagates (in the model used in Chapter IV the spherical volume expands from a fixed point on the diameter). For our purposes the differences between the models are quite small and the scaling behavior described in Chapter IV is valid for both. The material properties, rupture velocity, etc., are the same as for the earthquakes of Chapter IV.

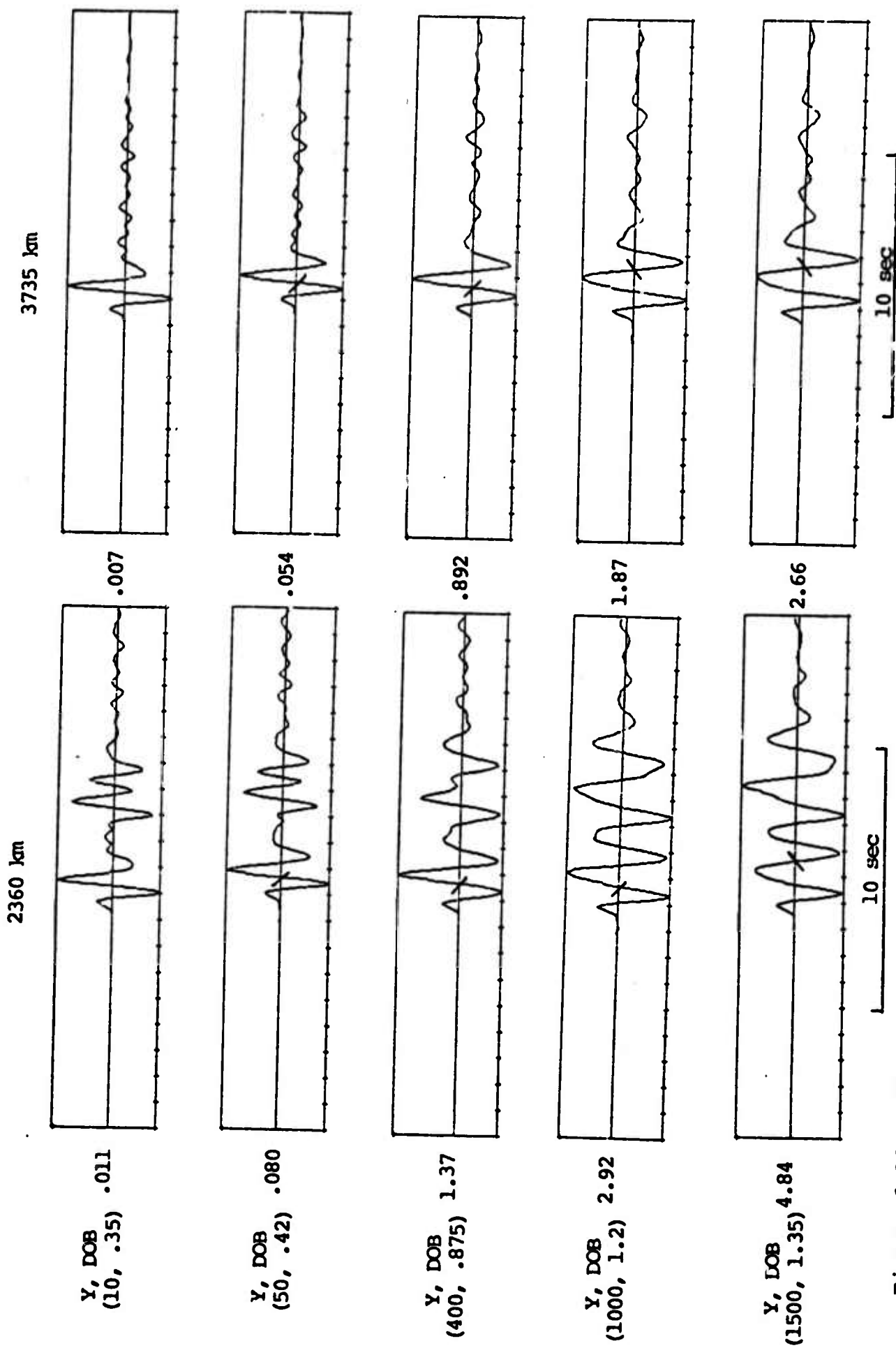


Figure 6.13. Theoretical seismograms for NTS events at two epicentral distances. The event yield (kt) and DOB (km) is indicated on the left. Given with seismogram is the maximum peak-to-peak amplitude in microns at 1 Hz. The instrument response is specified by the LRSM nominal response curves.

As in Chapter IV we compute synthetic seismograms for the five focal depths 10, 15, 25, 35 and 45 km. Earthquake sources were computed at three different fault lengths. In the material at 35 - 45 km depth these lengths were 10, 5 and 2.5 km. Then according to the scaling properties of the model discussed in Section 4.2, the fault lengths are 8.4, 4.2, 2.1 km at 25 km depth and 7.6, 3.8 and 1.9 km at the 10 and 15 km depths. All seismograms were scaled to a 100 bar stress drop.

In Figures 6.14 and 6.15 we show typical examples of the synthetic seismograms for this VFM study. The only difference between the seismograms of Figures 6.14 and 6.15 is in the upper mantle response which in one case is for a range of 2500 km, within the triplications, and for the other case is for a range of 4000 km. The source orientation is right-lateral strike-slip and the azimuth is 30° counterclockwise from the strike (see Figure 4.2). As for the explosions, the seismograms at the nearer range are considerably more complicated.

Seismograms for the three basic sources described above were also computed for two other source orientations in addition to the strike-slip. These orientations are dip-slip and 45° thrust. For both, the rupture initiates at the origin and breaks downward. For the dip-slip events the fault plane shown in Figure 4.2 is rotated 90° about the Y_G -axis. That is, the material on the $+Y_G$ side of the $X_G - Z_G$ plane is downthrown. For the thrust events the dip-slip fault plane is rotated 45° clockwise about X_G . Then the hanging wall slides upward over the footwall.

6.6.2 VFM Values for Synthetic Explosion Seismograms

For the synthetic seismograms shown in Figure 6.13, VFM values were computed at a number of frequencies. For

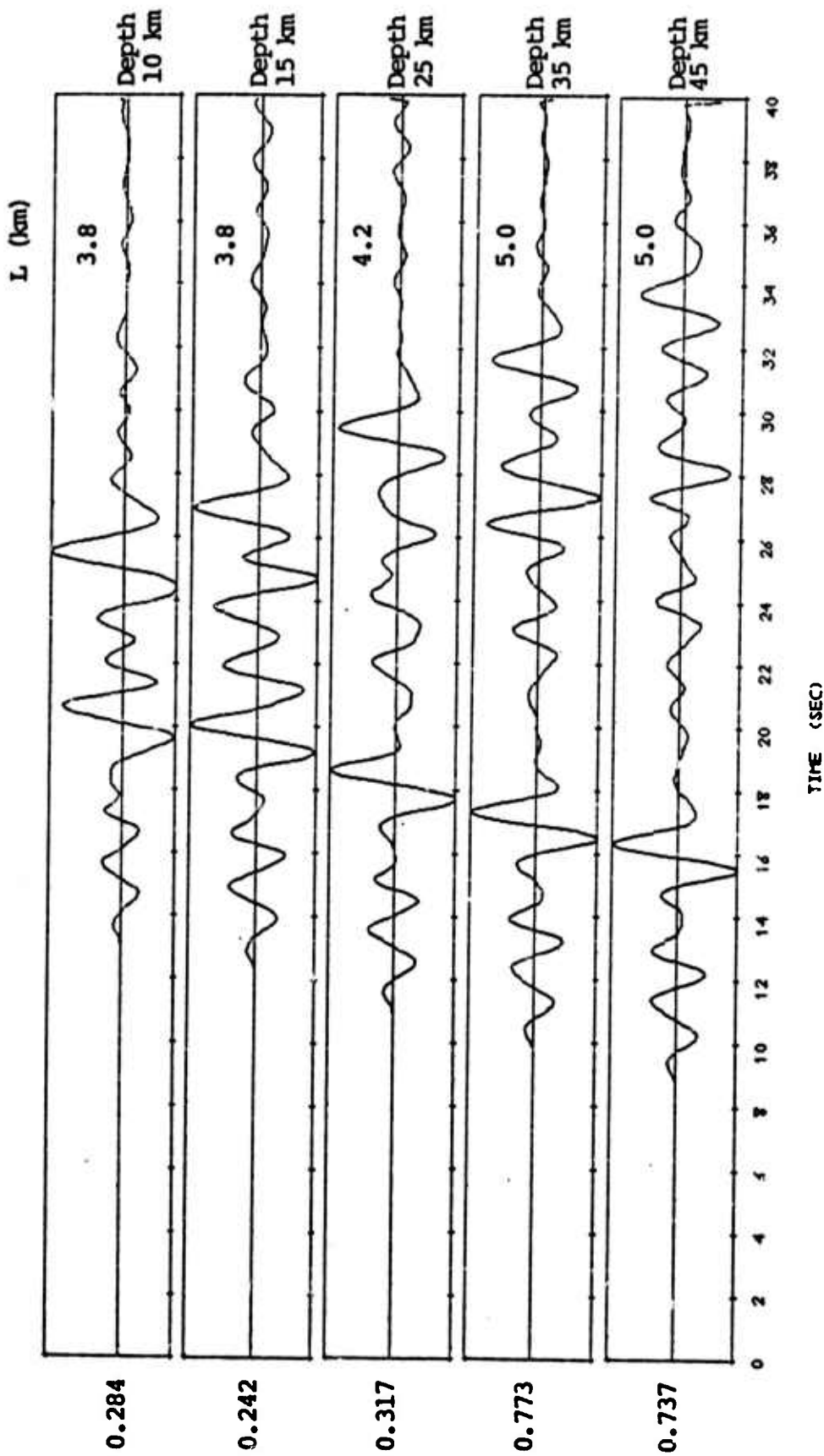


Figure 6.14. Theoretical seismograms for a right-lateral strike-slip event at an epicentral distance of ≈ 2500 km and an azimuth 30° counterclockwise from the strike. The fault length is indicated and the stress drop is 100 bars. At the left is the maximum peak-to-peak amplitude in microns at 1.0 Hz.

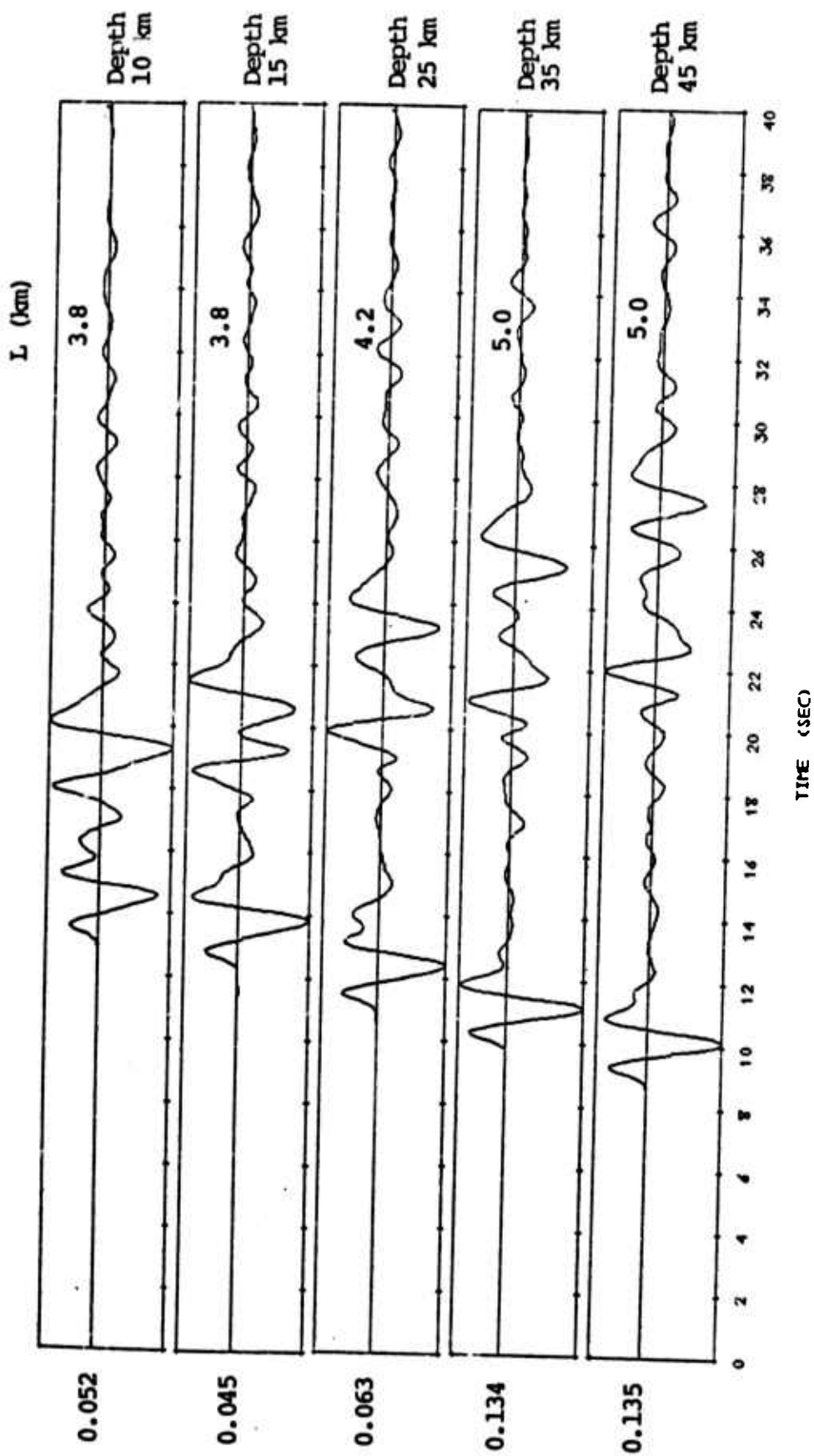


Figure 6.15. Theoretical seismograms identical to those of Figure 6.14 except that the upper mantle response is now appropriate to a distance of 4000 km.

these events we plot \bar{m}_b (0.45 Hz) versus \bar{m}_b (2.25 Hz) in Figure 6.16.

Recall that the events for which the synthetic seismograms were computed varied in emplacement material, depth of burial and yield. Also, seismograms were computed at two epicentral distances. The effect of the distance variation is clear and consistent with the $\Delta\bar{m}_b(f)$ about the same for every event. The lower frequency $\bar{m}_b(f)$ values are much less affected by the introduction of the upper mantle triplications.

The variation of the $\bar{m}_b(f)$ values with the source parameters is strongly dependent on frequency. As one might expect, the low frequency values (\bar{m}_b (0.45 Hz)) are proportional to the yield.* The high frequency values on the other hand seem to be almost independent of yield. This is because the high frequency (2.25 Hz) is beyond the corner frequency for these events.

6.6.3 VFM Values for Synthetic Earthquake Seismograms

For the earthquake synthetic seismograms the parameters varied include the focal depth, fault length, fault orientation and epicentral distance. The stress drop is held constant and the other fault parameters obey the similarity rules set forth in Chapter IV.

First, let us examine the effect of fault orientation on the VFM estimates. The basic event is that which has a

* Actually the proportionality is to the product of the local P wave velocity and the amplitude of the reduced velocity potential at the dominant frequency as is shown by Bache, et al. (1975). The source function amplitude is, of course, strongly dependent on the explosion yield.

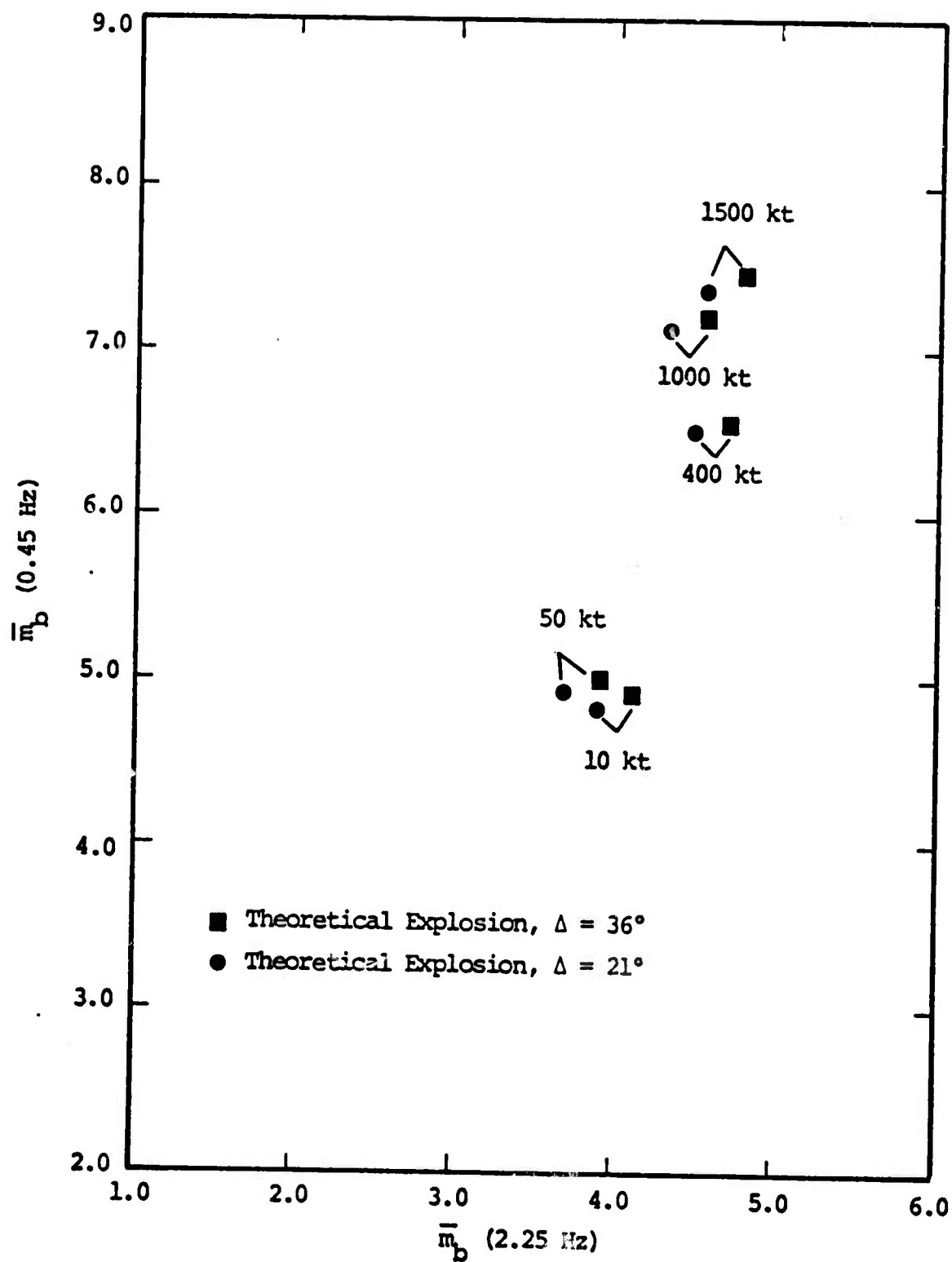


Figure 6.16. Theoretical NTS explosion VFM estimates for two distances (21° , 36°).

fault length of 5.0 km at the 45 km depth. The $\bar{m}_b(f)$ were computed from synthetic seismograms at a single azimuth (30°) and distance (4000 km). For the strike-slip orientation the seismograms were shown in Figure 6.14.

In Figure 6.17 we plot $\bar{m}_b(0.45)$ versus $\bar{m}_b(2.25)$ for the fifteen synthetic seismograms. In terms of our discussion of the scaling of teleseismic body wave amplitudes in Section 4.6, all these events have the same "source strength". Then the simple scaling relationship (4.13) indicates that, fixing the radiation pattern factor, the amplitude should scale with α^4 or L^4 since L/α is fixed. Except for the strike-slip orientation we see that the VFM values are poorly explained by this scaling. This is apparently because the radiation pattern factor is strongly varying from record-to-record, even for a fixed fault orientation.

In Figure 6.18 we plot the VFM values for the three different source strength events under study. Once again we show the values for all five focal depths. The source orientation is strike-slip and the azimuth and distance are again 30° and 4000 km. Within each group the variation with depth (and length) is about the same but the major change is due to the change in source strength.

Finally, in Figure 6.19 we select one of the sources, the strike-slip earthquake with $L = 5.0, 4.2, 3.8$ km, and show the effect of changing epicentral distance. That is, the seismograms are those of Figures 6.14 and 6.15. As with the explosions, we see that the effect of the upper mantle response variation is quite consistent from event to event.

In summary, we have seen that the variation of VFM with the source parameters is quite complex and not easily explained with simple scaling relationships. The data for superficially similar events scatters over a range of more than 0.5 VFM units at both high and low frequencies. In the

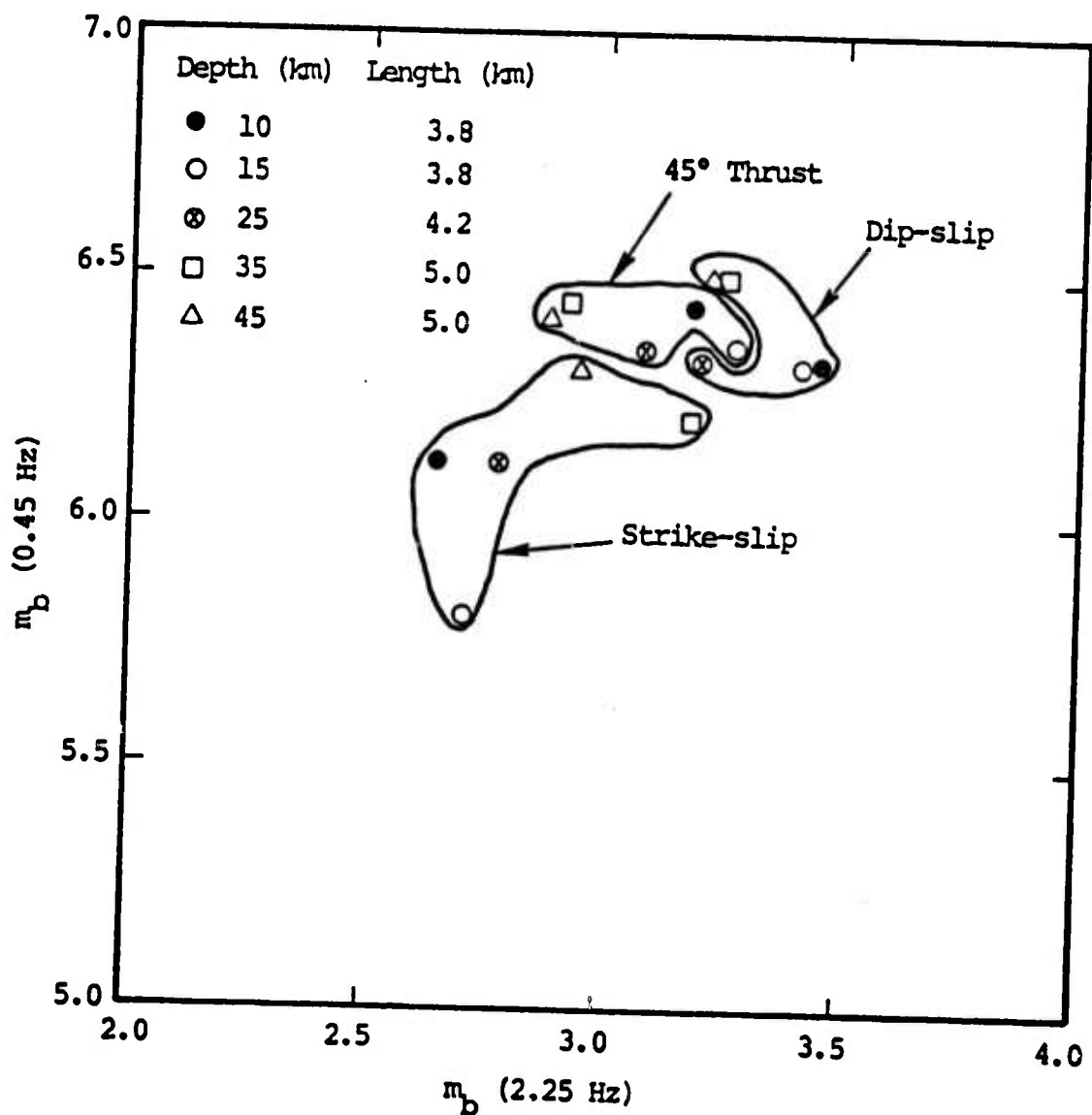


Figure 6.17. Plot of VFM for five events at three different fault orientations. The distance and azimuth are 4000 km and 30° for all seismograms.

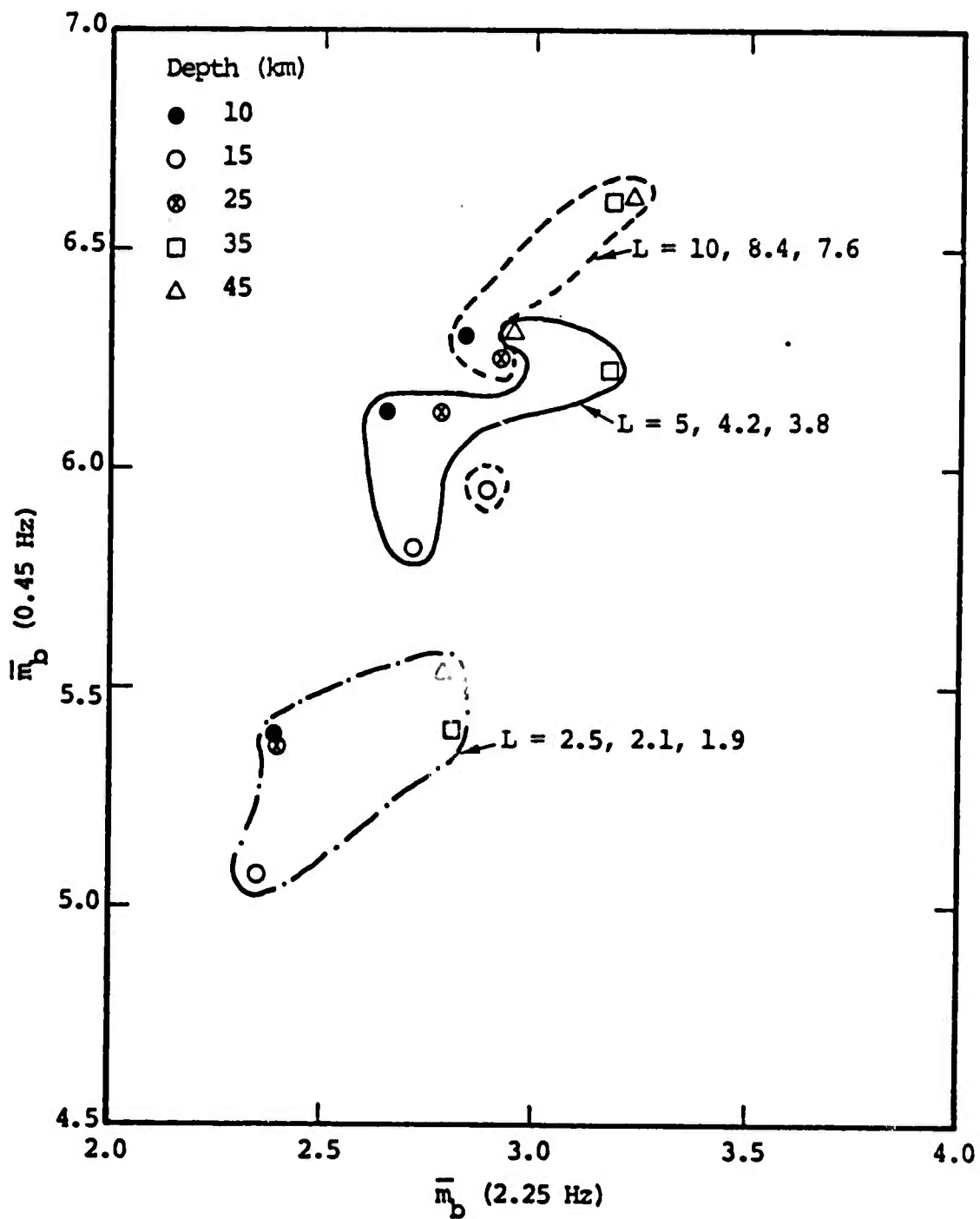


Figure 6.18. Theoretical VFM estimates for three strike-slip earthquakes.

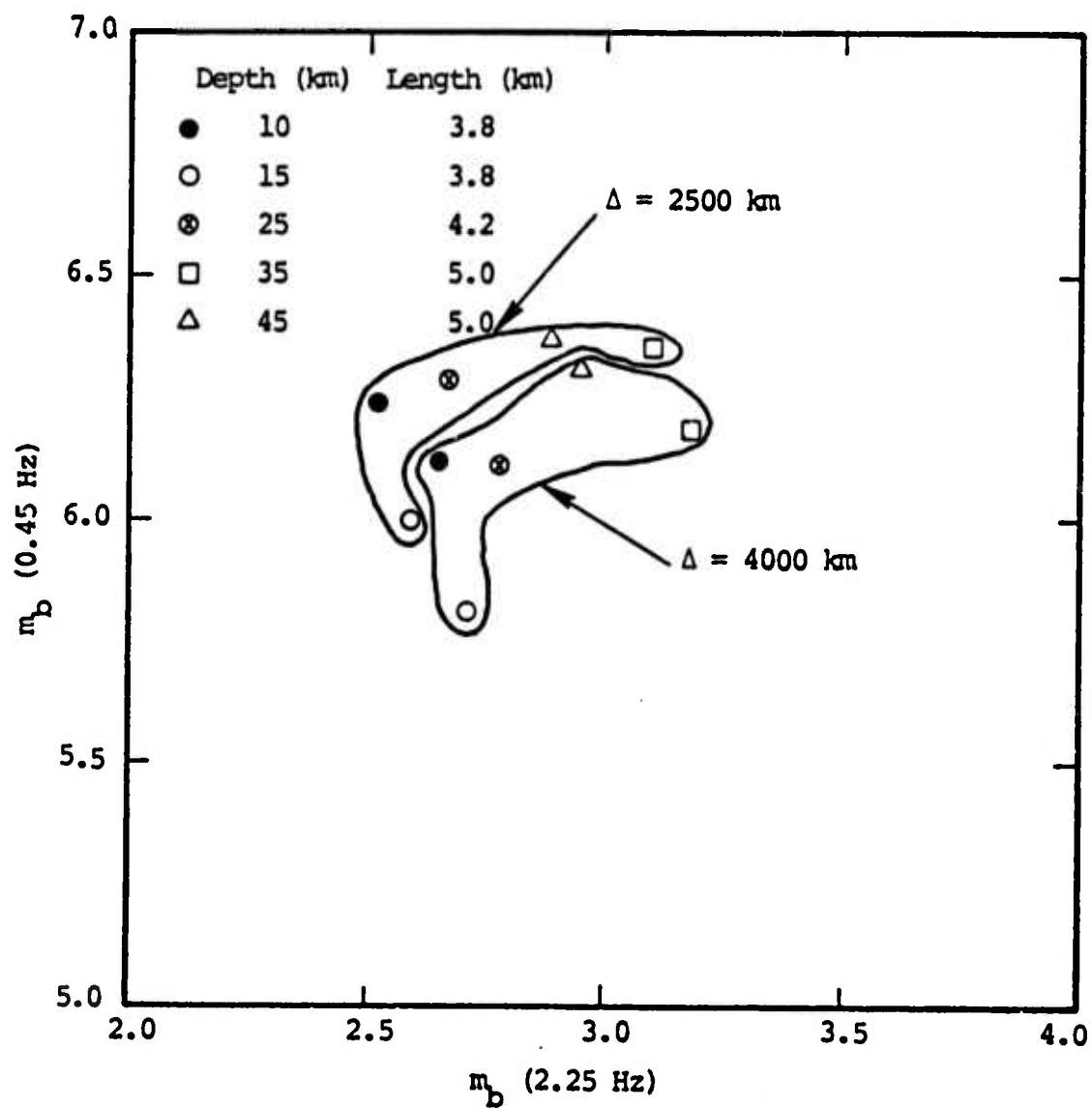


Figure 6.19. Theoretical VFM estimates for the seismograms of Figures 6.14 and 6.15.

next section we consider the data in a global sense and see how well the trends of our theoretical estimates agree with observations.

6.7 COMPARISON OF SYNTHETIC TO OBSERVED VFM DATA

This section presents a comparison of theoretical explosion and earthquake VFM estimates to selected observed VFM data discussed previously (see Section 6.4). The observed data from explosions includes NTS explosions recorded at YKA (Figure 6.10). Observed earthquake VFM data are from the Gulf of California and recorded at YKA (Figure 6.10).

6.7.1 Comparison of Explosion VFM Data

In Figure 6.20 we show the theoretical explosion data discussed in the previous section plotted with the observed NTS explosion data recorded at YKA. The distance range for the observed YKA data is 25.2° to 25.4° versus the distance range of 21° to 36° for the theoretical data. The agreement between the observed and synthetic explosion populations in terms of absolute magnitude estimates and trend is quite good. For instance, three of the largest observed explosions were in the 150 to 200 kt yield range while ten had reported yields of 10 kt or less. The majority of the remaining events were in the 50 to 100 kt yield range. Further, note that the noise corrections applied to the observed data set were particularly significant for the lower yield bombs. In general these corrections resulted in a reduction of the VFM estimates which accounts, in part, for the very low magnitude estimates in Figure 6.20.

In the previous section of this report we showed that there is a strong dependence of the explosion VFM estimates on depth-of-burial and near source material properties. In view of the fact that the explosion population in Figure 6.20 includes events from several different test areas at NTS (i.e., Pahute Mesa, Yucca Valley, Rainier Mesa), the

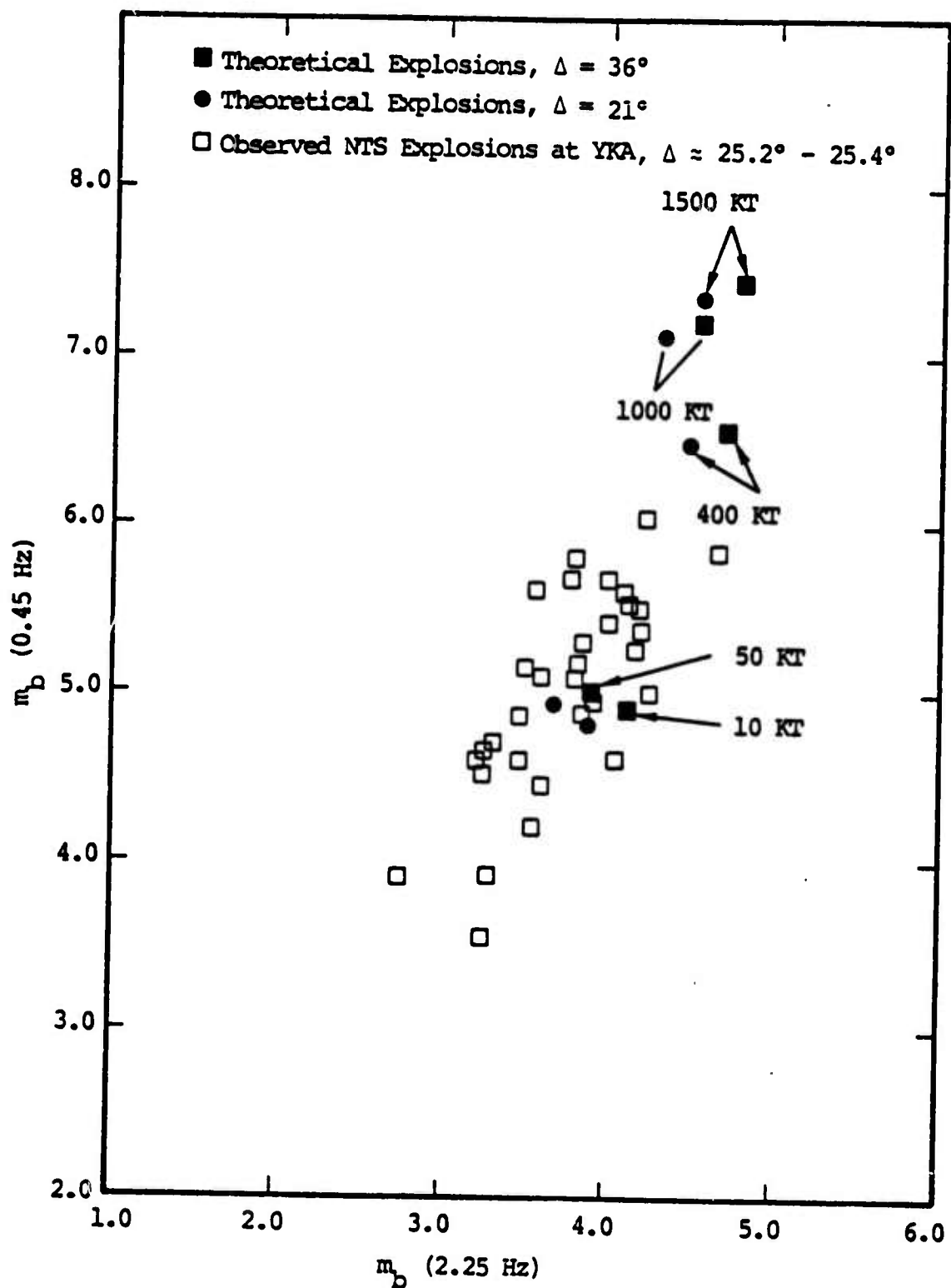


Figure 6.20. Comparison of theoretical to observed explosion (NTS-YKA) VFM estimates.

amount of scatter of the observed data is not really surprising. The scatter could undoubtedly be reduced by segregating the explosions according to the specific test areas and comparing with appropriate synthetic events. However, our intent here was to approximate the gross features of the observed data; an objective which is obviously fulfilled in Figure 6.20.

6.7.2 Comparison of Earthquake VFM Data

The theoretical VFM estimates for the strike-slip earthquakes (0° , 90° , 0°) at a distance of 36° shown in Figure 6.18 for three fault sizes (10×8.4 km, 5×4.2 km and 2.5×2.1 km) and five depths (10, 15, 25, 35 and 45 km) are plotted in Figure 6.21 along with the Gulf of California VFM data. The average distance of YKA from the Gulf of California is approximately 37° versus 36° for the theoretical data. The theoretical values are positioned within the left portion of the Gulf of California values.

The scatter of the observed data is large. Thatcher and Brune (1971) indicate that characteristically these earthquakes are very shallow and are predominantly normal faults. Had we used dip-slip earthquakes (0° , 90° , 90°) theoretical VFM values instead of the strike-slip type, the theoretical population would be positioned near the center of the observed data. The theoretical results shown previously in Figure 6.17 confirm this statement. However, much more must be learned about the fault mechanisms, stress-drops and depths of these Gulf of California earthquakes to explain the large variance observed in the VFM estimates.

6.7.3 Comparison of Explosion-Earthquake VFM Data

Figure 6.22 presents an overview of the important data included in this report. In this figure the theoretical VFM

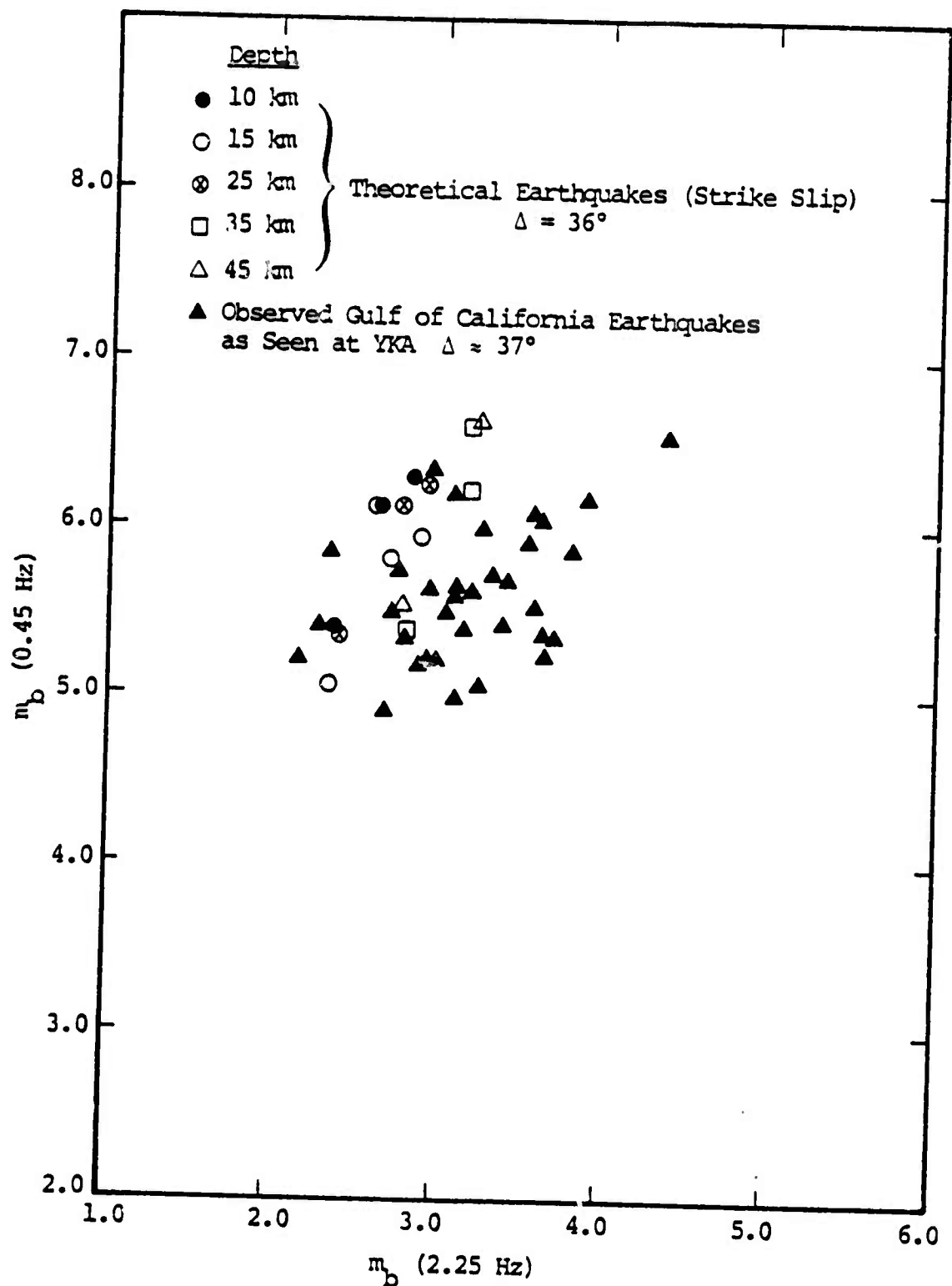


Figure 6.21. Comparison of theoretical strike-slip earthquakes to observed earthquake (Gulf of California-YKA) VFM estimates.

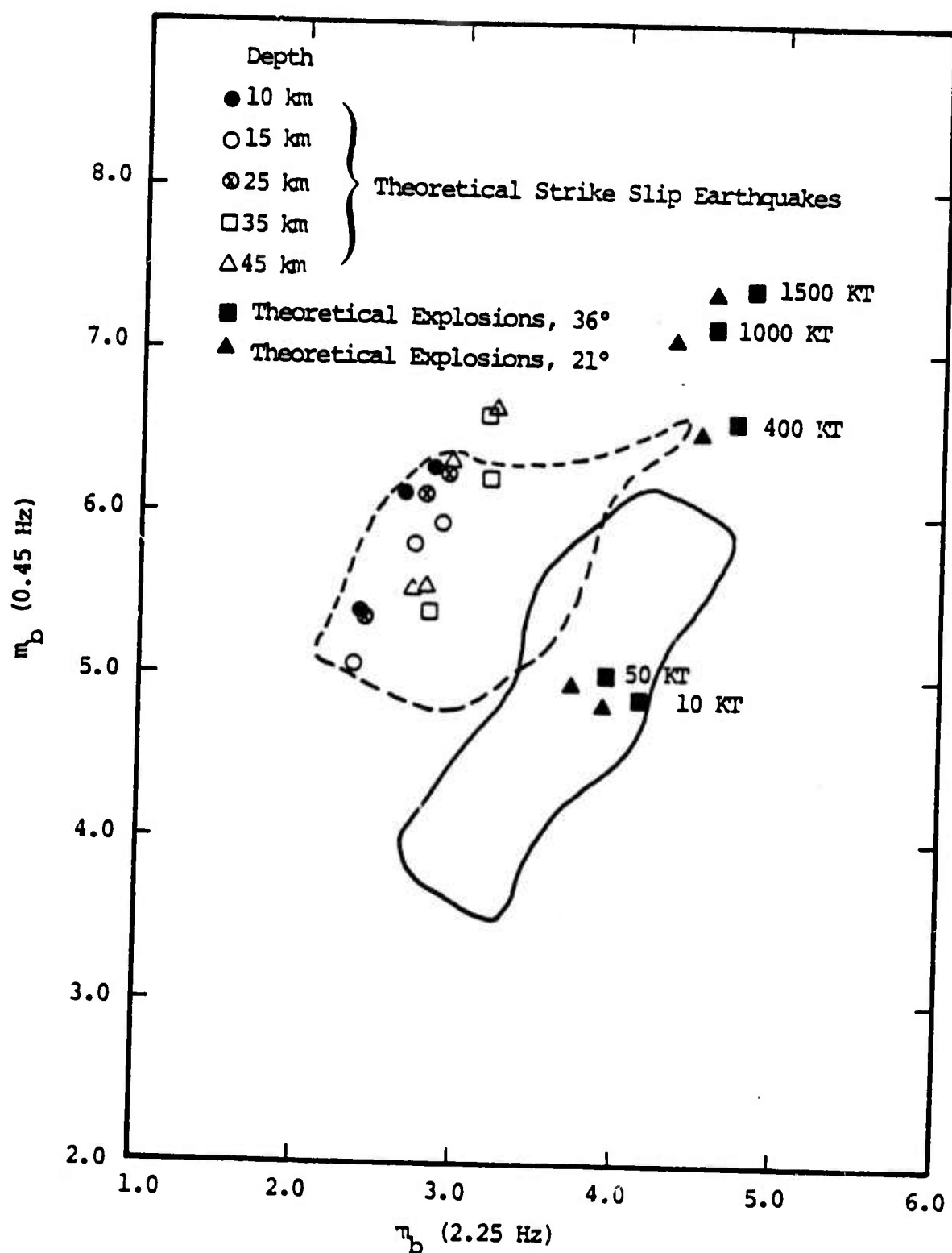


Figure 6.22. Comparison of theoretical and observed explosion and earthquake VFM estimates.

data for explosions and strike-slip earthquakes are plotted corresponding to an epicentral distance of 4000 kms. In addition we outline the Gulf of California population (broken line) and the NTS explosion (solid line) as observed at YKA. We previously indicated that had we used theoretical dip-slip earthquakes the VFM estimates would lie near the center of the observed Gulf of California VFM data. Further, the observed NTS-YKA data occurs at about 25.3° distance and plotting the theoretical values at a distance of 21° on the figure (solid triangles) indicates that they too lie near the center of the observed explosion population. Hence, the mean separation between earthquakes and explosions populations of both theoretical and observed groups is approximately the same (≈ 0.8 units of magnitude normal to the population trend lines).

6.8 SUMMARY AND CONCLUSIONS

Application of the variable frequency magnitude (VFM) discriminant to North American and Eurasian event populations yields complete separation between earthquakes and explosions down to conventional magnitudes, m_b , in the range of 4.0 to 4.5. Enhancement of this discriminant can be achieved by regionalization of the event populations and the application of noise corrections to the VFM values. Obviously, the latter process becomes most important for small events.

Application of the VFM discriminant to a multiple explosion scenario yielded VFM values similar to those of single explosions for five azimuths sampled around the linear array of explosions. All VFM values clustered around that of the primary signal employed and correspond to the largest yield explosion in the sequence.

Estimation of the VFM values for theoretical explosions and earthquakes originating in the same source region

and observed at similar epicentral distances indicate the following:

- Explosion VFM exhibit a strong dependence on depth-of-burial and near source material properties.
- For equal sized earthquakes of various orientations the most significant variation in the VFM estimates is associated with focal depth. Observations of similar fault orientations of varying size shows that depth changes result in nonuniform variations in the VFM estimates.

Comparison of VFM values for theoretical and observed explosions and earthquakes where Q's and distance ranges are reasonably comparable show the following:

- VFM estimates for NTS explosions observed at YKA compare well to the theoretical VFM values in terms of both absolute values and the trends of the two populations.
- Gulf of California VFM observed at YKA and compared to strike-slip earthquakes did not compare well. However, theoretical dip-slip earthquake VFM values are positioned near the center of the observed data; in agreement with the observation that most of the Gulf of California earthquakes were predominantly dip-slip events.

Comparing all explosion-earthquake data (theoretical and observed) we find that the mean separation between earthquakes and explosions to be approximately 0.8 units of magnitude units normal to the population trends and for frequencies of 0.45 and 2.25 Hz.

Future work should concentrate on a systematic study of the Gulf of California earthquake parameters (i.e., depth, stress drops and fault orientations) to determine the causes of the large variance seen in the VFM estimates. Further, we have investigated only a few theoretical explosion and earthquake parameter changes and reported their effects on the VFM estimate in a qualitative way. We need to know what parameters are particularly sensitive in the estimation of VFM to determine just how much confidence can be placed on this discriminant.

VII. REFERENCES

- Alexander, Sh S. (1963), "Surface Wave Propagation in the We United States," Ph.D. Thesis, California Institf Technology, c.f., Figure 14 and parti-
cularlure 16.
- Andrews, D. J75), "From Moment to Anti-Moment: Plane-
Strainls of Earthquakes that Stop," BSSA, 65,
p. 163
- Anglin, F. M.1), "Discrimination of Earthquakes and
ExplosUsing Short Period Seismic Array Data,"
Nature, p. 51-52.
- Archambeau, C (1968), "General Theory of Elastodynamic
Sourceds," Rev. of Geophys., 6, p. 241-288.
- Archambeau, C (1972), "The Theory of Stress Wave Radia-
tion Explosions in Prestressed Media," Geophys.
J. Royr. Soc., 29, p. 329-366.
- Archambeau, C (1975), "Investigations of Tectonic Stress:
Applieaxation-Source Theory to Earthquake-Explo-
sion Dmination," The Regents of the University
of Col, Boulder, Colorado, Technical Report
AFCRL-0467.
- Archambeau, Cand C. Sammis (1970), "Seismic Radiation
from Eions in Prestressed Media and the Measure-
ment Otonic Stress in the Earth," Rev. of Geophys.,
8, p. 99.
- Archambeau, C. D. G. Harkrider and D. V. Helmberger (1974),
"Studie Multiple Seismic Events," California
Institutf Technology, Final Report U.S. ACDA (Draft).
- Bache, T. C. 0, "The Effect of Tectonic Stress Release
on Expl P Wave Signatures," BSSA (in press).
- Bache, T. C. a G. Harkrider (1976), "The Body Waves
due to veral Seismic Source in a Layered Earth
Model: Formulation of the Theory," BSSA (in
press).
- Bache, T. C., Cherry and J. M. Savino (1974), "Appli-
cation (vanced Methods for Identification and
Detectic Nuclear Explosions from the Asian
ContineSystems, Science and Software Semi-Annual
Report, R-75-2483.

- Bache, T. C., J. T. Cherry, K. G. Hamilton, J. F. Masso, and J. M. Savino (1975), "Application of Advanced Methods for Identification and Detection of Nuclear Explosions from the Asian Continent," Systems, Science and Software Semi-Annual Report, SSS-R-75-2646.
- Bache, T. C., J. T. Cherry, N. Rimer, J. M. Savino, T. R. Blake, T. G. Barker and D. G. Lambert (1975), "An Exploration of the Relative Amplitudes Generated by Explosions in Different Test Areas at NTS," Systems, Science and Software Final Report (Draft), SSS-R-76-2746, October.
- Barker, T. G., T. C. Bache, N. Rimer, J. T. Cherry and J. M. Savino (1976), "Prediction and Matching of Teleseismic Ground Motion (Body and Surface Waves) from the NTS MAST Explosion," Systems, Science and Software Technical Report, SSS-R-76-2727.
- Basham, P. W. and K. Whitham (1971), "Seismological Detection and Identification of Underground Nuclear Explosions," Publications of the Earth Physics Branch, Department of Energy, Mines and Resources, 41, p. 146-181.
- Berckhamer, H. and K. H. Jacob (1968), "Investigation of the Dynamic Process in Earthquake Foci by Analyzing the Pulse Shape of Body Waves," ARPA Project Vela Uniform Final Report AF61(052)-801.
- Blandford, R. R. (1975), "A Source Theory for Complex Earthquakes," BSSA, 65, p. 1385-1406.
- Brune, J. N. (1970), "Tectonic Stress and Spectra of Seismic Shear Waves from Earthquakes," JGR, 75, p. 4997-5009.
- Burridge, R. (1975), "The Effect of Sonic Rupture Velocity on the Ratio of S to P Corner Frequencies," BSSA, 65, p. 667-676.
- Cherry, J. T., S. Sack, G. Maenchen and V. Kransky (1970), "Two Dimensional Stress-Induced Adiabatic Flow," Lawrence Radiation Laboratory Report UCRL-50987, Livermore, California.
- Cherry, J. T., T. C. Bache, C. B. Archambeau and D. G. Harkrider (1974), "A Deterministic Approach to the Prediction of Teleseismic Ground Motion from Nuclear Explosions," Systems, Science and Software Final Report, DNA 3321F.

- Cherry, J. T., N. Rimer and W. O. Wray (1975), "Seismic Coupling from a Nuclear Explosion: The Dependence of the Reduced Displacement Potential on the Non-linear Behavior of the Near Source Rock Environment," Systems, Science and Software Topical Report, SSS-R-76-2742, September.
- Cherry, J. T., E. J. Halda and K. G. Hamilton (1976), "A Deterministic Approach to the Prediction of Free Field Ground Motion and Response Spectra from Stick-Slip Earthquakes," Eq. Engr. and Struc. Dyn., 4, p. 315-332.
- Cohen, T. J. (1968), "The Feasibility of Using Cepstrum Analysis in the Determination of Nuclear Event Depth," Internal Memorandum, Teledyne Geotech, dated 22 October.
- Cooley, J. W. and J. W. Tukey (1965), "An Algorithm for the Machine Calculation of Complex Fourier Series," Mathematics of Computation, 19, p. 297-301.
- Dahlen, F. A. (1974), "Ratio of P-Wave to S-Wave Corner Frequencies," BSSA, 64, p. 1159-1180.
- Dieterich, J. H. (1973), "A Deterministic Near-Field Source Model," Proc. World Conf. on Earthquake Eng., 5th, Rome, Italy.
- Evernden, J. F. (1967), "Magnitude Determination at Regional and Near-Regional Distances in the United States," BSSA, 57, p. 591-639.
- Evernden, J. F. (1969), "Identification of Earthquakes and Explosions by Use of Teleseismic Data," JGR, 74, p. 3828-3856.
- Fuchs, K. (1966), "The Transfer Function for P-Waves for a System Consisting of a Point Source in a Layered Medium," BSSA, 56, p. 75-108.
- Geller, R. J. and G. A. Frazier (1976), "Near Field Modeling of Dislocations in a Heterogeneous Crust: A Dynamic Finite Element Approach," submitted for publication.
- Gutenberg, B. (1944), "Travel Times of Principal P and S Waves over Small Distances in Southern California," BSSA, 34, p. 13.
- Harkrider, D. G. and C. B. Archambeau (1976), "Theoretical Rayleigh and Love Waves from and Explosion in Pre-stressed Source Regions," submitted for publication.

- Hasegawa, H. S. (1971), "Analysis of Teleseismic Signals from Underground Nuclear Explosions Originating in Four Geologic Environments," Geophys. J. Roy. Astr. Soc., 24, p. 365-381.
- Hasegawa, H. S. (1973), "Surface- and Body-Wave Spectra of CANNIKIN and Shallow Aleutian Earthquakes," BSSA, 63, p. 1201-1226.
- Haskell, N. A. (1960), "Crustal Reflection of Plane SH Waves," JGR, 65, p. 4147-4150.
- Haskell, N. A. (1962), "Crustal Reflection of Plane P and SV Waves," JGR, 72, p. 2583-2587.
- Haskell, N. A. (1964), "Total Energy and Energy Spectral Density of Elastic Wave Radiation from Propagating Faults," BSSA, 54, p. 1811-1841.
- Helmberger, D. V. and R. A. Wiggins (1971), "Upper Mantle Structure of the Midwestern United States," JGR, 76, p. 3229-3245.
- Herrin, E. (1968), "Introduction to 1968 Seismological Tables for P Phases," BSSA, 58, p. 1193-1242.
- Hill, P. and C. Pakiser (1967), "Seismic-Refraction Study of Crustal Structure Between the Nevada Test Site and Boise, Idaho," Geol. Soc. of Amer. Bull., 78, p. 685-704.
- Kanamori, H. and D. L. Anderson (1975), "Theoretical Basis of Some Empirical Relations in Seismology," BSSA, 65, p. 1073-1095.
- Kolar, O. C. and N. L. Pruvost (1975), "Earthquake Simulation by Nuclear Explosions," Nature, 253, p. 242-245.
- Lacoss, R. T. (1969), "A Large Population LASA Discrimination Experiment," Lincoln Laboratory Contract Report 1969-24.
- Madariaga, R. (1976), "Dynamics of an Expanding Circular Crack," unpublished manuscript.
- Manchee, E. B. (1972), "Short Period Seismic Discrimination," Nature, 239, p. 152-153.
- Minster, J. B. (1973), "Elastodynamics of Failure in a Continuum," Ph.D. Thesis, California Institute of Technology, Pasadena, California.

- Minster, J. B. and C. B. Archambeau (1976), "Seismic Radiation Fields from Relaxation Source Theory Models of Earthquakes," to be submitted for publication.
- Molnar, P. (1971), "P-Wave Spectra from Underground Nuclear Explosions," Geophys. J. Roy. Astro. Soc., 23, p. 273-287.
- Molnar, P., K. Jacob and K. McComy (1973), "Implications of Archambeau's Earthquake Source Theory for Slip on Faults," BSSA, 63, p. 101-104.
- Ohnaka, M. (1973), "A Physical Understanding of the Earthquake Source Mechanism," J. Phys. Earth, 21, p. 39-59.
- Peppin, W. A. and G. W. Simila (1976), "P- and SV-Wave Corner Frequencies over Low-Loss Paths: A Discriminant for Earthquake Source Theories?," submitted to J. Phys. Earth.
- Richards, P. G. (1976), "Dynamic Motions Near an Earthquake Fault," BSSA, 66, p. 1-32.
- Sato, T. and T. Hirasawa (1973), "Body Wave Spectra from Propagating Shear Cracks," J. Phys. Earth, 21, p. 415-432.
- Savage, J. C. (1966), "Radiation from a Realistic Model of Faulting," BSSA, 56, p. 577-592.
- Savage, J. C. (1972), "Relation of Corner Frequency to Fault Dimensions," JGR, 77, p. 3788-3795.
- Savino, J. M. and C. B. Archambeau (1974), "Discrimination of Earthquakes from Single and Multiple Explosions Using Spectrally Defined Event Magnitudes," Trans. Amer. Geophys. Union, EGU Abstract, 56, p. 1148.
- Savino, J. M., T. C. Bache, J. T. Cherry, K. G. Hamilton, D. G. Lambert and J. F. Masso (1975), "Application of Advanced Methods for Identification and Detection of Nuclear Explosions from the Asian Continent," Systems, Science and Software Semi-Annual Technical Report, SSS-R-76-2792.
- Springer, D. L. and R. L. Kinnaman (1971), "Seismic Source Summary for U.S. Underground Nuclear Explosions, 1961-1970," BSSA, 61, p. 1073-1098.

- Strick, E. (1970); "A Predicted Pedestal Effect for Pulse Propagation in Constant-Q Solids," Geophysics, 35, p. 387-403.
- Thatcher, W. and J. N. Brune (1971), "Seismic Study of an Oceanic Ridge Earthquake Swarm in the Gulf of California," Geophys. J. R. Astr. Soc., 22, p. 473-489.
- Wiggins, R. A. and D. V. Helmberger (1974), "Synthetic Seismogram Computation by Expansion in Generalized Rays," Geophys. J. R. Astr. Soc., 37, p. 73-90.
- Wyss, M. and J. N. Brune (1968), "Seismic Moment, Stress and Source Dimensions for Earthquakes in the California-Nevada Region," JGR, 73, p. 4681-4694.
- Wyss, M., T. C. Hanks and R. C. Liebermann (1971), "Comparison of P-Wave Spectra of Underground Explosions and Earthquakes," JGR, 76, p. 2716-2729.
- Wyss, M. and L. J. Shaney (1975), "Source Dimensions of Two Deep Earthquakes Estimated from Aftershocks and Spectra," BSSA, 65, p. 403-409.